Advanced Materials for Enhanced Condensation Heat Transfer

by

Adam T. Paxson

B.S. Mechanical Engineering
Massachusetts Institute of Technology, 2009
M.S. Mechanical Engineering
Massachusetts Institute of Technology, 2011

SUBMITTED TO THE DEPARTMENT OF MECHANICAL ENGINEERING IN
PARTIAL FULFILLMENT OF THE REQUIREMENTS FOR THE DEGREE OF

DOCTOR OF PHILOSOPHY IN MECHANICAL ENGINEERING
AT THE
MASSACHUSETTS INSTITUTE OF TECHNOLOGY

JUNE 2014

Signature redacted

Signature of Author: ______________________________
Department of Mechanical Engineering
May 20, 2014

Signature redacted

Certified by: ______________________________
Kripa K. Varanasi
Doherty Chair in Ocean Utilization Associate Professor of Mechanical Engineering

Signature redacted

Accepted by: ______________________________
David E. Hardt
Ralph E. and Eloise F. Cross Professor of Mechanical Engineering
Graduate Officer

Advanced Materials for Enhanced Condensation Heat Transfer

by

Adam T. Paxson

Submitted to the Department of Mechanical Engineering on May 20, 2014 in Partial
Fulfillment of the Requirements for the Degree of Doctor of Philosophy in Mechanical
Engineering

ABSTRACT

This thesis investigates the use of three classes advanced materials for promoting dropwise condensation:

1. robust hydrophobic functionalizations
2. superhydrophobic textures
3. lubricant-imbibed textures

We first define the functional requirements of a hydrophobic functionalization for promoting dropwise condensation and use these guidelines to investigate two subclasses of materials: rare-earth ceramics and fluoropolymer films deposited via initiated chemical vapor deposition (iCVD). We show how both materials exhibit robust dropwise behavior, and further subject an iCVD film to an accelerated endurance trial to show how it sustains dropwise condensation throughout a 3-month equivalent trial.

Next we combine hydrophobic functionalization with rough texture to obtain superhydrophobic surfaces and identify a self-similar depinning mechanism governing adhesion on surfaces with multiple roughness length scales. We introduce the metric of pinned fraction to show how these surfaces must be designed to minimize adhesion. We then show how dropwise condensation on superhydrophobic surfaces and the ensuing "jumping" behavior consists of not only binary coalescences, but multiple-drop coalescences with tangential departure that result in increased departing mass flux. However, we find that although this mode of condensation is readily achievable when condensing working fluids with high surface tension, such as water, even re-entrant structures that are known to support millimetric droplets of low-surface tension liquids in a superhydrophobic state are not sufficient to promote the dropwise mode of condensation for working fluids with low surface tension.

Finally, we extend the applicability of textured surfaces by imbibing solid textures with a lubricant stabilized by capillary wicking. We show how these surfaces, when both solid texture and lubricant are properly designed, can promote dropwise condensation and reduce departing diameter of not only steam, but also of low-surface tension working fluids.

In summary, we find that all three classes of surfaces provide significant increases in vapor-side heat transfer coefficient. However, when considering the overall heat transfer coefficient of a surface condenser, we find that most of the benefits of dropwise condensation can be realized by hydrophobic functionalization.

Thesis Supervisor: Kripa K. Varanasi
Title: Doherty Chair in Ocean Utilization Associate Professor of Mechanical Engineering

Acknowledgements

This thesis would not have been possible without the unwavering inspiration of my advisor, Prof. Kripa Varanasi, and my labmates who spent countless hours working alongside me: Dave, Chris, Brian, Karim, Seyed, Nada, Gisele, Sushant, Konrad, Jacy, Ingrid, Divya, Asli, Maher, Paris, and Arindam. Special thanks to Hyuk-Min Kwon, who has been a stalwart guide throughout my graduate studies. To the staff at Harvard CNS, notably Adam Graham, David Lange, I am grateful for time spent helping with ESEM microscopy. To the building services staff at MIT, Mike and Larry, this rig could not have taken shape without your help. This work is supported by the NSF Graduate Research Fellowship, the Bosch Energy Initiative Fellowship, the DuPont-MIT Alliance, and the Martin Family Sustainability Fellowship.

To my parents, Fred and Diane Paxson, for giving me everything I have, for unrolling giant sheets of blank newsprint to draw my first figures, for showing me how to turn ideas to tangibility in the wood shop, for refusing to believe that anything couldn't be done with enough time and patience, this is for you.

Table of Contents

List of Figures

List of Tables

1. Introduction

1.1 Motivations

1.1.1 Electricity generation

The contribution of electricity generation facilities to global greenhouse gas emissions is difficult to understate: total electrical energy production in 2013 was estimated to be more than 25,000 GWh, generated by an installed base of more than 2,800 TW of capacity that emits more than 16 Gt CO_2/yr. This accounted for more than a third of global emissions in 2013.[1] Condensation of water vapor is a crucial process in this infrastructure, as roughly 85% of the global installed base of electricity generation plants rely on steam condensers to generate a low backpressure at the outlet of a steam turbine.[2] Given the massive scale of these processes, any improvements in condenser performance would impact overall efficiencies to have a profound effect on global energy consumption.[3,4]

Dropwise condensation has been an active area of research for nearly a century, as the resulting heat transfer coefficients can be an order of magnitude higher than those seen in filmwise condensation.[5,6] However, the practical implementation of this concept in power generation, desalination, and other applications has been a significant materials challenge,[6] limited in part by durability of existing hydrophobic functionalization for metal heat transfer surfaces. While metals provide both high thermal conductivity for maximizing heat transfer and high tensile strength to minimize the need for structural supports, metals are typically wetted by water and most other thermal fluids and so exhibit filmwise condensation. Thus, metallic heat transfer surfaces must be modified with a hydrophobic coating to obtain dropwise condensation. Previous dropwise promoters have included self-assembled monolayers of oleic acids,[7,8] fatty acids, and also of thin films of polymers applied via sputtering or dip-coating.[9–13] However, most of these hydrophobic modifiers, and particularly the silane-based modifiers that are ubiquitous in recent condensation studies, are not robust in steam environments of industrial interest. More recent studies have used nanotextured surfaces to improve condensation heat transfer, however these surfaces also rely on silane or thiol modifiers to switch the wettability of a nanotextured surface from superhydrophilic to superhydrophobic.[14–20] An aim of this thesis is then to investigate materials that promote dropwise condensation of steam.

1.1.2 Low surface tension condensation

Compared to the significant body of work devoted to surface engineering for promoting dropwise condensation heat transfer of steam, much less attention has been dedicated to fluids with lower interfacial tension. A vast array of low-surface tension fluids such as fluorocarbon refrigerants, carbon dioxide, and methane are used extensively in a number of industrial applications, and the development of passive means for increasing their condensation heat transfer coefficients has potential for efficiency enhancements. Later in this thesis I investigate condensation behavior of a variety of liquids with surface tensions in the range of 12 to 28 mN/m on three types of omniphobic surfaces: smooth oleophobic, re-entrant superomniphobic, and lubricant-imbibed surfaces. We demonstrate that only smooth oleophobic and lubricant-imbibed surfaces can promote dropwise condensation of the majority of these fluids. However, we also demonstrate that on the lubricant-imbibed surfaces, the choice of lubricant and underlying surface texture play a crucial role in stabilizing the lubricant and reducing pinning of the condensate. With properly engineered surfaces to promote dropwise condensation of low-surface tension fluids, we estimate at least a two to four-fold improvement in the heat transfer coefficient.

Some strategies have been pursued for enhancement of filmwise condensation heat transfer of methane, refrigerants, and other low-surface tension fluids, including passive techniques such as fabrication of fins and channels on the condenser surface[21–25] and active methods such as vibration, electrostatic fields, and suction.[25,26] However, these techniques remain limited by the fundamental constraint of filmwise wetting behavior and could greatly benefit from promoting dropwise condensation. Previous studies of dropwise condensation are primarily devoted to steam, with a few studies of fluids with high or moderate surface tension[27–31] or Marangoni dropwise condensation of binary mixtures.[32–38] To our knowledge, dropwise condensation of fluids with a surface energy, $\gamma_{lv,}$ less than 20 mN/m has not yet been demonstrated, since many of the materials commonly used as non-wetting modifiers do not have a critical solid surface energy low enough to prevent filmwise wetting. For example, methane (γ_{lv} = 9mN/m at 293K) and the refrigerant R-134a (γ_{lv}= 18 mN/m at 90K) will both spread on a poly-tetrafluoroethylene surface (PTFE, γ_c = 18 mN/m) and would exhibit filmwise condensation.[39,40] Accordingly, promotion of dropwise condensation necessitates the use of highly-fluorinated low-surface energy materials such as trichloro (1H,1H,2H,2H-perfluorooctyl) silane (fluorosilane, γ_c = 10.1 mN/m). However, even on these surfaces, the contact angle will be significantly below 90°.

Since increases in drop contact angle above 90° have been shown to significantly affect the heat transfer coefficient, h,[41–43] a decrease of contact angle is also likely to impact h. To quantify this effect, we used a model developed by Kim and Kim[44] to explore heat transfer during condensation of drops with contact angles less than 90°. We estimated the variation of the heat transfer coefficient with contact angle for an illustrative low-surface tension fluid, octane, at a saturation temperature of 293K condensing on a subcooled vertical surface with contact angle varying between 30° and 150°.

The expected increase in heat transfer coefficient of DWC vs. FWC of low-surface tension fluids can be estimated using Kim and Kim's[1] and classical Nusselt models,[2] respectively. Kim and Kim's model extends classical DWC models[3] for hemispherical drops to predict heat transfer through a drop with radius r and arbitrary contact angle θ:

$$q_d = \frac{\Delta T \pi r^2 \left(1 - r_c / r\right)}{\left(\frac{\delta}{\sin^2 \theta k_{film}} + \frac{r\theta}{4k_w \sin\theta} + \frac{1}{2h_i\left(1-\cos\theta\right)}\right)} \qquad \text{Equation 1-1}$$

where ΔT, r_c, h_i, δ, k_{coat}, and k_w are the surface subcooling, critical nucleation radius, interfacial liquid-vapor heat transfer coefficient, thickness of the coating, and thermal conductivities of the coating and liquid, respectively. The overall heat transfer rate per unit area for different degree of surface subcooling is obtained by integrating the product of q_d and drop size distribution, $n(r)$, from r_c to the departure radius $0.4\mathrm{l}_c$ defined as a constant multiplied by the capillary length l_c

$$q'' = \int_{r_c}^{\hat{r}} q_d n(r) dr \qquad \text{Equation 1-2}$$

Variations of this equation have been used by several groups to estimate heat transfer rate on surfaces with $\theta > 90°$.[4-5] Here, we used Equation 1-2 with $n(r)$ developed by Kim and Kim to explore heat transfer during DWC of drops with $\theta < 90°$. For "large" drops this distribution is identical to the classical Rose's DWC distribution.[3] Kim and Kim used population balance to derive size distribution of drops with radius smaller than $r_e = (4N_s)^{-0.5}$. The value of nucleus density, N_s, is difficult to measure and is typically in the range of 10^8 to 10^{12} m^{-2}. Although the model is largely insensitive even to large changes in magnitude of the nucleation density. For the following calculations, the value of nucleation density was derived from the DWC heat transfer measurements of condensing pentane droplets and set to $4\text{x}10^{10}$ m^{-2}.

The plot in Figure 1-1a shows that the heat transfer coefficient decreases as the contact angle decreases below about 90° for water, and below about 60° for octane. Despite this effect, a comparison of *h* during filmwise and dropwise condensation of water and octane, shown in Figure 1-1b as the slope of *q"* vs. ΔT, reveals a more than ten-fold increase in heat transfer coefficients from about 3 kW/m^{2}K to about 40 kW/m^{2}K in the case of octane.

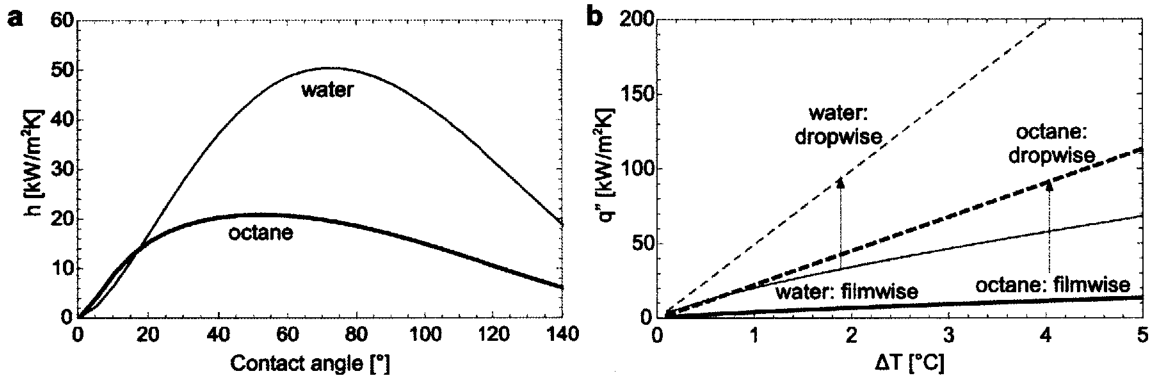

Figure 1-1. **Estimated heat transfer coefficient for low-surface tension fluids.** (a) Heat transfer coefficient estimated by Kim and Kim model for water and octane. (b) Estimated increase in heat flux (*q"*) vs. subcooling (ΔT) for filmwise and dropwise condensation of octane and water.

Motivated by the above results, we examine the fundamental design criteria of a surface for promoting dropwise condensation of low-surface tension fluids. The most basic condenser surface must have a critical surface energy appreciably lower than that of the condensate to result in a finite wetting angle, and a contact angle hysteresis low enough to allow condensate drops to shed before they coalesce to form a continuous film.[29,45] Beyond a simple smooth non-wetting surface, textured superhydrophobic surfaces have been employed to further enhance the dropwise condensation heat transfer coefficient. If the surface is sufficiently rough, it will promote a mode of water condensation commonly referred to as "jumping condensation."[18-20,46,47] However, this phenomenon relies on a large difference in surface energy between the condensate and solid surface in order to promote a robust Cassie-Baxter state.[48-50] In the case of low-surface tension liquids, a Cassie-Baxter state is significantly more challenging to maintain. Superomniphobic surfaces have been demonstrated to overcome this challenge by employing re-entrant textures to promote a Cassie-Baxter state even with low-surface tension liquids such as ethanol ($\gamma_{lv} = 24.8$ mN/m).[51-53] However, as with water condensate flooding of superhydrophobic surfaces, it is possible that re-entrant surfaces might lose their superomniphobic characteristics during condensation of low-surface tension fluids due to nucleation and growth of condensate drops within the texture.[54,55,14,56,15,57] To overcome the challenge of condensate impalement, Anand et al.[58] recently demonstrated that the departure diameter of condensing water drops can also be significantly decreased by impregnating a micro/nano-textured surface with a thin film of a lubricant that is immiscible with water. Such lubricant-imbibed surfaces have been shown to possess omniphobic, low hysteresis, self-cleaning, self-healing properties and will be described in 1 of this thesis.[59-63]

1.2 Thesis scope and content

This thesis is organized around three classes of surfaces for promoting dropwise condensation roughly in order of increasing conceptual complexity:

4. robust hydrophobic functionalizations
5. superhydrophobic textures
6. lubricant-imbibed textures

Chapter 2 details the experimental methods used to measure condensation heat transfer coefficients. The first subsection explains changes in the experimental apparatus since the first iteration of the setup.[64] Specifically, the instrumentation and calibration methods are substantially improved, and a novel method for sample attachment is developed to allow precise, high-flux measurements while maintaining flexibility in rapidly swapping sample surfaces. The second subsection details the methods used to create the textured surfaces used later in Chapter 3, including mask-free dry etching of silicon and metal oxidation.

Chapter 3 outlines the requirements of a seemingly “simple” hydrophobic functionalization, and quickly elucidates the complexities of developing such a material for industrial use. We investigate two candidate materials for meeting these requirements: the first subsection describes a family of rare-earth oxide ceramics with intrinsic hydrophobicity,[65] wherein the wetting theory behind hydrophobicity and measurements of condensation heat transfer coefficient on these surfaces are explained. The second subsection details the chemical and wetting properties of an ultra-thin grafted fluoropolymer films deposited via initiated chemical vapor deposition (iCVD) along with promising results from an accelerated endurance trial.[66]

Chapter 4 builds on the basic concept of intrinsic hydrophobicity by adding rough texture to obtain a superhydrophobic surface. Before discussion of condensation results, the first subsection, Section 3-2, presents the results of a study of the microscopic origins of contact angle adhesion and hysteresis on superhydrophobic surfaces. We describe a technique for measuring the dynamic behavior of the three-phase contact line at micron length scales using environmental scanning electron microscopy.[67] We examine a superhydrophobic surface on which a drop's adhesion is governed by capillary bridges at the receding contact line. We measure the microscale receding contact angle of each bridge and show that the Gibbs criterion is satisfied at the microscale, revealing a hitherto unknown self-similar depinning mechanism that shows how some hierarchical texture such as lotus leaves lead to reduced pinning, and counter-intuitively how some lead to increased pinning. We develop a model to predict adhesion force and experimentally verify the model's broad applicability both on synthetic and natural textured surfaces. The next subsection examines the behavior of a surface that maintains a superhydrophobic wetting state under condensation at high subcooling and heat flux. We show that the ensuing "jumping" behavior consists predominately of multi-drop coalescence events, in contrast with the two-drop coalescences that have been previously observed at lower heat fluxes. This tangential component of droplet departure leads to increased droplet departure mass flux and therefore increased heat transfer coefficients.

Chapter 5 adds yet another aspect to textured hydrophobic surfaces by imbibing the solid texture with a liquid lubricant. The thermodynamic wetting states of these surfaces is explained with emphasis on those states which are advantageous during condensation, and we show how proper selection of the lubricant is crucial for obtaining optimal condensing performance. After detailing the behavior of condensation of steam on these surfaces, we further compare their performance under condensation of low-surface tension working fluids to that of smoother hydrophobic functionalizations and “dry” superhydrophobic textures in the next subsection. We show that the maintenance of a superhydrophobic “jumping” state is made substantially more difficult with working fluids of low surface tension, but that proper selection of lubricant and surface texture parameters leads to dropwise condensation even of pentane, with a surface tension of 15 mN/m.

Chapter 6 concludes by comparing the condensation heat transfer coefficients of the three classes of surfaces in the context of a surface condenser in a power plant. Crucially, we find that owing to the other thermal resistances present in the system, namely the convection inside the condenser tubes and the conduction through the tube wall, there exist rapidly diminishing returns when pursuing ever-higher condensation heat transfer coefficients. Even modest increases in heat transfer coefficient have a profound effect on the overall thermal efficiency of the steam cycle, and most of the benefits of dropwise condensation are captured by even a modestly-performing hydrophobic functionalization.

2 Experimental section

2.1 Condensation rig

2.1.1 Functional requirements

The aim of the current apparatus is to evaluate the thermal performance of condensing surfaces at conditions equivalent to those seen in industrial power plants.[68] The operating conditions of an exemplary power condenser from the Heat Exchange Institute Surface Condenser Standards are listed below in Table 2-1:

Table 2-1. Operating pressure, flux and tempertaure of a typical power condenser.[68]

Parameter	Value	Units
P	3.98 kPa	condenser pressure
q''	30.68 kW/m^2	heat flux
T_s	28.89 °C	steam temperature
$T_{c,in}$	15.5°C	coolant inlet temperature

One of the functional requirements immediately becomes the maintenance of a sub-atmospheric pressure vacuum, since a typical condenser operates at pressures between 3 and 5 kPa. The effects of non-condensable gases in the measurements must be given special consideration, and have been shown to lead to inaccurate results in previous experiments.[6] Any vapor other than steam will be carried by the steam flow towards the condensing surface and accumulate in a vapor blanket, thus imposing a thermal resistance in the form of a diffusion barrier.[69–72]

2.1.2 Literature review

There are number of strategies for obtaining the heat flux and surface temperature. The most common approach involves the use of a condensing disc or plate with temperature probes embedded at precisely known locations in an attempt to extrapolate the temperature gradient within the block, and thus the heat flux with the knowledge of the thermal conductivity of the block. A number of others use a configuration more reminiscent of an industrial condenser, measuring the heat flux via the log-mean temperature difference across the condensing section of a condenser tube and extrapolating the surface temperature from knowledge of the coolant flow and thermal properties of the tube.[69,73–77]

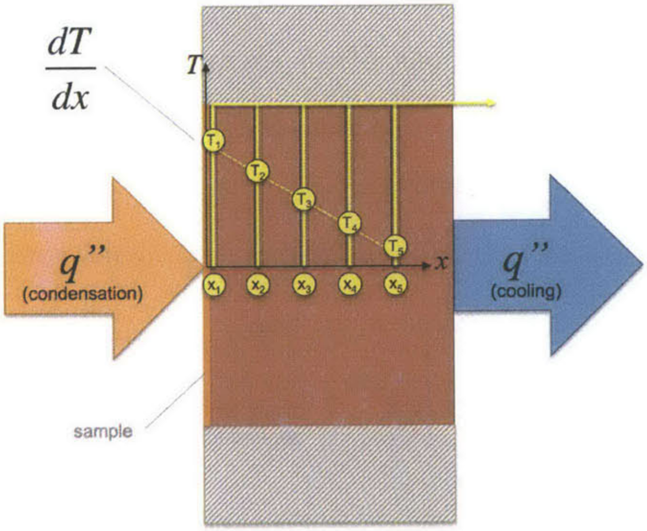

Figure 2-1. **Heat transfer coefficient measurement principle**. The sample side of a measurement block is exposed to saturated steam while the back side of the block is cooled. Thermal insulation around the periphery of the block ensures one-dimensional heat transfer, so that all heat fluxes occur in parallel. Temperature probes embedded at precisely known locations within the block are used to extrapolate the temperature gradient, and then with knowledge as to the thermal properties of the block, the heat flux may be calculated.

2.1.3 Rig design

The design of the current rig is inspired by the work of Koch and Leipertz.[78,79] By measuring the temperature at precise locations within the apparatus, we can calculate h_c, the condensation heat transfer coefficient

$$h_{dc} = \frac{q_{block}}{\Delta T_s} \qquad \text{Eqn. 2-1}$$

where q_{block} is the heat flux through the chiller block, obtained by measuring the temperature within the chiller block at incremental axial locations, and ΔT_s is the difference between the temperature of the condensing surface and the saturation temperature of water at the chamber pressure. The heat flux through the cooling block can be calculated as

$$q = -k\frac{dT}{dx} \qquad \text{Eqn. 2-2}$$

where x is the axial position as measured from the front surface of the block, k is the thermal conductivity of the block, and q is the heat flux through the block in W/m^2.

2.1.3.1 Flow loop

The steam flow loop is shown below in Figure 5-2. All steam lines are constructed from stainless steel with vacuum-compatible fittings.

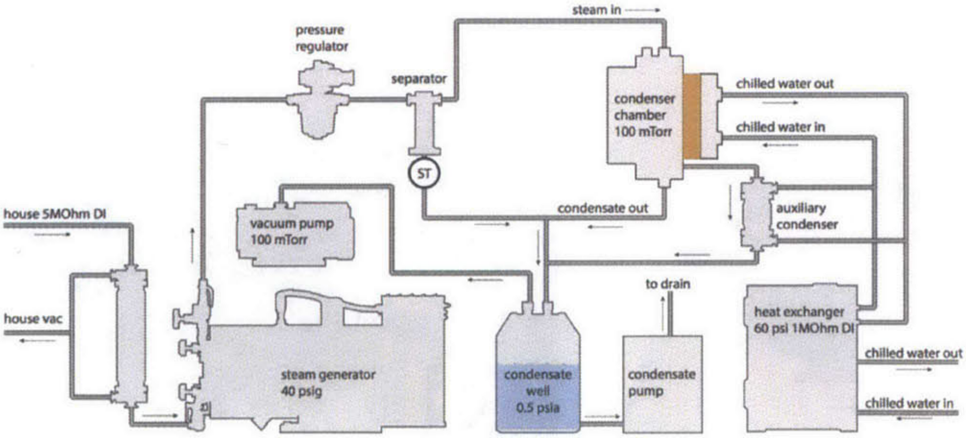

Figure 2-2. **Condensation rig flow loop.** The apparatus is build around a condensing chamber capable of vacuum levels down to 100 mTorr to evacuate non-condensables to a level less than 1ppm. Steam is supplied by an electric boiler fed by deaerated, deionized feedwater. The condensing sample is cooled by a chilled water loop.

2.1.3.2 Steam and coolant chambers

The chamber design incorporated as many stock parts as possible. The steam portion of the chamber, colored gray in Figure 2-3, was based around a 4" Pyrex viewport (Part #945001, MDC Vacuum) and a number of Quik-Flange fittings for fluid and instrumentation inlet and outlets. The rear portion of the steam condensing chamber consisted of a custom-machine receptor plate to receive the sample and insulation subassembly along with an access port for inserting thermistors into the sample puck. Construction was all 316 stainless steel with internal welds facilitated by weld tabs designed onto the receptor plate.

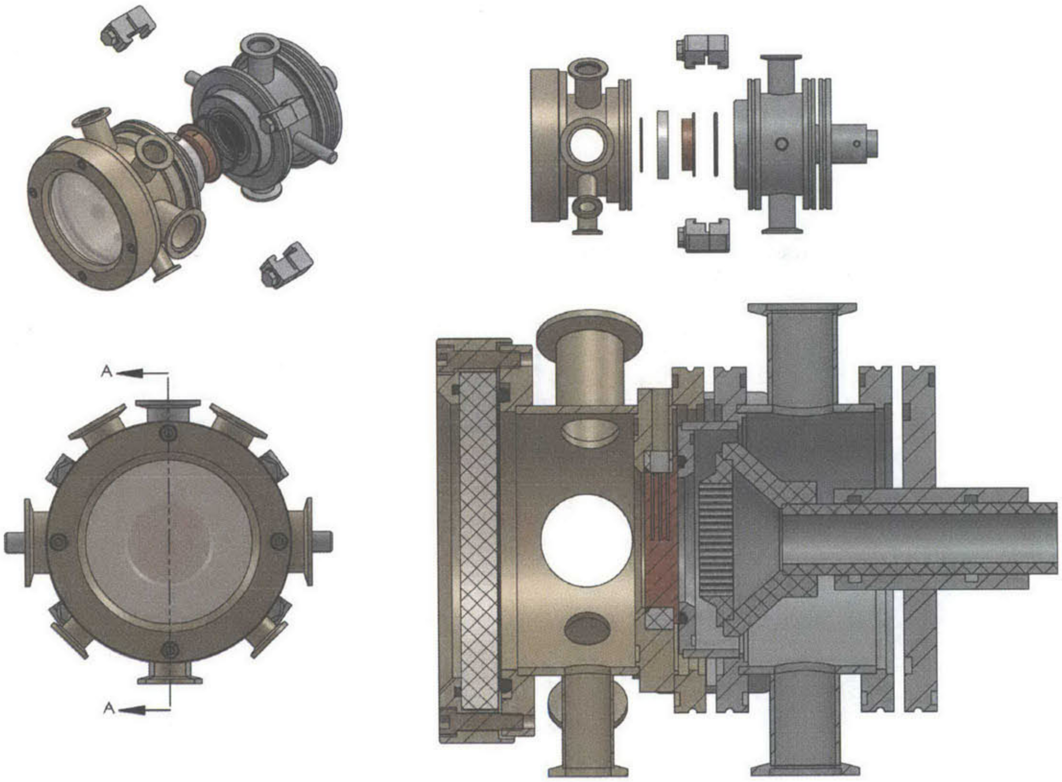

Figure 2-3. **Steam and coolant chambers**. Steam and condensing portion shaded in gray, coolant portion shaded in blue. (a) Isometric exploded view of chamber with sample subassembly and four claw clamps. (b) Side exploded view of chamber showing assembly sequence of sample puck and insulation with o-ring seals. (c) Front view of chamber showing port configuration. (d) Section view A-A showing seal detail and design of coolant and sample inspired by Koch and Leipertz.

2.1.3.3 Steam source

Deionized water (5 MΩ/cm) is first deaerated by passing through a membrane degassifier (LiquiCel, MarCor) to less than 4ppm dissolved O_2. The feedwater is pumped to a pressurized stainless steel boiler chamber (SR-20, Reimers), where a set of 440V heating elements boils the water to generate steam. A steam separator and steam trap are installed immediately upstream of the condensation chamber to ensure that only saturated steam reaches the chamber. Since the steam is generated at 40psi, it undergoes considerable flashing once it passes through the pressure regulator. A needle valve is provided as a bypass measure should the actuator fail. The quality of the steam is reduced significantly, and the separator removes the entrained water vapor. The steam trap at the bottom end of the separator ejects condensate into a condensate collection chamber. Due to contamination concerns, the system is not a cyclic loop. Condensate from the separator, the chamber, and the auxiliary condenser is collected in a reservoir that is drained after filling.

A 10L stainless chamber was drained and evacuated before each condensation run with a rotary vane vacuum pump (RV3F, Edwards). It is equipped with two float switches controlling a condensate pump (Model # 8000-033-236, ShurFlo) that is able to self-prime at sub-atmospheric pressure. The condensate reservoir is preceded by a secondary condenser for drawing steam through the main condenser chamber and further cooling condensate collected from the steam trap.

2.1.4 Sample puck design

The design of the sample puck built upon lessons learned from the first iteration of the condensation rig.[64] There are four principal functional requirements for this assembly: it must provide the steam-side test surface, the cooling surface, thermowells, and sealing surfaces. These functions were previously accomplished by four separate parts: a sample puck, a measurement block, a cooling block, and a Teflon piece for both sealing and thermal insulation. Figure 2-4 shows how these functions were combined into a single part, again inspired by the designs of Koch and Liepertz.[79] The sample puck consisted of an active section with a 2.000" diameter and a flange for providing a sealing surface for coolant at the rear side.

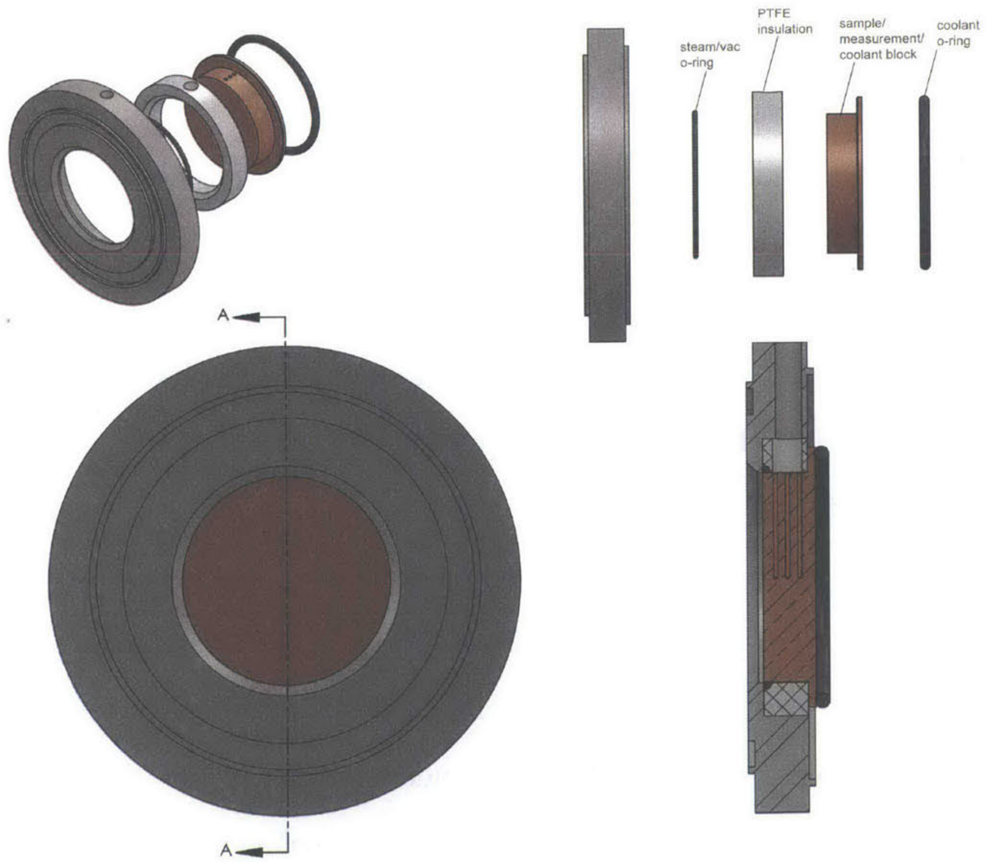

Figure 2-4. **Sample puck subassembly**. (a) Isometric exploded view of sample puck along with stainless steel sample plate from condenser chamber subassembly. (b) Exploded view of subassembly showing sequence of insulation ring and o-ring seals. (c) front view of sample puck. (d) Section view A-A of sample puck subassembly showing detail of o-ring seals and thermowells.

Figure 2-5 shows a detail view of the sealing surfaces. The Teflon insulation piece is designed with a bevel seal that presses an o-ring against the outer surface of the metal sample puck. In this manner, the entire 2" surface can be utilized without need for bolting a restraining structure to the front face, as in the previous rig design. The middle portion of the sample block is exposed to atmosphere, since it is through this area that the thermowells are accessed from the top of the rig. An access hole runs through the sample retainer plate, through the Teflon insulation, and meets the three thermowells. The rear of the measurement puck is a simple face seal against an o-ring that is retained in a gland machined into the coolant chamber.

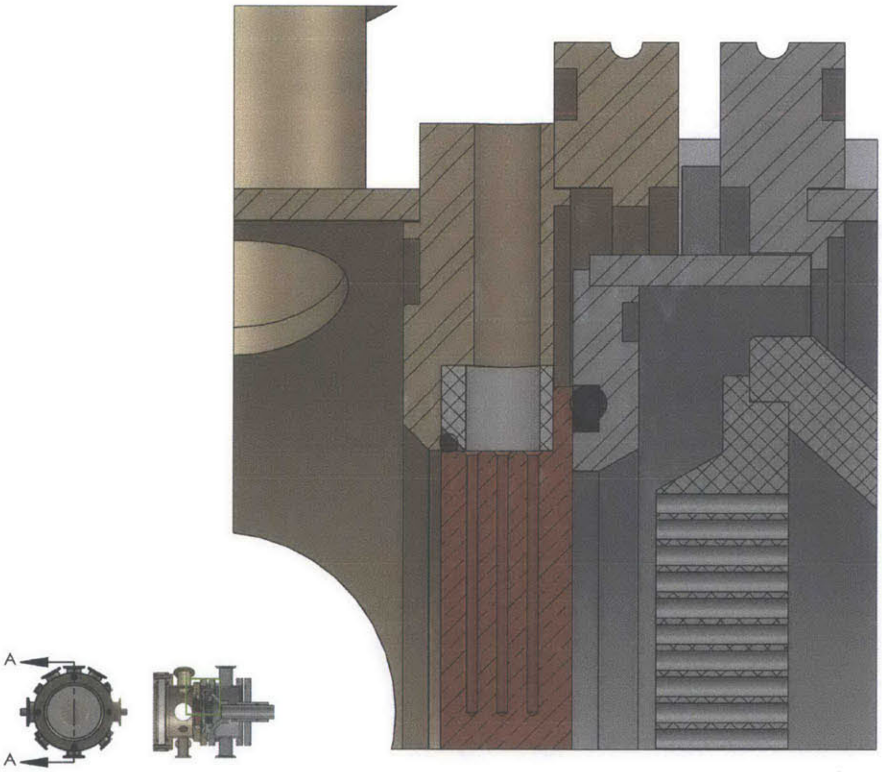

Figure 2-5. **Seal detail**. Steam-side is isolated by a bevel seal o-ring, while coolant-side surface is isolated with a face seal. Middle portion of block is accessible through thermowell port.

2.1.5 Instrumentation

Three thermistors were used to determine temperatures to better than 0.01°C accuracy. Temperature probes were assembled by inserting a 2.252 kΩ thermistor (T337, Redfish Sensors) into a precision stainless steel tube (19TW, VitaNeedle). Probes were hermetically sealed with adhesive and connected to a high-precision voltage measurement data acquisition block (9219, National Instruments). Cable shielding was crucial for obtaining low noise floors for thermal measurements.

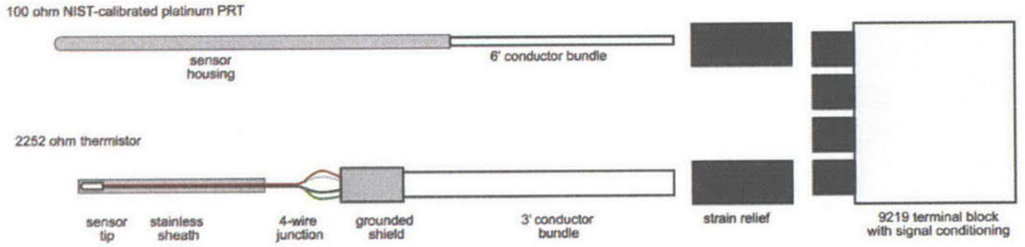

Figure 2-6. **Temperature probes and DAQ interface.** Top: high-precision NIST-calibrated platinum resistance thermometer. Bottom: thermistor with shielded 4-wire connection.

3 Hydrophobic functionalization

3.1 iCVD films

3.1.1 Introduction

Polymeric materials, including the coatings tested by Marto et al.,[12] are most commonly processed using solvent-based methods that require all precursor constituents to have a common solvent. This imposes a constraint on the design of tailored surfaces for wetting, since a common solvent may not be available for a significant number of material combinations. For example, many hydrocarbon and fluorocarbon precursors lack a common solvent, making the wet processing of these materials extremely difficult. In chemical vapor deposition (CVD), since all material precursors are transported in their vapor phase instead of in a liquid solvent, the constraint of a common solvent is eliminated. Furthermore, the precursor consumption, not to mention the elimination of a need for large quantities of solvent, have led to the adoption of lower-cost CVD techniques, which are further augmented by their lack of deleterious surface tension effects and their precise control of coating thickness.[80] Initiated chemical vapor deposition (iCVD) is a variant of hot-wire chemical vapor deposition in which an initiator species, typically a peroxide, is thermally cleaved to produce a free radical which is then adsorbed on the substrate to initiate polymerization of a second monomer species. iCVD differs from conventional HWCVD in that it is performed at low temperatures (substrate temperature $< 40°C$) and low energy inputs.

Now presented with a largely unrestricted choice of monomer precursor, we are faced with the selection of an appropriate monomer for hydrophobic functionalization. Zisman and coworkers have shown that the lowest surface free energies are attained by constructing close-packed monolayers of $-CF_3$ end groups, resulting in a critical surface energy of approximately 6 mN/m.[81,82] Increasing the length of the perfluorinated chain will tend to decrease the critical surface energy, but will also result in a lower vapor pressure and thus a less facile application to the iCVD process. Accordingly, the selection of an optimally low-surface energy monomer is constrained to the selection of an appropriate chain length terminated at one end by a $-CF_3$ group and at the distal end by a vinyl group for the purposes of radical polymerization, wherein the chain length is as long as possible while still amenable to vaporization at near-room temperatures.

Perfluorodecyl acrylate (PFDA) was used as the monomer precursor for obtaining hydrophobic functionalization on the following condensation studies. Depicted below in Figure 3-1, PFDA consists of a perfluorinated C_8 functional group with a vinyl anchor group.

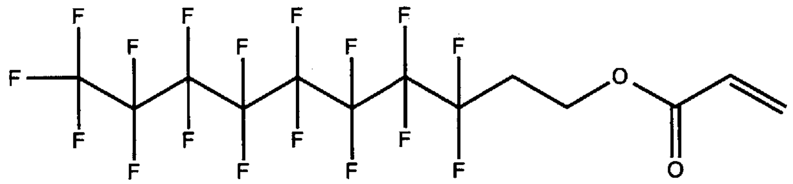

Figure 3-1. **Schematic of perfluorodecyl acrylate.** Perfluorinated C_8 functional group with vinyl pendant group.

Thin films of poly(perfluorodecyl acrylate) p(PFDA) deposited via iCVD have been shown to exhibit a high degree of hydrophobicity, with a advancing contact angles larger than 130° and contact angle hysteresis less than 15°.[83] Using tert-butyl peroxide (TBPO) as a radical initiator, and by controlling the ratio of initiator to monomer, films of varying degrees of crystallinity have been obtained, with lowest hysteresis exhibited on films of higher crystallinity index. Crystallinity leads to formation of microstructures, which increase both the surface roughness and contact angle hysteresis. PFDA tends to crystallize in a smectic B phase, with pendant perfluorinated chains arranged parallel to the substrate normal such that successive bilayers of alternating base- and end-groups are arranged parallel to the surface. Although these crystalline domains help prevent rearrangement of the perfluorinated chains into the bulk of the film, which would otherwise increase the contact angle hysteresis, it has the additional undesirable effect of increasing surface roughness. Increasing filament temperature during deposition causes the initiator to switch from a regime dominated by tert-butoxy radicals and parallel crystallographic orientation of perfluorinated side chains to a deposition regime dominated by methyl radicals, and perpendicularly-oriented perfluorinated side chains. There is a corresponding increase in roughness from 22 nm RMS at 240°C to nearly 60 nm at a filament temperature of 300°C, with a corresponding increase in water contact angle hysteresis from 7° to 40°. This drastic change in hysteresis highlights the importance of roughness in determining wettability, and that maintaining a substantially smooth surface is important in obtaining reasonable dropwise condensation performance.

By introducing vinyl groups onto the substrate surface, covalent bonds are formed between the radical initiator and adsorbed monomers during deposition.[84] As evidenced by XRD spectroscopy, the presence of a vinyl grafting layer substantially increases the degree of crystallinity, along with the surface fluorine/carbon ratio. These two effects lead to a drastic reduction of surface energy, as a higher degree of $-CF_3$ end groups are incorporated at the surface. The increase in roughness is sufficient to promote a superhydrophobic wetting state, which manifests as an advancing contact angle of 160° and a contact angle hysteresis of 5°.

Although crystallization and roughness have been shown to exhibit a desirable combination of high contact angle and low hysteresis, many applications require temperatures above the glass transition temperature of many organic crystalline materials. Furthermore, not all monomer species are capable of reliable crystallization. For these reasons, it is imperative to pursue other means of minimizing intrinsic contact angle hysteresis stemming from steric mobility. Crosslinking provides an alternative to crystallization as a means for providing steric hindrance, and further disrupts crystallization, leading to smoother films. Copolymers of PFDA and DVB have recently been incorporated into photonic circuits for use as an athermal cladding.[85] Yagüe and Gleason demonstrated that by optimizing the ratio of PFDA to divnylbenzene (DVB) crosslinker, relatively smooth films with RMS roughness less than 50nm and water contact angle hysteresis less than 10°.

In the remainder of this section, copolymer films of p(PFDA-*co*-DVB) are compared to coatings of trichloro(1H,1H,2H,2H-perfluorooctyl)silane, a hydrophobic modifier that used in a number of condensation studies, across a number of performance metrics including nucleation density, contact angle hysteresis, and durability in high-temperature steam condensation.

3.1.2 Experimental methods

3.1.2.1 Silanization

Polished silicon substrates were prepared for silanization by first cleaning by sonication in acetone for 5 minutes, followed by rinsing in DI water (18 MΩ/cm), followed by sonication in isopropanol for 5 minutes, and a second rinse with DI water. The surfaces were treated with oxygen plasma for 10 minutes (Harrick Plasma) for further cleaning and for increasing the surface density of hydroxyl groups. Immediately following plasma treatment, the substrates were transferred to a vacuum desiccator that also held a small amount (approx. 50 µL) of either trichlorovinylsilane (97%, Sigma Aldrich) for obtaining a vinyl-covered iCVD precursor substrate, or trichloro(1H,1H,2H,2H-perfluorooctyl)silane (97%, Sigma Aldrich) for obtaining a fluorosilanized benchmark surface. The vacuum desiccator was evacuated to 200 mTorr and the chamber was isolated to allow the silane to begin to vaporize. The chamber was purged twice more to increase silane concentration, then finally isolated and allowed to react with the substrate for 15 minutes in the case of vinylsilane and for 2 hours in the case of fluorosilane. After silane deposition, the substrates were sonicated in toluene for 5 minutes to remove excess unreacted silane and rinsed with DI water.

3.1.2.2 iCVD procedure

iCVD polymerizations were conducted in a custom-designed cylindrical reactor (diameter 24.6 cm, height 3.8 cm), with an array of 14 parallel Chromalloy heating filaments (Goodfellow) suspended 2 cm above the sample stage Figure 3-2. Tert-butyl peroxide (TBPO, 98%, Aldrich), perfluorodecyl acrylate (PFDA, 97%, Aldrich), and divinylbenzene (DVB, 80%, Aldrich) were used as-received. TBPO was delivered to the reactor through a mass flow controller (MKS Instruments) through heated lines at a constant flow rate of 3.2 sccm. PFDA and DVB were vaporized in glass jars that were heated to 80°C and 60°C, respectively. Their flow rates were controlled by manually adjusting precision needle valves to achieve rates of 0.2 and 0.6 sccm, respectively. The resistive filaments were heated to 230°C by controlling current using a DC power supply (Sorensen), and filament temperature was measured by a K-type thermocouple (Omega). The sample stage was maintained at 30°C with a recirculating temperature bath (Neslab RTE-7). The chamber pressure was maintained at 200 mTorr using a throttle valve at the vacuum outlet (MKS Instruments). The reactor was covered with a quartz top (2.5 cm) that allowed in-situ thickness monitoring by interferometry with a 633 nm HeNe laser source (JDS Uniphase). Following deposition, the samples were transferred to an oven (VWR) to be annealed at 80°C for 30 min to increase crosslinking density.

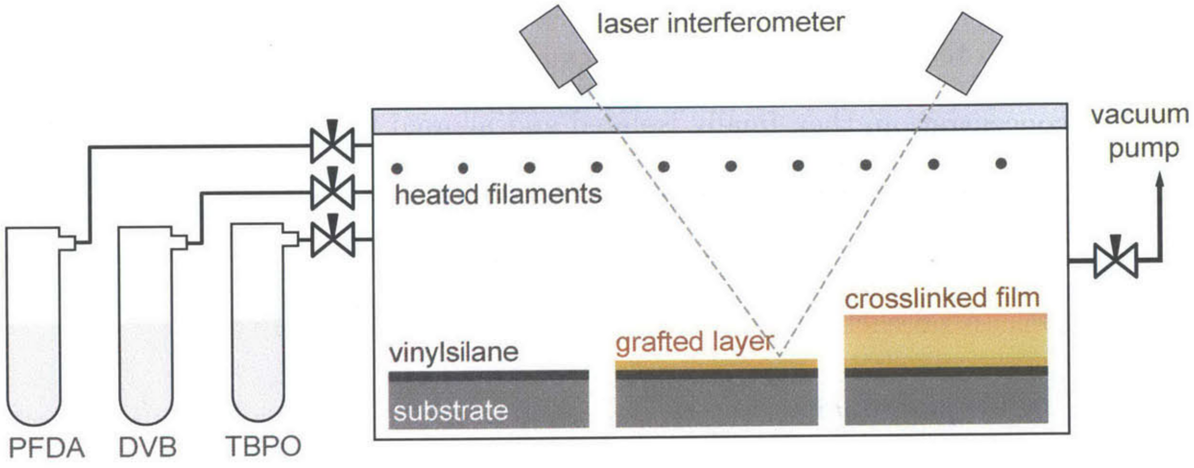

Figure 3-2. **Schematic of iCVD reactor.** Initiator (TBPO) and monomer (DVB, PFDA) species are flowed into a chamber maintained at 200 mTorr by exhaust valve. TBPO is thermally cleaved by heated filaments and covalently bonds to vinyl groups of vinylsilanized substrate, initiating polymerizations. Successive layers of PFDA are grafted to substrate and crosslinked by DVB. Thickness is monitored *in situ* by laser interferometer to determine end of deposition.

3.1.3 Surface characterization

Film thicknesses were measured *in situ* by laser interferometry and verified by variable-angle ellipsometric spectroscopy, (VASE, M-2000, J. A Woollam), atomic force microscopy (AFM, MP3D-SA, Asylum) and contact profilometry (Model 150, Dektak). All VASE thickness measurements were performed at a 70° angle of incidence using 190 wavelengths from 315 to 718 nm. A nonlinear least-squares minimization was used to fit ellipsometric data of dry films to the

Cauchy-Urbach model. The thickness was obtained upon convergence of the algorithm. All AFM thickness measurements were preformed in tapping mode over an area of 20 µm x 20 µm using a cantilever with a tip radius of 9 ± 2 nm (AC200Ts, Asylum). The film thickness was calculated as the difference between the average heights of the rough film surface and the trough of a nearby scratch; the rough built-up edge of the scratch was masked from analysis. The profilometry measurements were performed with a stylus having a radius of 12.5 µm. The film thickness was similarly calculated as the difference in the average height of the rough film and the smooth scratch trough. AFM and profilometry measurements were repeated on at least four locations. Film thickness was determined as the average of all measurement methods to be 41.5 ± 2.4 nm, summarized below in Table 3-1.

Table 3-1. Film thickness measurements

method	**Thickness**
ellipsometry	40 ± 2 nm
profilometry	41.5 ± 2.3 nm
AFM	43.0 ± 1.8 nm
mean	**41.5 ± 2.1 nm**

At this thickness, the resistance of the film assuming a thermal conductivity of 0.2 W/mK typical for bulk fluoropolymers represents 0.001% of the overall thermal resistance of a typical condenser tube. It can thus be assumed that the thermal resistance of such an ultra-thin film contributes negligibly to the overall heat transfer coefficient of the heat exchanger.

AFM scans shown in Figure 3-3 indicate that the surface topology consists of isolated microstructures similar to those seen in previous studies[83,84,86] with hemispherical agglomerates with a characteristic height of 100 nm and an average spacing of 1.3 ± 0.7 µm, resulting in an RMS roughness of 75 nm. These structures are the result of crystalline domains nucleating on the substrate during condensation polymerization of the monomers into a smectic B structure that arrange into a rotationally symmetric fiber texture.

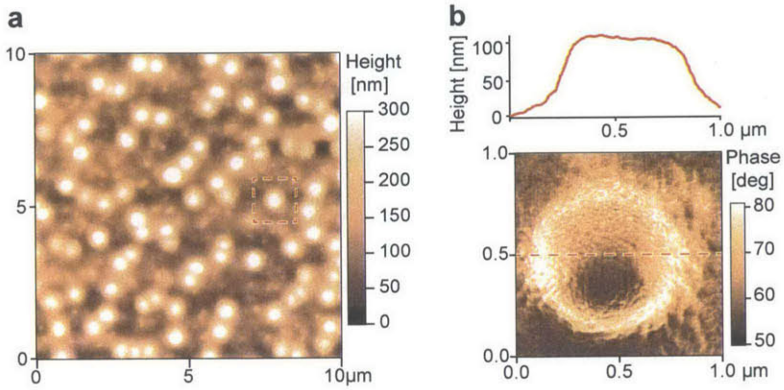

Figure 3-3. **iCVD copolymer film morphology.** AFM scans of p(PFDA-*co*-DVB) deposited on a polished silicon substrate. (a) 10 μm x 10 μm height scan. (b) Phase scan of single nodule indicated by dotted box in (a) and corresponding height profile (top inset).

The composition at the near-surface region is important in determining the wettability and hysteresis of the copolymer film. High-resolution angle-resolved X-ray photoelectron spectroscopy (AR-XPS) was used to probe the topmost region of the film. The XPS spectra were collected by a SSX-100 X-probe (Surface Science Instruments) equipped with a monochromatized Al K_α source operated at 1486.8 eV. Survey scans were conducted at a 0° take-off angle. The two important bonding environments of the $-CF_2$ and $-CF_3$ constituents of the pendant group can be resolved from the XPS spectra at 290.8 and 293.1 eV, respectively. The combined area of the spectrum under these peaks is 61.8 ± 0.4%, with the peaks at the lower binding energies representing other bonding environments not of interest: carbons directly bonded with oxygen, hydrogen, or other carbon atoms. These same $-CF_2$ and $-CF_3$ bonding environments were observed previously in the C1s XPS spectrum of a PFDA homopolymer deposited via iCVD and represented a combined spectrum area of 61.4 ± 0.3%.[87] This is in good agreement with the structural formula for PFDA, which would give a theoretical value of 61.5% for the combined peak area of the $-CF_2-$ and $-CF_3$ regions. This indicates that the present film has a low degree of DVB incorporation in the near-surface region. However, we confirm the incorporation of DVB in the bulk by use of Fourier transform infrared spectroscopy (FTIR, Nicolet Nexus 870 ESP). Measurements were taken in normal transmission mode equipped with a mercury cadmium tellurium detector and KBr beamsplitter. Spectra were acquired over the range of 400 to 4000 cm^{-1} with a 4 cm^{-1} resolution for 256 scans. FTIR measurements confirmed peaks at 2810 and 2980 cm^{-1} corresponding to sp^2 C-H stretching modes that indicate incorporation of DVB in the bulk film. These results lead us to expect the underlying crosslinking DVB units to reduce the ability of the surface to reconstruct between the dry and wet states, potentially reducing this intrinsic steric contribution to contact angle hysteresis.

Wettability was measured using the volume addition and subtraction method: a 32g stainless steel dispensing needle was used to deposit a 1μL droplet of deionized water (18MΩ/cm) on the surface using a motorized syringe pump (ramé-hart), and the volume was increased at the rate of 0.1μL/sec up to a volume of 5μL while measuring the advancing receding angle with a goniometer and profile-fitting contact angle software (Model 590 Advanced, DropImage, ramé-hart). Water was then withdrawn at a rate of 0.1μL/sec while measuring the receding contact angle. Wetting properties of the resulting surface are reported below in Table 3-2. Water contact angles on iCVD copolymer thin film deposited onto polished silicon wafer as the mean and standard deviation of the mean measured at four locations:

Table 3-2. Water contact angles on iCVD copolymer thin film deposited onto polished silicon wafer

θ_a	θ_r	$\Delta\theta$
132° ± 1°	127° ± 1°	5° ± 1°

The extremely low contact angle hysteresis indicates that the steric hindrance provided by DVB crosslinking is quite effective at reducing contact line adhesion even though the roughness of the surface is appreciable. In contrast, a fluorosilanized surface with an RMS roughness of 1.5 ± 0.3 nm exhibits a contact angle hysteresis of 25° ± 3°. Since the roughness of the fluorosilanized surface is considerably lower than that of the copolymer surface, morphology alone cannot explain the lower hysteresis of the copolymer surface. Instead, we attribute this to the steric hindrance of the crosslinker that prevents the $-CF_3$ groups from shifting away from their low-energy state into the bulk of the film when in the presence of water.

3.1.4 Nucleation density

Environmental scanning electron microscopy (ESEM) was used to compare the microscale condensation behavior of the iCVD and fluorosilanized surfaces. Sample substrates 2 x 2 mm were secured to an aluminum stub with double-sided carbon adhesive and instrumented with K-type thermocouple (Omega) embedded into the tape. The aluminum stub was clamped into a Peltier cooling state (Coolstage Mk II, Deben), which was attached to the stage of an environmental scanning electron microscope (EVO 50, Zeiss). The chamber was purged with water vapor three times up to 3 kPa and down to 10 Pa to remove non-condensable gases. After purging, the pressure was held at 800 Pa and the temperature was slowly decreased at a rate of 0.5 K/min until formation of observable water droplets (> 1 μm diameter). Supersaturations at the onset of condensation were consistently 1.16 ± 0.05. Accelerating voltage was 20 kV and beam current was 100 nA. Images were recorded at 1 Hz and the stage was moved to different areas to avoid charging effects on condensation. Nucleation densities were measured as the mean and standard deviation of at least five different locations on each surface. Representative images of the onset of condensation on p(PFDA-*co*-DVB) and fluorosilane surfaces are shown below in

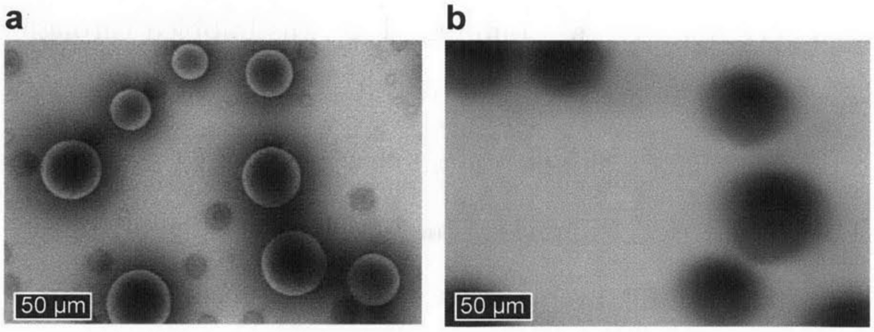

Figure 3-4. **Nucleation density micrographs.** Onset of nucleation on (a) p(PFDA-*co*-DVB) surface and (b) fluorosilane surface, both deposited on a polished silicon substrate and imaged in an ESEM at 800 Pa, supersaturation 1.16 ± 0.05.

For all experiments, the onset of nucleation was not directly observable due to resolution limits of the instrument. Nonetheless, we assume the condensation behavior to remain in the pre-coalescence growth regime[88] and thus the droplet number density when the drops first become observable at a size of 1µm represents the original nucleation density. Droplets became visible at supersaturations of 1.16 ± 0.05. Nucleation densities were measured as the mean and standard deviation of at least five different locations on each of three different iCVD copolymer surfaces to be 173 ± 19 /mm2. This value is considerably higher than that seen on a comparable "smooth" hydrophobic promoter such as fluorosilane (RMS roughness = 1.5 ± 0.3 nm), where the nucleation density was measured to be 110 ± 10 /mm2. Although the crystalline agglomerations seem to contribute negligibly to the contact angle hysteresis, the ~100nm radius concavities at the base of each feature provide nucleation enhancement.

3.1.5 Droplet population distribution

To investigate macroscale shedding behavior and measure the population distribution of condensate droplets, we utilized an atmospheric condensation setup in order to operate at low heat fluxes and facilitate the measurement of single, isolated shedding events. Compressed air was bubbled through a reservoir of deionized water (18 MΩ/cm) and the flow of saturated air was directed normally to the surface of a sample mounted vertically to a Peltier cooling device (SK-12D, Thermoelectrics Unlimited, Inc.). The surface temperature was held between 4-6°C and shedding events (Figure 3-5) were recorded by an SLR camera (Nikon D300s with 105mm Macro lens). Representative images captured during condensation are shown below in Figure 3-5.

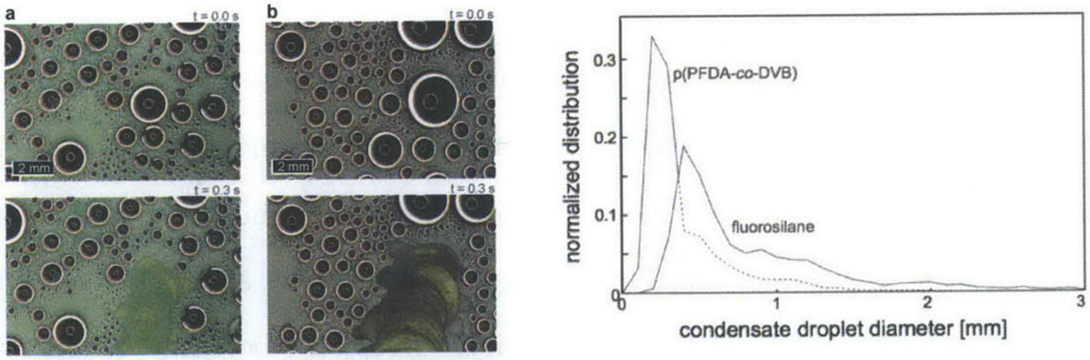

Figure 3-5. **Droplet population distribution**. Photographs of shedding events on (a) iCVD copolymer and (b) fluorosilane surfaces deposited on polished silicon substrates. At right, average normalized population distribution on iCVD copolymer and fluorosilane on silicon substrates.

The departing diameter was determined as the average of 15 individual shedding events to be 2.0 ± 0.3 mm on the iCVD copolymer and 2.9 ± 0.2 mm on the fluorosilane surface, indicating a higher heat transfer coefficient. The advancing and receding contact angles during condensation did not change from the values measured in ambient with a goniometer, suggesting that the drop wets in a Wenzel state in both cases. A Cassie-state droplet would have either exhibited jumping condensation if the Cassie state was maintained during condensation, or would have transitioned to a Wenzel state with higher pinning. The droplet population distribution (Figure 3-5) was measured from 100 images of an area of 2cm x 2 cm recorded over a span of 100 seconds and is shown below in Figure 3-5. The higher nucleation density and lower contact angle hysteresis of the iCVD copolymer both act to shift the population distribution to smaller sizes, indicating better heat transfer performance.

3.1.6 Heat transfer coefficient

To proceed towards an industrially relevant prototype we grafted a 40 nm film of p(PFDA-*co*-DVB) onto 50 mm diameter polished aluminum substrates. Since the adhesion of silanes to copper substrates is substantially poor [89], we did not attempt a comparison of iCVD copolymers and fluorosilane on copper substrates. Polishing was performed using a rotational wheel (RotoPol, Struers) and successive steps of 800, 1200, and 4000 grit carbide paper followed by 3 µm diamond paste and 0.1 µm alumina abrasive. The additional roughness imparted by the metal substrate (RMS = 118 ± 33 nm) is apparent in the AFM height scans (Figure 3-6) and by the notably higher hysteresis: $\Delta\theta = 32° \pm 2°$ on the iCVD copolymer and 31° ± 3° on the fluorosilane surface. The rough metal substrate contributes a substantial amount of pinning, which becomes even more evident during condensation and droplet shedding.

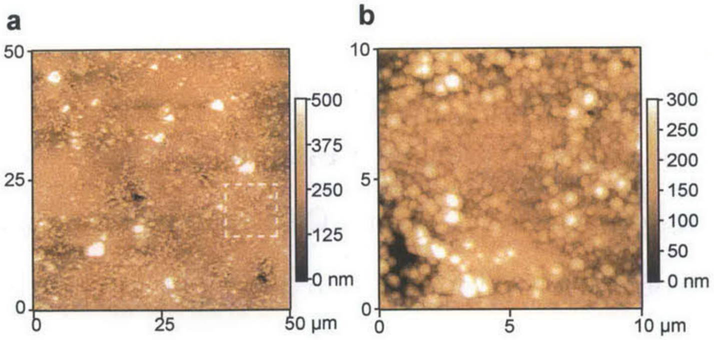

Figure 3-6. **Surface morphology**. AFM height scans of iCVD copolymer deposited on polished aluminum substrate.

When condensing at a pressure of 103.4 kPa (Figure 3-7), departing diameters on the iCVD and fluorosilane surface deposited on polished aluminum substrates are 4.2 ± 0.1 mm and 3.6 ± 0.4 mm. The large discrepancy in departing droplet diameters relative to the contact angle hysteresis could be due to rearrangement of the copolymer at elevated temperatures.

Accordingly, the silanized surface initially displays a heat transfer coefficient of 61 ± 2 $\mathrm{kW/m^2\,K}$, which is larger than that of the iCVD copolymer, which exhibits an initial $h = 38.1 \pm 4.0\ \mathrm{kW/m^2\,K}$. However, whereas the fluorosilane coating degrades after 2 minutes and reverts to filmwise condensation ($h = 4.6 \pm 0.4\ \mathrm{kW/m^2\,K}$), the grafted coating shows no noticeable change in heat transfer coefficient after 48 hours of condensation (Figure 3-7). We propose that the 40 nm film shields the coating/substrate interface from access by steam, while the silane/substrate bonds of the fluorosilane coating are readily hydrolyzed in the presence of high-temperature steam.

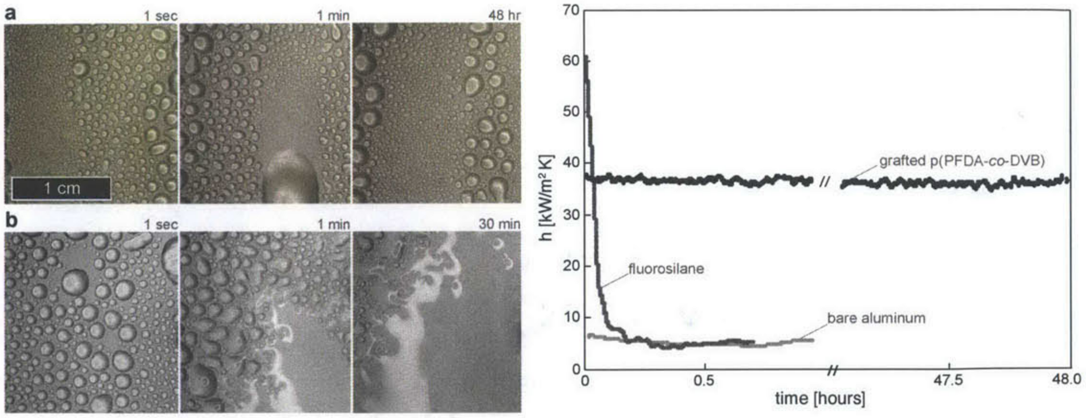

Figure 3-7. **Accelerated endurance test**. Condensation on p(PFDA-*co*-DVB) and fluorosilane deposited on polished aluminum substrate. Condensate shedding on iCVD copolymer (a) over a period of 48 hours and degradation of fluorosilane (b) after 30 min.. Right, heat transfer coefficient of aluminum substrates with no coating, fluorosilane coating, and grafted p(PFDA-*co*-DVB), plotted vs. time.

Grafted polymer films deposited via initiated chemical vapor deposition offer robust hydrophobic functionalization, and lead to durable dropwise condensing surfaces that can sustain prolonged exposure to steam at 100°C while increasing the heat transfer coefficient nearly eightfold from the filmwise value of 4.6 $\mathrm{kW/m^2\,K}$ to the dropwise value of 38.1 $\mathrm{kW/m^2\,K}$. Although longer endurance trials are needed to verify long-term performance, a simple first-order fit to the degradation the heat transfer coefficient of the iCVD copolymer results in a time constant of $O^{\sim}10^{4}$ hours. We envision that these copolymer functionalizations will be employed in a wide array of electronics cooling applications.

3.2 Rare Earth Oxides

3.2.1 Introduction

When a single crystal of metal oxide or ceramic is cleaved, the atoms at the new surfaces are bound to fewer adjacent atoms than before cleavage when they resided in the bulk of the material. This deficiency of bonds at the surface, or surface coordination unsaturation, means that most metal oxide and ceramic materials have a strong affinity for water, since these unsaturated sites provide polar bonding regions for water and other adsorbates:[90]

$$H_2O + M^{n+}O^{2-}M^{n+} \longleftrightarrow M^{n+}OH^{-}M^{n+}OH^{-} \qquad \text{Equation 3-1}$$

The low coordination number of aluminum cations at the surface of alumina, for example, causes these cations to act as Lewis acid sites, and likewise the surface oxygen anions act as Lewis base sites. To satisfy this deficiency in coordination number and obtain a full octet of valence electrons, these sites will then readily form hydrogen bonds with water molecules. This strong interaction gives rise to a clathrate, or hydrophilic, hydration structure, in which three of the four hydrogen-bonding vectors of interfacial water point towards the surface.[91] This is illustrated schematically in Figure 3-8, where the clathrate hydration structure gives rise to strong interaction between both cationic and anionic Lewis bonding sites and results in low, hydrophilic contact angles with water of less than 10°.

The electronic structure of the lanthanide and actinide series, or rare-earth, elements is quite different from that of the transition metals. For these elements, as the 4*f* orbitals are filled with electrons, they remain shielded from interactions by the surrounding $5s^2p^6$ shell.[92] On a rare-earth oxide (REO) ceramic surface, interfacial water can no longer maintain a clathrate hydrogen-bonding network, and so is expected to adopt the configuration shown in Figure 3-8b. In this case, the only hydrogen bond that exists occurs between the OH bond of the water molecule and a surface oxygen atom. The remaining three bonding vectors point away from the surface in a manner similar to a hydrophobic anti-clathrate structure.[91] The hydrophobic wetting state of water observed experimentally on such a surface suggests that this anti-clathrate structure is a governing mechanism in the passivation of an unsaturated rare-earth oxide surface.

To further explore the use of rare-earth oxides as a robust hydrophobic functionalization, surfaces were synthesized and surface properties were analyzed using a variety of techniques including scanning electron microscopy (SEM, JSM-6610LV) for probing morphology, X-ray photoelectron spectroscopy (XPS, PHI 5600 ESCA) for probing crystallinity, X-ray diffraction (SRD, PANalytical X'Pert Pro MPD) to measure ceramic lattice parameter, and Fourier transform infrared/grazing-angle attenuated total reflection (FTIR/GATR, Thermo Scientific Nicolet 6700 FT-IR) to directly probe the structure of interfacial water. The results of these analyses confirmed that the pellets consisted of crystalline grains with characteristic size of 4-10 µm depending on the element with a density of 98%; all samples showed the expected atomic ratio of rare-earth metal and oxygen at the surface, and a diminished FTIR/GATR signal corresponding to ceramic/H_2O hydrogen-bonding peaks on the REO surface compared to alumina, supporting the anti-clathrate hydration structure shown in Figure 3-8.

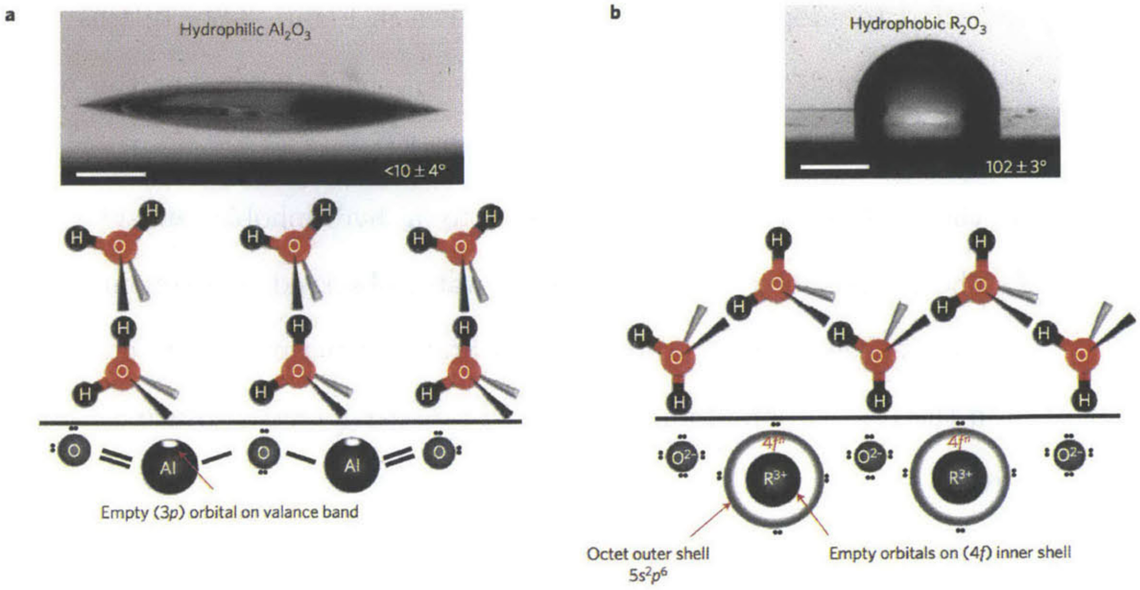

Figure 3-8. **Schematic of orientation of interfacial water on metal oxide surfaces.** (a) Hydrophilicity of alumina arising from clathrate structure: three hydrogen-bonding vectors point towards the coordinatively unsaturated surface atoms of aluminum and oxygen, resulting in low contact angles. (b) Unfilled *4f* bonding orbitals of rare-earth oxide cation are shielded from hydrogen-bonding interactions by $5s^2p^6$ valence orbital, resulting in anti-clathrate hydrophobic structure of interfacial water and corresponding high contact angles. Scale bars in contact angle images: 1mm. Water and ceramic molecules not drawn to scale. Figure from Azimi et al.[65]

3.2.2 Wettability and surface free energy

Contact angle measurements of water on these surfaces (Figure 3-9) show hydrophobic behavior for the entire series of lanthanide oxide ceramic samples, with advancing water contact angles well above 90°. The polar component of surface energy, which is an indicator of the tendency of a surface to form hydrogen bonds, was determined for each of the REO samples using the Oss-Good-Chaudhury equation:[93]

$$\gamma_{l,i}\left(1+\cos\theta_i\right)=2\left(\sqrt{\gamma_s^{LW}\gamma_{l,i}^{LW}}+\sqrt{\gamma_s^{+}\gamma_{l,i}^{-}}+\sqrt{\gamma_s^{-}\gamma_{l,i}^{+}}\right) \qquad \text{Equation 3-2}$$

Briefly, the contact angles of set of three probe fluids (water, ethylene glycol, diiodomethane) were measured on each of the REO surfaces, and the known values of γ^{LW}, γ^-, and γ^+ for the liquid were used to solve for γ_s^{LW}, γ_s^-, and γ_s^+ in Equation 3-2. For all surfaces, the polar component of the critical surface energy was near-zero as shown in Figure 3-9.

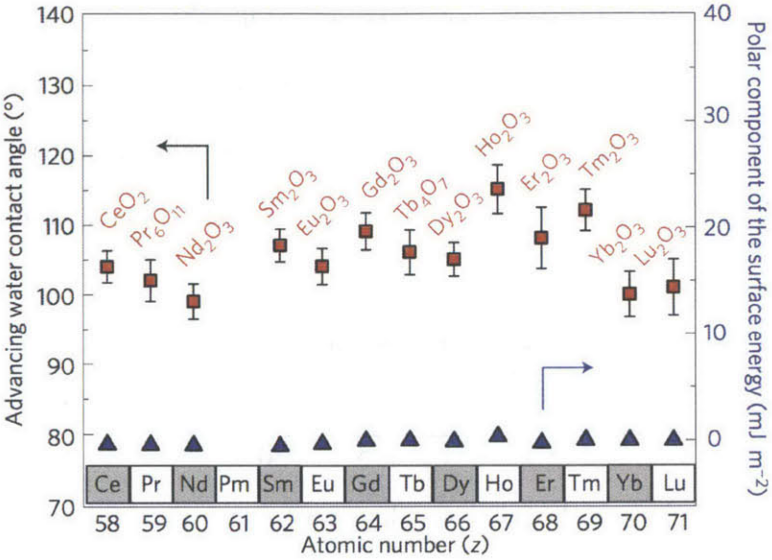

Figure 3-9. **Wettability and surface free energy of REO surfaces.** Advancing water contact angle (left axis) and polar component of surface free energy (right axis). Figure from Azimi et al.[65]

3.2.3 Heat transfer coefficient

To investigate dropwise condensation on REO surfaces, samples were prepared by sputtering thin REO films onto polished silicon wafers. The ultra-smooth silicon surface (RMS < 2nm) was utilized to decouple textural effects from the intrinsic wettability of the REO thin film. Due to the mismatch in lattice parameter and coefficient of thermal expansion between ceria and silicon, an intervening adhesion layer is necessary to avoid delamination of the sputtered film. A CeO_2 target (99.99%, K. J. Lesker) was used to deposit a 300nm layer of ceria onto an 80nm Ti adhesion layer by magnetron sputtering (AJA sputterer, ATC series). Wetting properties

Wettability was measured using the volume addition and subtraction method: a 32g stainless steel dispensing needle was used to deposit a 1μL droplet of deionized water (18MΩ/cm) on the surface using a motorized syringe pump (ramé-hart), and the volume was increased at the rate of 0.1μL/sec up to a volume of 5μL while measuring the advancing receding angle with a goniometer and profile-fitting contact angle software (Model 590 Advanced, DropImage, ramé-hart). Water was then withdrawn at a rate of 0.1μL/sec while measuring the receding contact angle. Wetting properties of the resulting surface are reported below in Table 3-3 as the mean and standard deviation of the mean measured at four locations:

Table 3-3. Water contact angles on ceria thin film sputtered onto polished silicon wafer

θ_a	θ_r	$\Delta\theta$
102° ± 2°	82° ± 5°	20° ± 4°

The ceria sample was bonded to the condensation measurement apparatus described in 2.1. After following the standard non-condensable purging procedure, the steam pressure was increased while flowing cooling water behind the sample surface. Condensing conditions and heat transfer coefficient are reported below in Table 3-4 as the average value and 95% confidence bounds over 10 minutes of condensing at steady-state, defined as a change in parameter value of no more than 0.1%/min.

Table 3-4. Condensation conditions and heat transfer coefficient

parameter	value
P	68.4 ± 1.9 kPa
T_{sat}	81.8 ± 0.8°C
T_s	69.7 ± 0.8°C
ΔT	7.6 ± 0.2°C
q''	485 ± 3.2 kW/m^2
h	63.9 ± 2.0 kW/m^{2}K

4 Superhydrophobic Textures

4.1 Introduction to contact angle hysteresis

The adhesion of liquid drops to solid substrates, whether it be the ratcheting of drops up a bird's beak[94] or the anisotropic wetting on butterfly wings[95] and spider silk[96], is determined by the morphology of the three-phase contact line[97]. Similarly, controlling the mobility of drops and bubbles along surfaces is crucial for many industrial processes, ranging from phase change heat transfer[6,18,98,99] to biomedical devices[100,101]. The dynamic behavior of the contact line is in turn governed by surface heterogeneities that act as pinning sites to produce local deformations, ultimately leading to contact angle hysteresis and the adhesion of a macroscopic contact line[102-105]. Recent studies have highlighted the need for a more complete picture of the contact line across multiple length scales[106,107]. Despite their importance, dynamic imaging of these microscale deformations has been challenging, and particularly elusive in the case of non-wetting drops.

Superhydrophobic surfaces utilize a combination of surface chemistry[108] and texture to promote a Cassie-Baxter (CB) wetting state, in which the drop rests atop roughness features forming a composite interface[48,51,109,110]. Adhesion is substantially reduced in the CB state, particularly when multiple length scales are employed[111], but it is not altogether eliminated. In fact, the adhesion of CB drops represents an almost ideal case of strong dilute defects for investigating the effects of contact line pinning[112]. When a CB drop is moved across a surface, the advancing portion of the contact line simply lies down onto the next roughness features and contributes negligible resistance to drop motion. The deformations due to pinning are localized at the receding region, and as the contact line is displaced, it is hypothesized that micro-capillary bridges are formed at each pinning site[102,113,114]. In order for the contact line to move, the micro-capillary bridges must somehow detach from the surface, either by depinning and receding from each roughness feature, or by necking and rupturing. Although the complete mechanism is not known, the global adhesion of the entire liquid drop is dependent on the detachment of these micro-capillary bridges. After numerous studies[113,115–121], several details of the behavior of these micro-capillary bridges remain uncertain. Currently, models based on per-pillar adhesion force rely on a correction factor[112,122] and computational models rely on the Gibbs criterion being met to result in depinning of the capillary bridges[123]. This latter assumption states that as a contact line recedes around a sharp corner, it will remain pinned until it reaches the intrinsic receding angle[124]. This assumption remains to be validated experimentally, as the microscopic receding contact angle of a Cassie droplet on a superhydrophobic surface has not yet been measured. In a study by Chibbaro et al. [125], the authors investigated capillary filling using three computational methods: molecular dynamics, lattice Boltzmann equations, and computational fluid dynamics. Surprisingly, they found that for a meniscus advancing over obstacles below a certain size, the Gibbs criterion breaks down due to coalescence of the meniscus with nearby condensed molecules. However, these violations of the Gibbs criterion disappear once the obstacles are made large enough. Therefore, it would be important to also experimentally establish the smallest length scale at which the Gibbs criterion is still satisfied. Experimental investigations of wetting and contact angles at very small length scales are rare. Recently, Mirsaidov *et al.* use an electron beam to induce movement of drops of water as small as 10-80 nm in diameter and observe unusually-shaped toroidal drops. Although they did not measure nanoscale contact angles directly, the drops nevertheless exhibited advancing and receding fronts as they moved along a surface.[126] There have been only a handful of experimental investigations of micro-capillary bridges, all high-resolution imaging has been restricted to static drops[113,127–132]. Though some have examined the dynamic behavior, the limited resolution of the three-dimensional details leaves the deformation processes unclear[112,122,133,134]. Furthermore, the effect of multiple length scales on both the behavior of micro-capillary bridges and macroscopic adhesion of drops remains unresolved. Using a novel technique for observing the dynamic behavior of a three-phase contact line and quantitatively measuring contact angles at micron length scales, we show direct evidence that the Gibbs criterion is satisfied at these length scales. We introduce a model that describes a self-similar depinning mechanism and accounts for the effects of the hierarchical roughness features.

4.2 ESEM hysteresis

4.2.1 Experimental setup

Silicon substrates (n-type <100>) were patterned with arrays of square micropillars 10 µm high and 10 µm on a side, with spacings ranging from 3.3-75 µm, using standard positive photolithography techniques and DRIE. By performing a plasma etch with O_2 and SF_6, a silicon nanograss texture was etched into the top surfaces of the micropillar structures. All surfaces were coated with a hydrophobic modifier (tridecafluoro-1,1,2,2, tetrahydrooctyl-trichlorosilane). Advancing and receding contact angles of DI water on silanized smooth silicon substrates were measured with a goniometer (Model 500, ramé-hart) at 25°C to be 120° ± 2° and 90° ± 3°, respectively. Lotus leaves were generously provided by Marilyn Eigsti of Wonderful Water Lilies, Sarasota, FL.

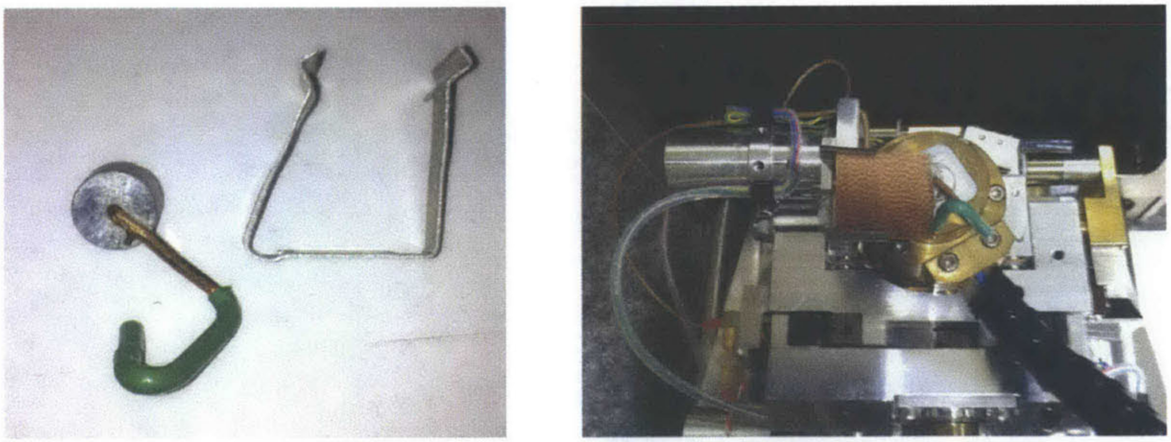

Figure 4-1. **ESEM sample fixture.** (**a**) Aluminum sample coupon holder (right) and copper droplet-restraining wire (left). (**b**) Sample fixture in-place on top of Deben Coolstage showing orientation of droplet-restraining wire before rotation of the entire setup to 90° for ESEM imaging.

A Zeiss EVO-55 ESEM was used for imaging hysteresis and capillary bridge depinning at the microscale. A custom fixture was fabricated to mount the samples vertically in the ESEM and provide cooling with a Deben Coolstage Mk II Peltier cooling stage (Figure 4-1). A 10 µL water drop was affixed to the end of a copper wire that allowed the drop to be held against a vertically oriented surface, and also provided a cooling flux to minimize evaporation. Droplets of water were placed next to the imaging fixture to increase humidity in the chamber. A droplet of water was placed between the rotating wire holder and the fixed sample to provide a deformable thermal interface. By rotating the motorized stage of the ESEM, the droplet was swept across the surface at a velocity of 2 μm / sec while observing the depinning events of the contact line at micron length scales. The chamber of the ESEM was maintained at a pressure of 1000 Pa.

4.2.2 Important observations from SEM images

A single frame from an ESEM movie is shown in Figure 4-2 depicting the formation of capillary bridges. Some important observations can be immediately drawn from the high-resolution images (Figure 4-3). It is clear that the macroscopic contact line is not continuous, but is instead composed of a multitude of microscopic contact lines at the top of each pillar.

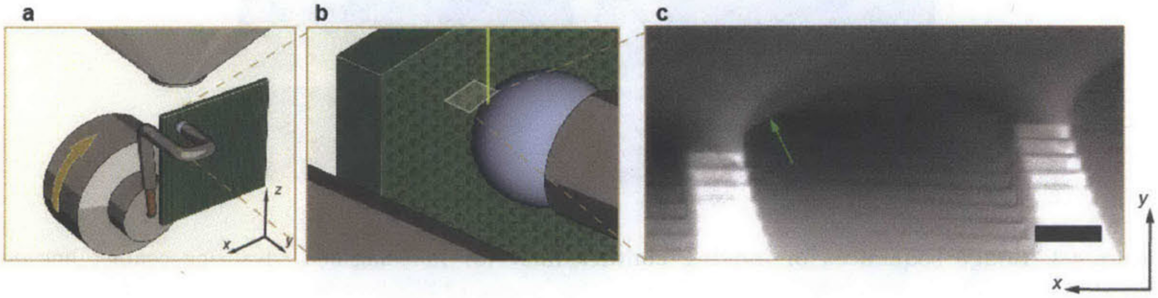

Figure 4-2. **ESEM fixture and movie frame.** **(a)** Experimental apparatus within an ESEM chamber. A water droplet is held against a superhydrophobic micropillar surface by a copper wire. The 10 μL drop is cooled by a Peltier device and swept across the surface (x-direction) by rotating the ESEM stage about the y-axis. **(b)** Illustration of electron beam imaging area with respect to droplet contact line. **(c)** Single frame from movie of water droplet receding along superhydrophobic micropillars in the positive x-direction shows capillary bridge formation. Arrow indicates penultimate capillary bridge. Scale bar, 10 μm.

The difference in behavior between the advancing and receding contact line is apparent in Figure 4-3a, in which the advancing contact line lays down onto the next roughness features with a contact angle of ~180° before advancing further. At the receding contact line, numerous micro-contact lines sit at the bases of capillary bridges, which are stretched vertically until they detach from the pillars.

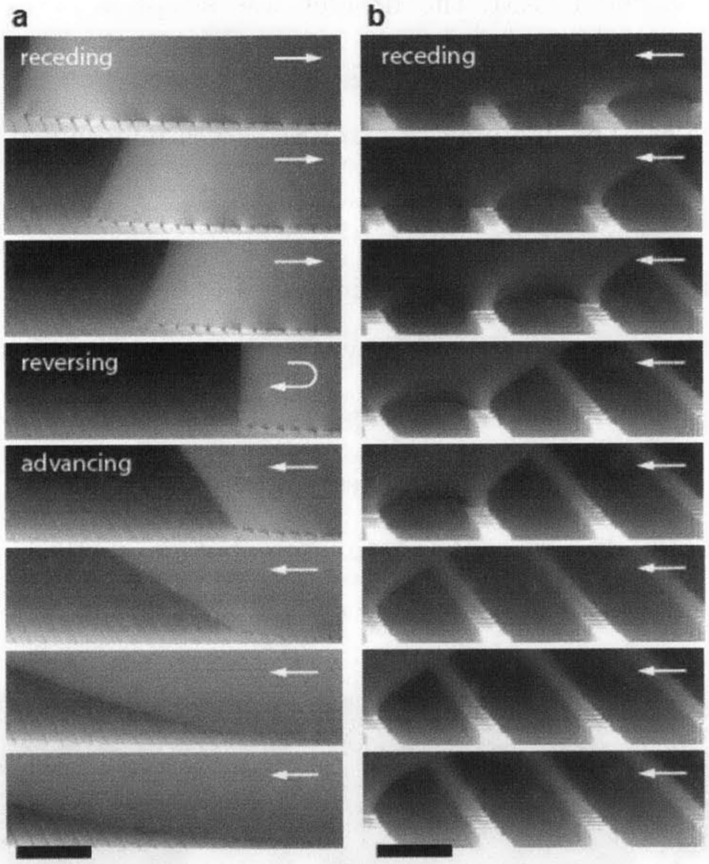

Figure 4-3. **Image sequences of moving contact line.** **(a)** Receding and advancing contact line on micropillar array with 3.3 µm spacing. Arrow indicates direction of drop movement. Scale bar, 50 µm. **(b)** Receding contact line on micropillar array with 40 µm spacing. Arrow indicates direction of drop movement. Scale bar, 50 µm.

The deformations range from severely distorted capillary bridges sitting on top of micropillars at the periphery of the contact patch to smaller distortions at interior micropillars (Figure 4-2c). Because the vapor-liquid interface at the center of the contact patch sags between pillars[135,136], there should be a region over which the vapor-liquid interface is nearly flat as it begins to deform vertically upwards near the periphery of the contact patch. The extent of the deformation depends on the surface tension of the liquid, and on the density and strength of the pinning features. Lower surface tensions should result in only partially-formed peripheral capillary bridges and no interior bridges, as observed recently with cured epoxy drops[130,131]. Nevertheless, we observe fully-formed peripheral capillary bridges that can be approximated as catenoids atop a sharp-edged disk[137,138]. The details of the shape of the multiple catenoids at the base of a spherical drop would be difficult to describe analytically, so we make further simplifying assumptions.

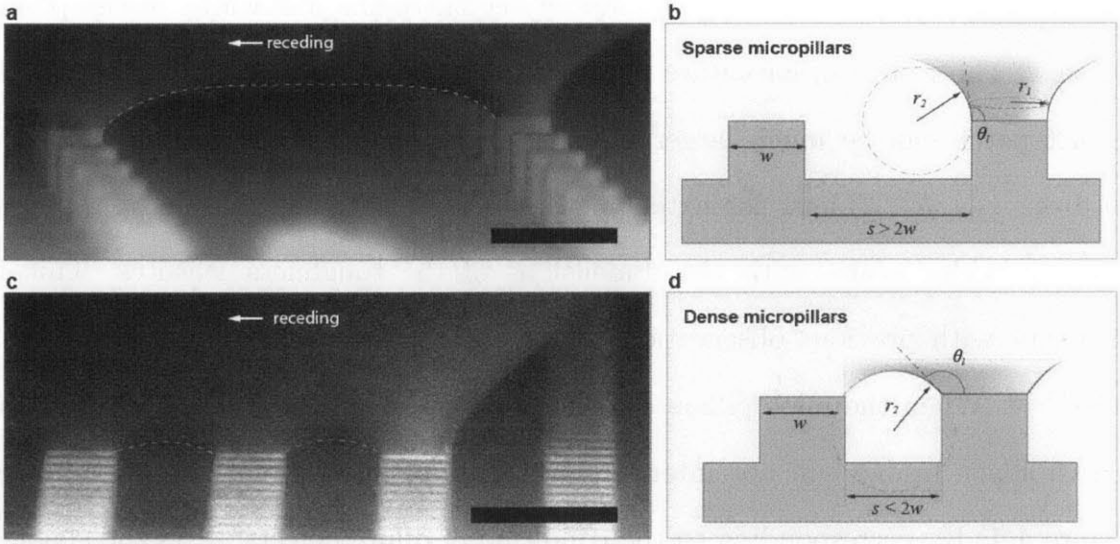

Figure 4-4. **Capillary bridge geometry as a function of roughness feature spacing.** **(a)** Representative ESEM frame showing a water drop receding to the right at a velocity of 2 µm/sec on micropillars spaced 75 µm apart, with profile of capillary bridge highlighted; scale bar: 20 µm. **(b)** Illustration of capillary bridge shape and two principal radii of curvature, and illustration depicting how sparsely spaced capillary bridges do not interact. **(c)** Representative ESEM frame showing a water drop receding to the right at a velocity of 2 µm/sec on micropillars spaced 15 µm apart, with profile of capillary bridge highlighted. Scale bar: 20 µm. **(d)** Illustration depicting how densely spaced capillary bridges interact.

We approximate the capillary bridges in the vicinity of the micro-contact lines to have two constant principal radii of curvature, as highlighted in Figure 4-4: r_1 in the plane of the surface, corresponding to the radius of the bridge, r_2 corresponding to the arch between adjacent bridges. The first radius of curvature is constrained by the pinned micro-contact line to be approximately equal to the half-width of a pillar: $r_1 \sim w/2$. The second radius of curvature can be calculated by considering the mean curvature of the drop. Neglecting the effects of gravity, the mean curvature of the drop H must remain constant everywhere: $H = 2/R$, where R is the radius of the drop. Locally to the capillary bridges, the mean curvature can be estimated by $H = 1/r_1 + 1/r_2$. In the limit that the radius of the drop $R \gg r_1$, the second radius of curvature between peripheral micropillars can attain a minimum value approximately equal to the half-width of the pillar: $r_2 \sim w/2$. The radius of curvature between micropillars close to the center of the contact patch can be much larger than $w/2$, and simply scales as the radius of the drop: $r_2 \sim R$[135]. Thus, the extent of the deformations around each peripheral capillary bridge scales with the dimensions of the roughness features. This is consistent with previous observations of contact line distortions at larger length scales[105,132]. When the micropillars are sparsely spaced ($s > 2w$), the deformations of a capillary bridge will not interact with those of an adjacent capillary bridge (Figure 4-4a,b), corresponding to the condition of dilute defects[102]. As the spacing between roughness features decreases, we see that adjacent bridges begin to interact (Figure 4-4b). This leads to a shorter capillary bridge with a larger contact angle. A similar interaction of menisci has been shown in the case of liquid imbibition through square pillar arrays[139].

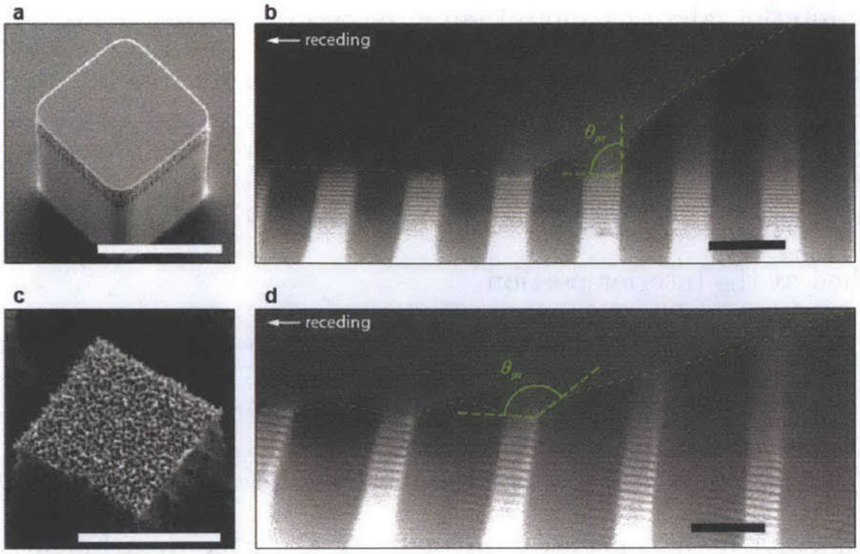

Figure 4-5. **SEM micrographs of micro contact line.** **(a)** SEM micrograph of smooth micropillar. Scale bar, 10 µm. **(b)** ESEM frame of water droplet receding on smooth micropillars with 15 µm spacing. Microscale receding contact angle $\theta_\mu^{\,r} = 86° \pm 5°$ (approximately equal to that on a smooth surface: $\theta^{\,r} = 90° \pm 2°$). Scale bar, 20 µm. **(c)** SEM micrograph of nanograss micropillar. Scale bar, 10 µm. **(d)** ESEM frame of water droplet receding along nanograss-covered micropillars with 25 µm spacing. Microscale receding contact angle $\theta_\mu^{\,r} = 140° \pm 5°$ (Approximately equal to that on a planar nanograss surface: $\theta_{ng}^{\,r} = 145° \pm 3°$). Scale bar, 20 µm.

Most significantly, we are able to directly measure the microscopic contact angle θ_μ at the base of each micro-capillary bridge as shown in Figure 4-5. Our observations show that it can take any value ranging from the advancing contact angle to the intrinsic receding contact angle. The microscopic contact angle reaches a minimum receding value immediately before a capillary bridge detaches from a micropillar: $\theta_\mu^{\,r} = 86° \pm 5°$. This microscopic receding contact angle is consistent across all micropillars and is approximately equal to the intrinsic receding angle on a smooth silanized substrate measured using a goniometer: $\theta^{\,r} = 90° \pm 3°$. This observation indicates that the Gibbs criterion for depinning is indeed met at the top surface of the micropillars. In the current study, the microscopic contact angle at the outer edge of a peripheral micropillar is less than that at the interior edges by more than 5° as seen in Figure 4-5, indicating that a capillary bridge will depin from the outer edge of a micropillar as put forth in recent studies[118,120]. Since the receding angle condition for depinning is always met first on the outer portion of a flat-topped micropillar, the depinning condition is never reached at the interior portion.

To investigate the possibility of satellite drop deposition, we carried out experiments in the ESEM under the same humidity conditions (1000 Pa, Peltier temp. 2°C), but instead of DI water, we used a solution of DI water and CaCl (a deliquescent salt) at a concentration of 0.5 g/L. After detachment, we do not observe deliquescent droplets that would have been the result of necking and rupture of the capillary bridges. This is in agreement with previous studies of single macroscale capillary bridges, in which satellite drops are deposited only when velocities are sufficiently high and receding angle is sufficiently low.[140,141] Capillary numbers calculated from these experiments as $\mathrm{Ca} = \mu V/\sigma$ yield a critical value of $\mathrm{Ca}^* > 10^{-7} - 10^{-9}$ for the deposition of a satellite drop (Table 4-1). The capillary numbers encountered in the current study are sufficiently low ($\mathrm{Ca} \sim 10^{-8}$) as to avoid deposition. Although satellite drops have been observed on other studies,[129–131] this is most likely due to both significantly larger capillary numbers and/or smaller local receding contact angles, which lead to necking and eventual rupture of the capillary bridges. If the detachment velocity is too high, the capillary bridge will form a neck, and the contact line will not be able to recede before the neck ruptures. Furthermore, if the receding angle is much less than 90°, the capillary bridge will be able to form a neck and rupture without reaching depinning condition that is necessary for avoiding a satellite drops. Therefore, the condition for avoiding the deposition of satellite drops is that the detachment velocity is slow enough to allow the contact line to completely depin, and that the contact angle is high enough to depin before forming a neck.

Table 4-1 Satellite drop deposition

Study	**Liquid**	η [Pa s]	σ [N/m]	V [m/s]	θ_r [°]	**Ca**
Krumpfer *et al.*[42129]	dimethylbis(β-hydroxyethyl) ammonium methanesulfonate	0.05	0.066	0.01	152	10
Dufour *et al.*[44130,131]	NOA 72 UV-curable epoxy adhesive, sliding	0.155	0.040	20×10^{-6} [a]	62 ± 2	10^{-6}
	DI water with fluorescent particles, sliding	10^{-3}	0.036	5×10^{-3}	52 ± 2	10^{-3}
	Glycerol, sliding	1.412	0.064	20×10^{-6}	93 ± 2	10^{-4}
Current study	DI water (6.5°C)	1.4×10^{-3}	0.074	2.0×10^{-6}	90 ± 3	10^{-8}

[a] Velocity was not reported by the authors. The epoxy was rolled along a tilted surface, and since the viscosity of the epoxy is less than that of glycerol, is estimated to roll at least as fast as the glycerol drop, and most likely much faster. Therefore a capillary number Ca = 10^{-6} represents a lower bound.

4.2.3 Depinning from hierarchical textures

We imparted a second roughness scale by etching silicon nanograss[142] into the tops of the micropillars while leaving the dimensions of the first scale unchanged. The contact line of a water drop on these samples was observed with the ESEM in the same manner as before. Figure 4-5 shows a comparison of the microscale receding contact angle observed on these two types of surfaces measured immediately before detachment of the right-most capillary bridge. On nanograss-covered micropillars, the microscale receding contact angle increases to $\theta_\mu^r = 140° \pm 5°$ and is about equal to the macroscopic receding angle measured using a goniometer on a sample with only a nanograss texture ($\theta_{ng}^r = 145° \pm 3°$), indicating that the Gibbs criterion is met for each of the two classes of surfaces (smooth micropillars and nanograss-covered micropillars).

4.2.4 Self-similar depinning mechanism

We observe a higher microscale receding angle for the capillary bridges on the nanograss-covered micropillars as compared to the smooth micropillars. We propose that this is due to a self-similar depinning mechanism, for which the total pinned length of the contact lines at each level of the hierarchical roughness must be taken into account.

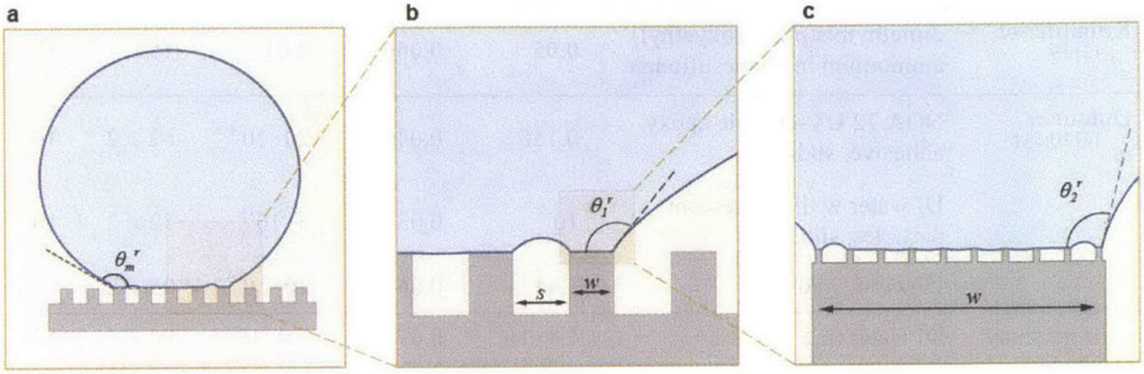

Figure 4-6. **Schematic of self-similar contact line pinning.** **(a)** A liquid droplet that rests in a Cassie-Baxter state on a hierarchical surface exhibits an apparent receding angle θ_0^r. **(b)** The apparent contact line of the drop is divided into many smaller first-level contact lines, each at the top of a first-level roughness feature with width w and spacing s. Each of these first-level contact lines sits at the base of a first-level capillary bridge, which has a local receding angle θ_1^r **(c)** The apparent contact line of each second-level capillary bridge is further divided into smaller second-level contact lines, each atop a second-level roughness feature. Each second-level contact line sits at the base of a second-level capillary bridge, which has a local receding contact angle θ_2^r.

Considering a droplet sitting on a surface comprising multiple levels of roughness features (Figure 4-6a), the apparent macroscopic contact line of the drop comprises the zeroth level of hierarchy and will actually be divided into many smaller contact lines, each sitting on top of a roughness feature at the first level (Figure 4-6b). The receding angle exhibited by the capillary bridges local to the first level of hierarchy θ_1^r will be different from that exhibited by a drop observed at the zeroth level θ_0^r, e.g. macroscopic contact angles measured by a goniometer. The microscale contact angle θ_μ^r on smooth micropillars observed by the ESEM is synonymous with θ_1^r. If the contact lines of these first-level capillary bridges are observed at an even smaller length scale, we hypothesize that they will be divided into even smaller contact lines, each sitting on top of a roughness feature at the second level of hierarchy (Figure 4-6c). The receding angle of these second-level capillary bridges local to the second level of hierarchy θ_2^r will in turn be different from that observed at the first length scale. This self-similar pattern of sub-divided contact lines and differing local contact angles may be continued down successive levels until reaching a level *n* that exhibits a homogeneous wetting interface[25]. At this cut-off level, the contact line on each roughness feature will be continuous. Thus, the actual pinned length of the apparent contact line at any level will be determined by the geometry of the roughness features at all smaller levels, if they exist. If the tops of the roughness features at the cut-off level are also flat, as is the case with the smooth micropillars, the local receding angle should approach the intrinsic receding angle, i.e., $\theta_n^r \sim \theta^r$.

The apparent contact line at any level can be projected onto the tops of the roughness features of the next smaller-scale level. The projected contact line will traverse a number of individual roughness elements, as illustrated in Figure 4-7a in which a portion of a projected contact line traverses seven square micropillars. This hypothetical drop will be pinned to both the peripheral micropillars and the interior micropillars, but significant distortion occurs only at the micropillars that sit directly under the projected contact line. The total pinned length is simply the perimeter of each micropillar P multiplied by the number of peripheral micropillars N. The effective pinned fraction ϕ of a projected contact line of length l can then be found as $\phi = NP/l$. Since the number of micropillars per length N/l is equal to the inverse of the average micropillar pitch τ, the pinned fraction can be rewritten as $\phi = P/\tau$. Thus, if the roughness features are sparsely spaced, only a small fraction of the projected contact line will be pinned (Figure

4-7b, row 1). However, if the pillars are packed densely, then the pinned fraction will increase. In some cases, ϕ may be greater than 1, indicating that the sum of the lengths of the contact lines of the peripheral capillary bridges is greater than the length of the projected contact line (Figure 4-7b, row 2).

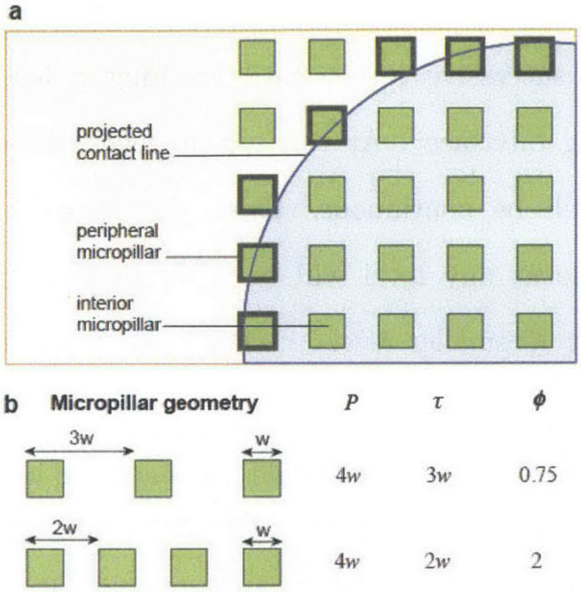

Figure 4-7. **Pinned fraction schematics.** **(a)** A contact line projected on a textured surface will be pinned to a number of peripheral micropillars. **(b)** Effect of texture geometry on pinned fraction. Micropillars with sufficiently dense spacings will result in pinned fractions greater than 1.

The pinned fraction concept can be further applied to structures with multiple hierarchies. Just as the apparent macroscopic contact line of a millimetric drop can be projected onto the tops of the micropillars to obtain the number of peripheral micro-capillary bridges, the contact lines of the micro-capillary bridges can be projected onto the tops of the nanoscale features to find the number of peripheral nano-capillary bridges. The total pinned fraction of a macroscopic contact line at the zeroth level Φ_0 can be calculated for a surface with n hierarchical roughness levels by the product of the pinned fraction at each level:

$$\Phi_0 = \prod_{i=1}^{n} \phi_i \quad ; \quad \phi_i = \frac{P_i}{\tau_i}$$ Equation 4-1

where P_i and τ_i are the perimeter and average pitch, respectively, of the roughness features at the i^{th} level of the hierarchy. The quantity $l_0\Phi_0$ then gives the total pinned length of a projected contact line of length l_0 sitting on a surface with n roughness levels. This total pinned length is equal to the sum of the lengths of contact lines of all peripheral capillary bridges at the n^{th} hierarchical level. Similarly, if we wish to find the total pinned length for a subset of levels starting at $j < n$, we calculate Φ_j by evaluating Equation 4-1 from $i = j+1$ through n:

$$\Phi_j = \prod\nolimits_{i=j+1}^{n} \phi_i$$ Equation 4-2

The total pinned length is then given by $l_j\Phi_j$, where l_j is the perimeter of a roughness feature at the j^{th} level. This is useful, for example, in calculating the total pinned length of an individual micro-capillary bridge sitting on a micropillar that itself has additional finer roughness levels. In this case l_j is equal to the perimeter of the micropillar, and $\Phi_j = \Phi_1 = \prod\nolimits_{i=2}^{n} \phi_i$ is equal to the product of the pinned fractions on the second level and all finer levels. Finally, since the contact line at the n^{th} level is continuous, it is not subdivided any further and the pinned fraction $\Phi_n = 1$.

Surprisingly, Equation 4-1 indicates that adding multiple roughness levels does not necessarily decrease the total pinned fraction. As an example, consider a surface with one roughness scale consisting of sparse micropillars, such that $\Phi_0 = \phi_1 < 1$. If we impart an additional level consisting of sparse nanograss such that $\phi_2 < 1$, then the total pinned fraction becomes $\Phi_0 = \phi_1\phi_2$, which is less than the original pinned fraction. Indeed, for many familiar hierarchical superhydrophobic surfaces such as lotus leaves, there are two roughness scales, and the pinned fraction at both levels is less than one[143]. However, if the nanograss features had been very densely packed such that $\phi_2 > 1$, then the total pinned fraction of the dual-level surface would have been *greater* than that of the single-level micropillar surface: $\phi_1\phi_2 > \phi_1$. This is the case for some nanotube surfaces for which the pinned fraction can be greater than 3, leading to very high droplet adhesion[144].

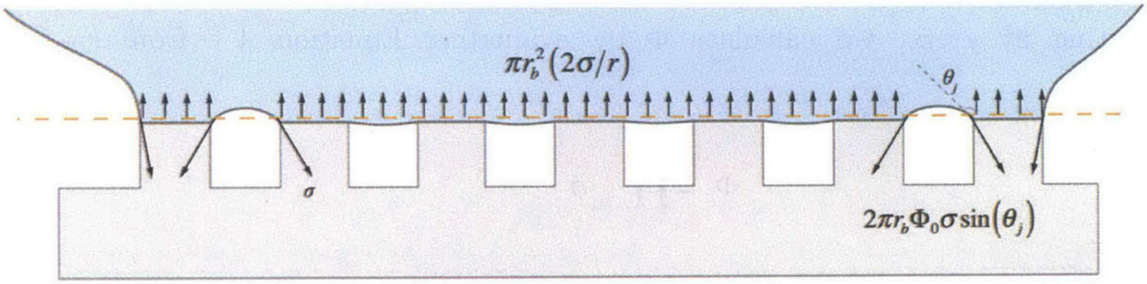

Figure 4-8. **Vertical force balance of a liquid drop.** A plane (orange dashed line) placed just above the tops of the roughness features will only intersect the liquid-air interface at the capillary bridges around the periphery of the drop. The force due to Laplace pressure acting on the plane, given by $\pi r_b^2(2\sigma/r)$, is negligible compared to the detachment force, given by $2\pi r_b\Phi_o\sigma\sin(\theta_j)$.

The adhesion of a drop to a hierarchical superhydrophobic surface with discrete roughness features can be determined by considering the force due to surface tension acting along the bases of the capillary bridges. Considering a liquid drop sitting in a Cassie state on a textured surface, the contact patch will consist of an interior region that sags between the roughness features and a peripheral region that is pulled up between adjacent roughness features. If an imaginary plane is placed just above the tops of the roughness features so that it intersects the drop immediately above the contact line, then the interior portion of the plane will reside completely within the drop, and the peripheral region will intersect the air-water interface Figure 4-8. Gravity is assumed to be negligible for this drop, whose radius is much smaller than the capillary length: $R << \sqrt{\sigma/\rho g}$ and so there will be two principal forces acting on this plane. The first, due to the pressure within the drop, is equal to $\pi r_b^2 (2\sigma/r)$, where σ is the surface tension of the liquid, R is the radius of the drop, and r_b is the radius of the contact patch. The second force, due to surface tension acting along the peripheral roughness features, is equal to $2\pi r_b \Phi_0 \sigma \sin(\theta^r)$, where Φ_0 is the total pinned fraction, and θ^r is the intrinsic receding contact angle. For a static drop, these two forces are equal, and for the experiments in the current study are of the order 1x10^{-7} N. When an external vertical force is applied to the drop, the drop responds by both receding to a smaller contact patch radius and a smaller local contact angle. Both of these effects act to increase the force due to surface tension above its original value for the unperturbed drop. We argue that since the force due to the internal pressure of the unperturbed drop is more than two orders of magnitude smaller than the final detachment force (F > 1x10^{-5} N), the force due to pressure may be neglected in the vertical force balance leading to Equation 4-2. By considering a vertical force balance on the drop, the adhesion of the entire drop is predominantly dictated by the vertical component of surface tension acting at the peripheral capillary bridges. The force pinning a single capillary bridge at the j^{th} level can be written as $F_j = \int_{P_j} \sigma \sin(\theta_j) ds$, where P_j is the perimeter of an individual roughness feature onto which the bridge is pinned, σ is the liquid-vapor surface tension, θ_j is the contact angle local to j^{th} level, and ds is a differential length along the perimeter. In the present case, to estimate the maximum adhesion force before detachment, we approximate the contact angle as being uniform around the entire perimeter of the micropillar and equal to the receding angle local to the j^{th} level θ_j^r, so the previous expression simplifies to $F_j = P_j\sigma\sin(\theta_j^r)$. If there exist additional roughness levels, the adhesion of the j^{th}-level capillary bridges will be determined by depinning of capillary bridges at the smaller levels. This will in turn affect the value of θ_j^r.

Due to the mechanism of self-similar depinning, the adhesion of the entire j^{th}-level bridge will be governed by the detachment of the capillary bridges atop features at the n^{th} level. Since the local receding contact angle at this final level θ_n^r will be approximately equal to the intrinsic receding angle θ^r, the vertical force exerted by a single n^{th}-level peripheral capillary bridge due to surface tension will be $P_n\sigma\sin(\theta^r)$, where P_n is the perimeter of a roughness feature at the n^{th} level, and θ^r is the intrinsic receding contact angle. Finally, the vertical adhesion force of the entire drop can be found by summing the forces due to all of the peripheral n^{th}-level capillary bridges:

$$(F/l)_0 = \Phi_0\sigma\sin(\theta^r) \qquad \text{Equation 4-3}$$

where l_0 is the length of the projected macroscopic contact line. By normalizing the vertical adhesion force predicted by Equation 4-3 to the adhesion force of a drop with an equivalent base radius on a smooth surface, given by $(F/l)_s = \sigma\sin(\theta^r)$, the resulting ratio $(F/l)_0/(F/l)_s = \Phi_0$ suggests that Φ_0 can be considered as a multiplier that reflects the strength of the pinning on the textured surface as compared to that on a smooth surface. Therefore, when $\Phi_0 > 1$, the adhesion force per unit length of a contact line on a textured surface should be greater than that on a smooth surface, and vice versa. Due to self-similarity, the adhesion force per unit length of a single capillary bridge atop a feature at the j^{th} level is the same as that of a macroscopic drop sitting on a surface consisting of a texture with levels $j+1$ through n:

$$(F/l)_j = \Phi_j \sigma \sin(\theta^r) \qquad \text{Equation 4-4}$$

In other words, the adhesion force per unit length of the microscopic contact line of a micro-capillary bridge on a single nanograssed micropillar is the same as that of a macroscopic drop on a surface with just a nanograss texture.

4.2.5 Error analysis

We have made a simplifying assumption that for the case of water on silanized silicon pillars, capillary bridges are formed on only the peripheral micropillars with a nearly uniform contact angle around the entire micropillar. As noted, the contact angle is not uniform all around the pillar, but differ by as much as 5°. The error in the adhesion force of a single capillary bridge is given by:

$$\frac{\delta F}{F} = \frac{1}{F}\frac{\partial F}{\partial \theta^r}\delta\theta^r = \frac{\cos(\theta^r)}{\sin(\theta^r)}\delta\theta^r \qquad \text{Equation 4-5}$$

The error is 7.1% when $\theta^r = 86°$ and $\delta\theta^r = 5°$, which represents the worst-case error, and so we believe this assumption to be appropriate for the case of water on silanized silicon. However, this assumption will not be appropriate with other liquid/solid systems that have different contact angles, e.g. as seen with the epoxy drops imaged by Dufour et al.[130,131] In that case, the contact angle differs by almost 90° from the outside to the inside of the roughness feature, so we would need to evaluate the integral given in the general expression for pinning force.

The high humidity and low temperatures of the ESEM experiments were needed to minimize evaporation rates, and any error in comparing the results to the macroscale adhesion experiments conducted at room temperature need to be taken into account. The ESEM instrument used in this study is constrained to an upper operating pressure of 3000 Pa, but the poor resolution at this pressure warrants imaging at pressures as low as possible. 1000 Pa was chosen as a tradeoff between better image resolution at lower pressures and lower evaporation rates at higher pressures. The saturation temperature of water at 1000 Pa is 6.97°C, and since the ESEM chamber walls surrounding the sample are at room temperature (~20°C), both the water drop and the sample experience a radiative heat flux. To counter this positive heat flux, a negative heat flux is provided by means of a Peltier cooling stage. The drop is held by a copper wire so that the incident radiative heat flux may be conducted away into the Peltier stage. Likewise, the textured samples are in thermal contact with the Peltier stage so that the incident radiative heat flux is also conducted away. Despite these efforts, it was not possible to completely eliminate evaporation of the drop. The evaporation rate of a drop of water held in the ESEM under the reported humidity conditions (P = 1000 Pa, $T_{Peltier}$ = 2°C) was measured to be approximately 5 pL/s.

As a consequence of the low temperature, the surface tension of water is higher than at the room temperature conditions reported in most other studies. The contact angle will also change with temperature. However, both of these effects are quite small. The error in Equation 4-3 with respect to error in surface tension and contact angle is given by:

$$\frac{\delta F}{F}=\frac{1}{F}\sqrt{\left(\frac{\partial F}{\partial \theta^r}\delta\theta^r\right)^2+\left(\frac{\partial F}{\partial \sigma}\delta\sigma\right)^2}=\sqrt{\left(\frac{\cos(\theta^r)}{\sin(\theta^r)}\delta\theta^r\right)^2+\left(\frac{\delta\sigma}{\sigma}\right)^2} \quad \text{Equation 4-6}$$

The error in Equation 4-3 due to temperature difference between an ESEM temperature of 6.5°C (slightly below saturated temperature) and room temperature is 2.8%, and so temperature effects are considered to be negligible.

4.2.6 Macroscopic adhesion measurements

To validate our hypothesis of self-similar depinning, we compared the adhesion force predicted by Equation 4-3 to experimental observations. Using a tensiometer, we measured the force required to pluck a millimetric drop vertically off of two types of surfaces: smooth micropillars and nanograss-covered micropillars. A Sigma KSV 700 tensiometer was used to measure the adhesion force of water drops on superhydrophobic surfaces (Figure 4-9). A 3 µL drop was held at the end of the force balance and lowered onto a test surface at 0.5 mm/min until a compressive force of 1 µN was measured, indicating contact with the surface. The drop was then lifted at 0.5 mm/min until detachment, at which point the tensile force and contact patch radius were measured. Measurements were repeated at five locations on each sample.

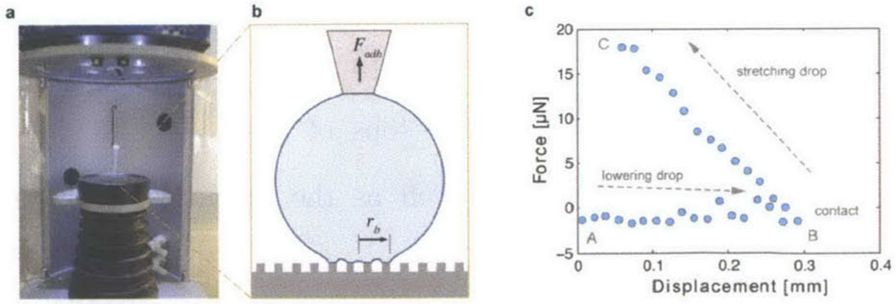

Figure 4-9. **Tensiometer adhesion measurements.** **(a)** Photograph of experimental apparatus. **(b)** Schematic illustration of drop held at the end of a pipette tip while in contact with a textured surface. The drop contact patch has radius r_b. **(c)** Typical force-displacement curve for an adhesion trial. The drop begins at some distance above the surface (A) and is lowered until it makes contact (B). The pipette tip is then raised slowly to stretch the drop vertically until detachment (C).

There is a significant decrease in adhesion of the nanograss-covered micropillars as compared to the smooth micropillars. Additionally, as the spacing ratio s/w increases, the density of micropillars and the adhesion force both decrease. For both the smooth and nanograss-covered micropillars, the pinned line fraction at the first level is given by $\phi_1 = 4w/(w+s)$. In the case of the nanograss-covered micropillars, there is a second roughness level (n=2) at a nanometer scale with a pinned fraction $\phi_2 = 0.18 \pm 0.05$.

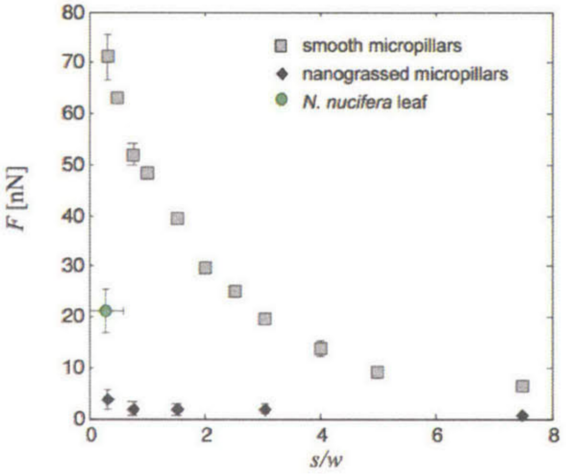

Figure 4-10. **Macroscopic adhesion measurements.** Adhesion force vs. spacing ratio for smooth micropillars, nanograss micropillars, and a *N. nucifera* leaf.

High-resolution SEMs were used to estimate the pinned fraction of the silicon nanograss. The perimeters of the tops of the roughness features were identified and measured manually, as well as the distances between adjacent roughness features. A representative frame is shown in Figure 4-11. The pinned fraction was taken as the average of the perimeters of the roughness features divided by the average distance between the centroid of each feature. A pinned fraction of 0.18 ± 0.05 was determined as the average value from five SEM images taken at different locations (Figure 4-11).

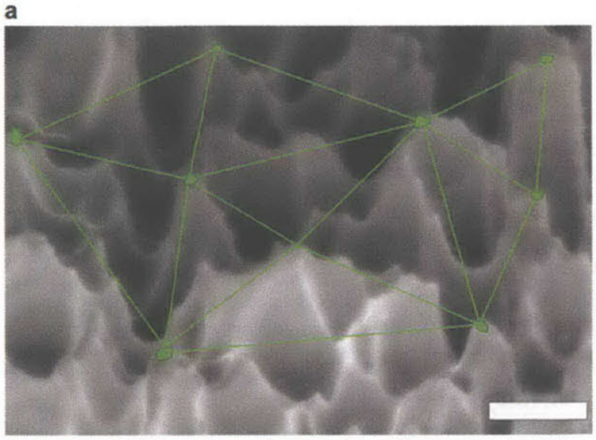

Figure 4-11. **Silicon nanograss pinned fraction.** (a) A representative frame depicting manual identification of roughness feature perimeter and average spacing. Image was taken at a tilt angle of 53°. Scale bar is 300 nm.

Figure 4-12 shows $(F/l)_0/(F/l)_s$ - the measured adhesion force per unit projected length of the contact line of a macroscopic droplet normalized to that on a smooth surface - vs. the total pinned fraction Φ_0. For both single- and dual-hierarchy surfaces, and even the lotus leaf, the data collapse onto the line predicted by Equation 4-3. There is a deviation at denser pillar spacings because the roughness features are no longer in the regime of sparse defects, and the peripheral capillary bridges begin to interact with one another. This leads to a larger local receding angle between adjacent pillars as shown in Figure 4-4b, thus we would expect the vertical component of surface tension to decrease. Indeed, we find that the normalized adhesion at larger pinned fractions ($\Phi_0 \geq 1.5$), which corresponds to the regime of dense spacings, is lower than that predicted by Equation 4-3.

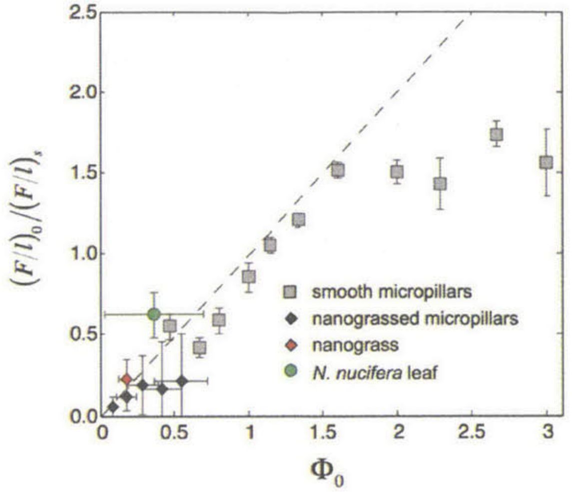

Figure 4-12. **Macroscopic adhesion measurements normalized to force on smooth surface.** Ratio of measured adhesion force per unit length of the contact line of a macroscopic drop to that on a smooth surface vs. total pinned fraction for smooth micropillars, nanograss micropillars, flat nanograss, and a *N. nucifera* leaf. Deviation at large pinned fractions is due to interaction of capillary bridges. Dotted line indicates the ratio as predicted by Eqn. 2. Error bars indicate standard error.

The effect of the second level of hierarchy can be cancelled by normalizing the measured vertical adhesion force per unit projected length of the contact line of a macroscopic drop from Equation 4-3 $(F/l)_0 = \phi_1\phi_2\sigma\sin(\theta^r)$ with the force per unit length of a capillary bridge on top of the micropillars from Equation 4-3 evaluated at $j=1$ $(F/l)_1 = \phi_2\sigma\sin(\theta^r)$ to obtain the ratio $(F/l)_0/(F/l)_1$. Hence, plotting $(F/l)_0/(F/l)_1$ against ϕ_1 should yield similar results for both smooth micropillars and nanograssed micropillars, as the effect of the texture on top of the micropillars is cancelled. Indeed, Figure 4-13 shows that the normalized adhesion forces measured on nanograssed micropillars match well with those measured on smooth micropillars, and as predicted, both lie along a line with a slope of 1. Furthermore, the normalized adhesion forces on the nanograssed micropillars display a similar plateau due to capillary bridges interacting at the microscale level, as seen with the smooth micropillars. However, since the receding angle local to the micropillars is greater for the nanograssed micropillars, they will begin interact at wider spacings than for smooth micropillars and exhibit normalized adhesion forces that are lower than predicted. One might expect that adding any additional level of microtexture to the nanograss would have decreased the adhesion force per unit length. Interestingly, we find that the normalized adhesion of nanograssed micropillars with small s is greater than that of a surface with just a nanograss texture. This can be explained by realizing that the total pinned fraction involves the product of the pinned fractions at both levels, and since $\phi_1 > 1$ for $s < 30$ µm, we see how dense nanograssed micropillars ($\phi_1 \geq 1.5$) can exhibit greater normalized adhesion per unit length than a surface with just a nanograss texture.

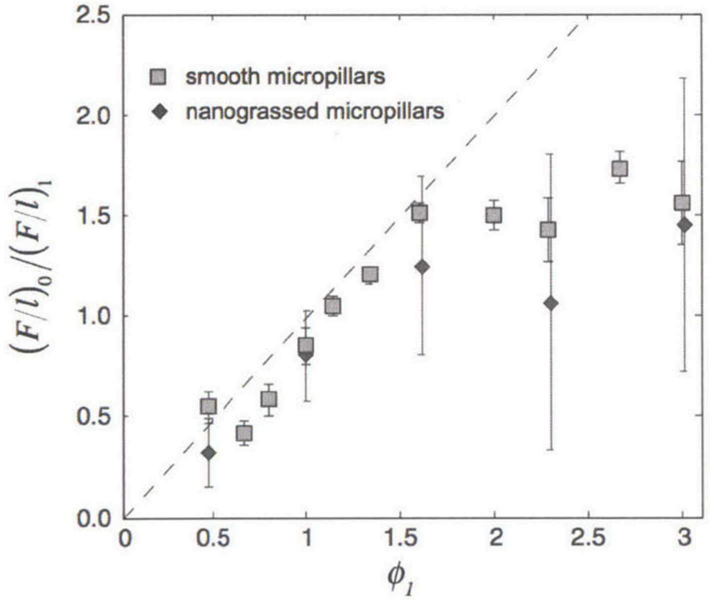

Figure 4-13. **Macroscopic adhesion measurements normalized to force on first hierarchy.** Adhesion force per unit length of projected contact line of a macroscopic drop normalized to remove the effect of the nanograss hierarchy, plotted against the pinned fraction at the first hierarchy. For the case of nanograssed micropillars, $(F/l)_0$ was obtained by measuring the adhesion force of a drop on a nanograss surface and normalizing with the projected length of the contact line. For the case of smooth micropillars, $(F/l)_0$ is simply $\sigma \sin(\theta^r)$. Dotted line indicates the normalized force as predicted by Equation (2). Error bars indicate standard error.

This result is counterintuitive, and shows how additional roughness levels will decrease the adhesion force per length only if the pinned fraction at that level is less than one. As the pinned fraction of a particular level is increased beyond one, that level will act to increase the adhesion force per unit length. However, the adhesion force will saturate when the pinned fraction at that level reaches a critical value ($\phi_i \geq 1.5$ in the current case) above which the capillary bridges at that level begin to interact.

The model described in Equation 4-4 shows that the adhesion force per unit length of the projected contact line may be either increased or decreased by adding multiple length scales of roughness depending on the pinned fraction of each level of hierarchy. This finding is important for designing surfaces with minimal adhesion, e.g. optimal roll-off behavior, since it quantifies the effect of multiple length scales on the adhesion of a liquid drop on a textured surface: in order to reduce adhesion, the product of the pinned fractions at all length scales must be less than one. Furthermore, two micropillar geometries that have identical area fractions may have different pinned fractions depending on their perimeter and spacing, and any attempt to calculate pinning or hysteresis based on area fraction would yield identical results for the two surfaces. In agreement with our mechanism, experiments have shown that the hysteresis differs depending on the micropillar perimeter and tip geometry[113,129,144]. Our technique could also enable the detailed imaging of contact line behavior on complex pillar geometries and on intricate biological surfaces such as water strider legs[145] and fiber arrays[146].

4.3 Jumping Condensation

Recently, Dorrer and Ruhe[14] and Chen et al.[18] observed that during condensation on sufficiently small-scale superhydrophobic surfaces, drops with sizes significantly below the capillary length depart the surface via spontaneous droplet motion. The prospect of enhancing the condensation rate by decreasing the maximum departure diameter, which could significantly increase the heat transfer coefficient has generated much interest and research effort in condensation on superhydrophobic surfaces.

Boreyko and Chen[18] initially reported that hierarchical superhydrophobic surfaces, which consist of both nanoscale and microscale topological features, are necessary to promote spontaneous drop motion. More recently this mode of condensation has also been observed on surfaces with only a nanoscale roughness hierarchy.[20,46,142,147–150] Rykaczewski et al.[42,46] found that the primary role of the nanostructure is confinement of the base area of nucleating droplets, which leads to formation of nearly spherical microdroplets through contact angle increase. In a subsequent work, Enright et al.[150] reached a similar conclusion by studying the effect of the nanoscale superhydrophobic surface architecture on later stages of microdroplet growth. Similarly, Liu et al.[151] found in their theoretical study that the nanostructure is crucial for formation of high contact angle microdroplets. Rykaczewski demonstrated that the forming droplets grow in purely constant base area mode until reaching a contact angle of 130° to 150°. Miljkovic et al.[41] found that the growth rate of droplets in the wetting Wenzel state is much higher than of those in the nonwetting Cassie-Baxter state. This behavior is primarily due to a significant increase in the base area of droplets, and with that number of silicon pillars in contact with the liquid, when the drops transition from the Wenzel to the Cassie-Baxter state.

The effects of microscale topography, separately from that of the smallest-scale and often nanoscale topography, on coalescence dynamics during condensation on hierarchal superhydrophobic has only been explored theoretically by Liu et al.[151,152] and experimentally by Chen et al.[17] Using thermodynamic analyses, Liu et al. predicted that the microscale topography should influence the final wetting state, apparent contact angle, rolling angle, and departure diameter of a condensed drop. Chen et al. focused on how the microscale topography affects cumulative departure volume and drop number density. In this work, we investigate the impact of microscale topography on the droplet coalescence dynamics and wetting states during the condensation process.

In this chapter we image condensation occurring on hierarchical superhydrophobic surfaces consisting of truncated microscale cones with varied dimensions and pitch covered by deep-reactive ion etched silicon nanograss[17] across multiple length and time scales using high speed light microscopy. We show that isolated mobile and immobile coalescence between two drops, almost exclusively focused on in previous studies, are rare. The majority of coalescence events on hierarchical superhydrophobic surface occurs in series and leads to coalescence of multiple droplets. These drops can merge locally or be sequentially swept up in a serial chain of coalescences. Such multi-drop serial coalescence events are triggered by mobile coalescence events resulting in formation of a droplet departing with significant tangential velocity component that subsequently collides with another neighboring or distal drop. Regardless of the number of coalescence drops, the serial coalescence events culminate in formation of a drop that either departs or remains anchored to the surface. We quantify the frequency of formation of the departed and anchored drops in different size regimes as a function of the microscale topography. We explain the observed post-coalescence drop adhesion trends through direct correlation to formation of drops in nanoscale as well as microscale Wenzel and Cassie–Baxter wetting states. We find that optimally designed hierarchical superhydrophobic surfaces, which promote the highest number of departing microdrops, consist of microscale features spaced close enough to enable transition of larger droplets into micro-Cassie state, yet at the same time provide sufficient spacing in between the features for occurrence of mobile coalescence.

4.3.1 Experimental procedure

4.3.1.1 Superhydrophobic Surface Fabrication

The microscale features were patterned using standard photolithographic procedures: tetramethylammonium hydroxide (TMAH) was used for anisotropic etching of silicon. Because the etching rate of the $\langle 100\rangle$ plane was significantly faster than of the $\langle 111\rangle$ plane, the $\langle 111\rangle$ plane defined the microscale features, resulting in a 54.7° angle between the etched wall and the flat surface. The etching rate of the $\langle 100\rangle$ plane using 25% TMAH solution at 80 °C was about 0.33 μm/min. The truncated cone-like silicon pillars were fabricated by carefully adjusting the etching time. Afterward, the silicon nanograss was fabricated using a modified Bosch deep reactive ion etching (DRIE) process. First, a thin film of fluoride polymer was deposited on the solid surface in the passivation cycle, followed by etching cycle. We carefully tuned the ratio of the etching and passivation times to leave behind residual polymer particles that served as a random mask for subsequent etching. The nanograss was formed via alternating etching and passivation steps. The coil power was set to ~550 W. The chamber pressure and temperature was kept at 4 Pa and 20 °C. In the passivation cycle, the C_4H_8 flow rate was ~85 sccm. In the etching cycle, the SF_6 flow rate was 70 sccm and platen power was set to 15 W. Nanograss features with a typical diameter of about 400 nm, pitch of about 700 nm, and height of about 2.6 µm were produced after 20 processing cycles. All the surfaces were modified by immersing in 1 mM hexane solution of trichloro-(perfluorooctyl)-silane for 30 min, followed by heat treatment at about 150 °C in air for 1 h.[153] This procedure resulted in a uniform coating of the nanostructures with the hydrophobic layer. Flat silicon wafers modified using this procedure had a static water contact angle of about 110°. SEM images of typical nanograss structures and the hierarchical superhydrophobic surface are shown in Figure 4-14, panels a and b—e, respectively. The dimensions and wetting parameters for these hierarchal superhydrophobic surfaces are specified in Table 4-2. Henceforth, we identify each of the surfaces by the center-to-center distance between the microscale features (i.e., P-120 stands for the superhydrophobic surface with 120 µm center-to-center distance; P-0 refers to the surface consisting only of nanograss texture).

Table 4-2. Hierarchical surface texture dimensions and wetting roughness parameters.

sample	P	H	D_b	D_t	θ_a	θ_r	φ	$r_{\mu W}$	$r_{\mu C}$	r_{nC}	$r_{n\mu C}$
P-120	120	14	51	34	165.3°	161.0°	0.13	1.07	0.06	0.26	0.016
P-64	64	12.6	49	27	164.8°	162.8°	0.32	1.17	0.14	0.26	0.036
P-40	40	14	27	7.3	163.8°	159.3°	0.2	1.25	0.026	0.26	0.007
P-30	30.2	13.4	23.8	5.4	165.5°	162.3°	0.25	1.35	0.025	0.26	0.007
P-0					164.3°	144.8°	0.26				

[a] Unless otherwise specified, the units are in micrometers. P, H, D_b, and D_t stand for center-to-center distance, height, and bottom and top diameters of the microscale features, whereas θ_a, θ_r, φ, and r refer to the macroscopic advancing contact angle, receding contact angle, volumetric solid fraction, and the Cassie or Wenzel wetting parameters at the specified length scale.

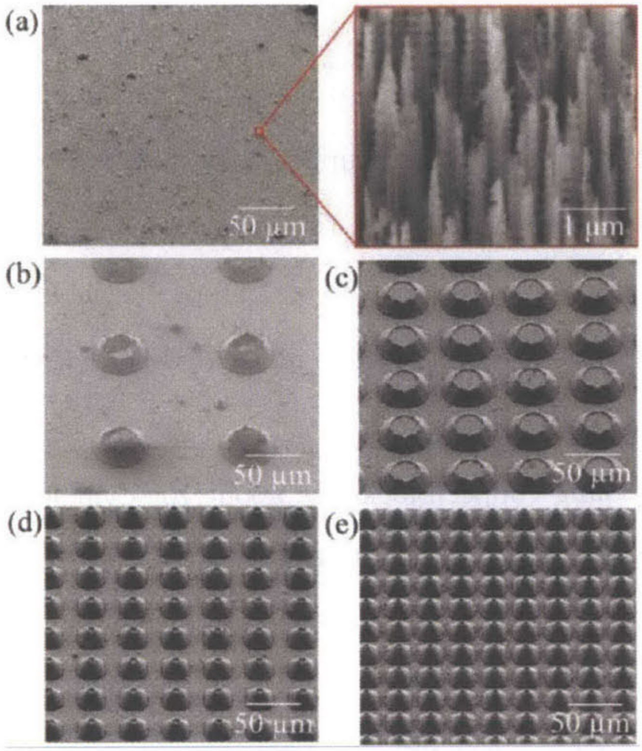

Figure 4-14. **SEM images of texture detail.** (a) surface consisting only of nanograss (P-0), and (b–e) hierarchical superhydrophobic surfaces consisting of nanograss and truncated microcones with a center-to-center distance of (b) 120 μm (P-120), (c) 64 μm (P-64), (d) 40 μm (P-40), and (e) 30 μm (P-30). The samples were inclined at an angle of 52° with respect to the surface normal.

The macroscopic contact angles were measured with a goniometer (ramé-hart model 590) using volume addition and subtraction method. First, a 1 **μ**L sessile drop of deionized water with resistivity of 18 MΩ/cm was deposited on the surface. To measure the advancing contact angle, measurements were taken while water was added to the drop at a rate of 0.1 **μ**L per second. The receding contact angles were measured while volume was withdrawn from the drop at the same rate. All reported values were averages of measurements taken in four different locations on the samples. The uncertainties, which were calculated with a coverage factor of 1, were 4° for the P-0 surface and 1° for all other surfaces.

Macroscale condensation experiments were performed in a custom built condensation apparatus described in Section 2.1. The superhydrophobic substrates were affixed to a copper cooling block using copper adhesive tape to ensure adequate thermal contact. The other side of the copper cooling block was cooled by a flow of chilled water supplied by a heat exchanger (Neslab II, Thermo Scientific). Before condensing, the chamber was evacuated to a pressure below 13 Pa to minimize the effect of non-condensable gases. Steam was introduced to the chamber by an electric boiler (SR-20, Reimers Boiler Co.) at a constant pressure of about 75 kPa and temperature of about 92 °C. While the subcooling of the cooling copper block was about 10 °C, it is difficult to estimate the subcooling of the superhydrophobic surface because of the unknown thermal resistance of the tape adhesive and the sample itself. Videos were recorded at 500 frames per second and 12000 frames per second by a high-speed camera (SA-1, Photron) equipped with a zoom lens (Model 6265, Navitar) and illuminated by a concentric ring light (Dolan-Jenner). For comparing condensation characteristics of the different surfaces, droplet size distribution was analyzed during later stages of condensation process dominated by coalescence regime.[88] From the videos recorded at 500 frames per second, ~3000 frames were extracted. From these, every 100th frame was subsequently analyzed using ImageJ after performing image segmentation and thresholding. To obtain droplet size distribution, droplet diameters were categorized with intervals of 30 μm. For each interval, the number of droplets in that range occurring in all the analyzed frames were counted and divided by the total number of droplets in all the analyzed frames to obtain the percentage distribution of that droplet size. Thus the droplet size distribution averaged over a period of time could be obtained for each surface for purposes of comparison. The diameters of droplets involved in isolated and serial coalescence events in 500 frames (two sets of 250 frames selected from the ~3000 frames for each surface) were measured manually. For the drops that remained anchored to the surface, the final drop diameter and number of coalescence drops was recorded. For the coalescence events that culminated in drop departure, the final drop diameter was estimated from the measured diameters of the coalescence drops.

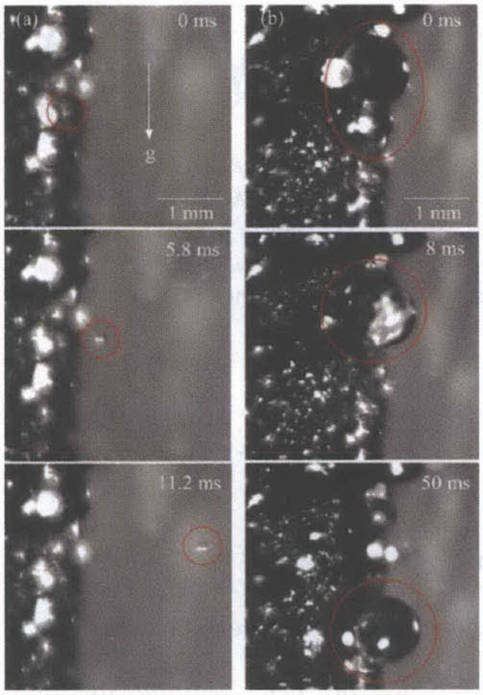

Figure 4-15. **Confirmation of jumping condensate departure.** High speed light microscopy showing examples of mobile coalescence water droplets on P-40 superhydrophobic surface resulting in (a) out-of-plane droplet ejection and (b) rolling or shedding with gravity.

To confirm the occurrence of mobile coalescence events, we imaged the condensation process at 12000 frames per second using a high-speed camera placed on the side of the superhydrophobic surface. The images in Figure 4-15a show post-coalescence out-of-plane droplet motion, but the images in Figure 4-15b show that after coalescence larger droplets can also roll or shed with gravity in the vicinity of the surface. In the following sections we describe in depth our investigation of the impact of microscale topography on the droplet coalescence dynamics and wetting states during the condensation process.

Top-down imaging of the condensation process using high speed optics revealed several droplet shedding modes (see Figure 4-16). These events can consist of multiple neighboring drops coalescence locally (Figure 4-16a) or drops being sequentially swept up in a domino-like process across distances of even several millimeters (Figure 4-16, panels a– f). The multi-drop coalescence events were likely triggered by mobile coalescence, resulting in formation of a flying droplet that subsequently collided with another neighboring or distant drop (see Figure 4-16, panels a, c, and g–i). The spontaneous droplet motion is typically described as being purely normal to the surface,[152,154] but to trigger the serial coalescence the droplet motion must possess a tangential component (see schematics in Figure 4-16, panels f and g). The tangential component of the droplet's motion could be caused by coalescence of uneven sized drops, pre-coalescence tangential movement of one of the drops, or asymmetric adhesion of the droplets to the microscale topological features. Once triggered, the domino-like serial coalescence can sweep up droplets in any direction. For example droplets in Figure 4-16a–c and Figure 4-16d were swept with and against gravity while those in Figure 4-16e were swept laterally. However, we observed that serial coalescence events involving drops with diameters larger than about 300 μm typically resulted in the drops shedding with gravity. Also, such drops did not necessarily sweep up all droplets in their path (Figure 4-16, b and c), but it was difficult to determine whether in the sweeping mode the droplets remained in contact with or were slightly detached from the substrate. Irrelevant of the mode, ultimately the isolated and serial coalescence events resulted in formation of a drop that had either departed or remained anchored to the surface (Figure 4-16, panels h vs i).

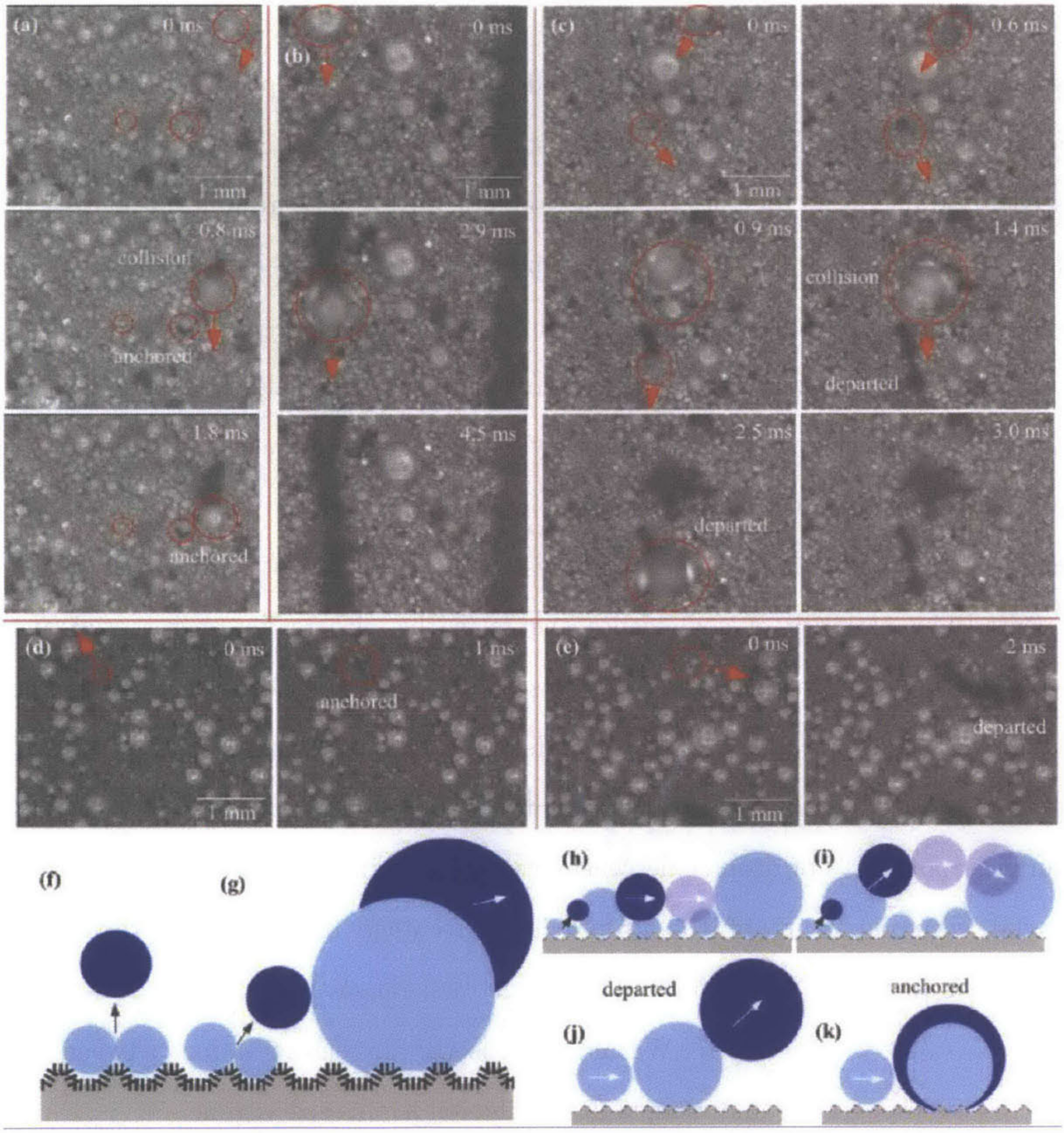

Figure 4-16. **Multiple-drop coalescence and tangential departure.** High-speed light microscopy images showing examples of serial coalescence events resulting in coalescence of multiple droplets that culminate in formation of (a and d) an anchored drop and (b, c, and e) a departed drop. Note that large droplets can depart the surface in shedding mode as in (b) as well as in jumping mode in (c and e); Schematics of mobile coalescence involving two drops with (f) purely out-of-plane motion and (g) motion containing a tangential component which results in collision and dislodging of neighboring droplet, which in turn can trigger (h) domino-like sweeping coalescence or (i) non-localized collision coalescence, both of which can culminate in formation of a (j) departed or (k) anchored drop.

To study post-coalescence drop adhesion to the hierarchical superhydrophobic surface, we quantified the number of serial coalescence events which culminated in formation of a drop which had departed or remained anchored to the surface from 500 high speed optical images collected during one second of operation of the condensation apparatus. The results presented in histograms in Figure 4-17 specify the number of drops involved in these events as well as the diameter range of the final droplet (30–100, 100–200, and above 200 µm). These results highlight the predominance of serial coalescence events over isolated coalescence events. Specifically, isolated coalescence events occurred almost solely for droplets with merged diameter in the 30–100 µm range and even in this size regime comprised of at most 15% of the total drop coalescence events. The majority of coalescence events in this size regime were serial and involved between three and six droplets. For the P-0, P-120, P-40, and P- 30 about 30% of the drop coalescence events that produced drops with diameters in the range 30–100 µm ended with departure of that drop. In contrast, on the P-64 surface about 60% of drop coalescence events producing drops in this size regime ended with departure of the drop. The percentage of departing drops with diameters in the 100–200 µm and above 200 µm ranges varied from 0% to 45% and 0% to 63%, respectively. We did not observe any clear relation between the microscale topography and merged drop adhesion in this size regime.

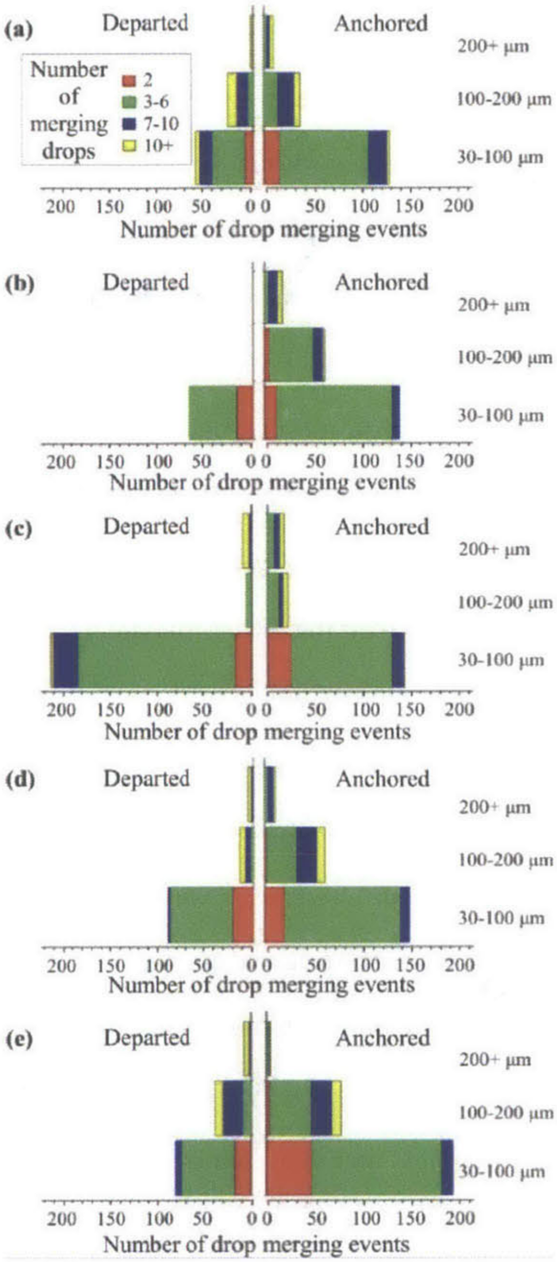

Figure 4-17. **Quantification of droplet departure events.** Analysis of binary (2 drop) and serial (more than 2 drops) drop coalescence events culminating in formation of a drop in the range of 30 to 100 µm, 100 to 200 µm, and above 200 µm regime which departed or remained anchored to the (a) P-0, (b) P-120, (c) P-64, (d) P-40, and (e) P-30 surfaces during one second of condensation in the condensation apparatus. The number of droplets involved in the droplet coalescence events is also indicated.

To gain an insight into the physical mechanism of post-coalescence drop adhesion to the superhydrophobic surface, we investigated the droplets wetting states occurring on these surfaces. Following Verho et al.,[155] we distinguished droplet wetting of the nanoscale and the microscale topological features illustrated in Figure 4-18a as nano-Wenzel, nano-Cassie, micro- Wenzel, and micro-Cassie states. We note that droplets in the micro-Cassie and micro-Wenzel states can also locally wet the nanostructure through formation of nanoscale capillary bridges. Miljkovic et al.[41] and Rykaczewski et al.[42,46] previously observed formation of micro-droplets with diameters below ~20 µm in the nano-Wenzel as well as the nano-Cassie states. We confirm their results with the side-on ESEM images in Figure 4-18, panels c and d, which clearly show droplets in both of these wetting states. The final wetting state of the micro--droplets depends on the location of nucleation of nano-droplets, which combine to form the larger droplets. The side-on ESEM image in Figure 4-18b demonstrates that the nano-droplets can nucleate on bottom as well as on top of the nanograss, yielding micro-droplets in nano-Wenzel and nano-Cassie states. Irrelevant of the wetting state, micro-droplets with diameters greater than 10 µm grow primarily by coalescence with neighboring droplets. Coalescence of two micro-droplets in the nano-Cassie state is much more likely to result in the post-coalescence motion.[41,152] If a micro-droplet in the nano-Wenzel state is involved in a coalescence event, it can serve as an anchor and prevent the newly formed drop from moving.

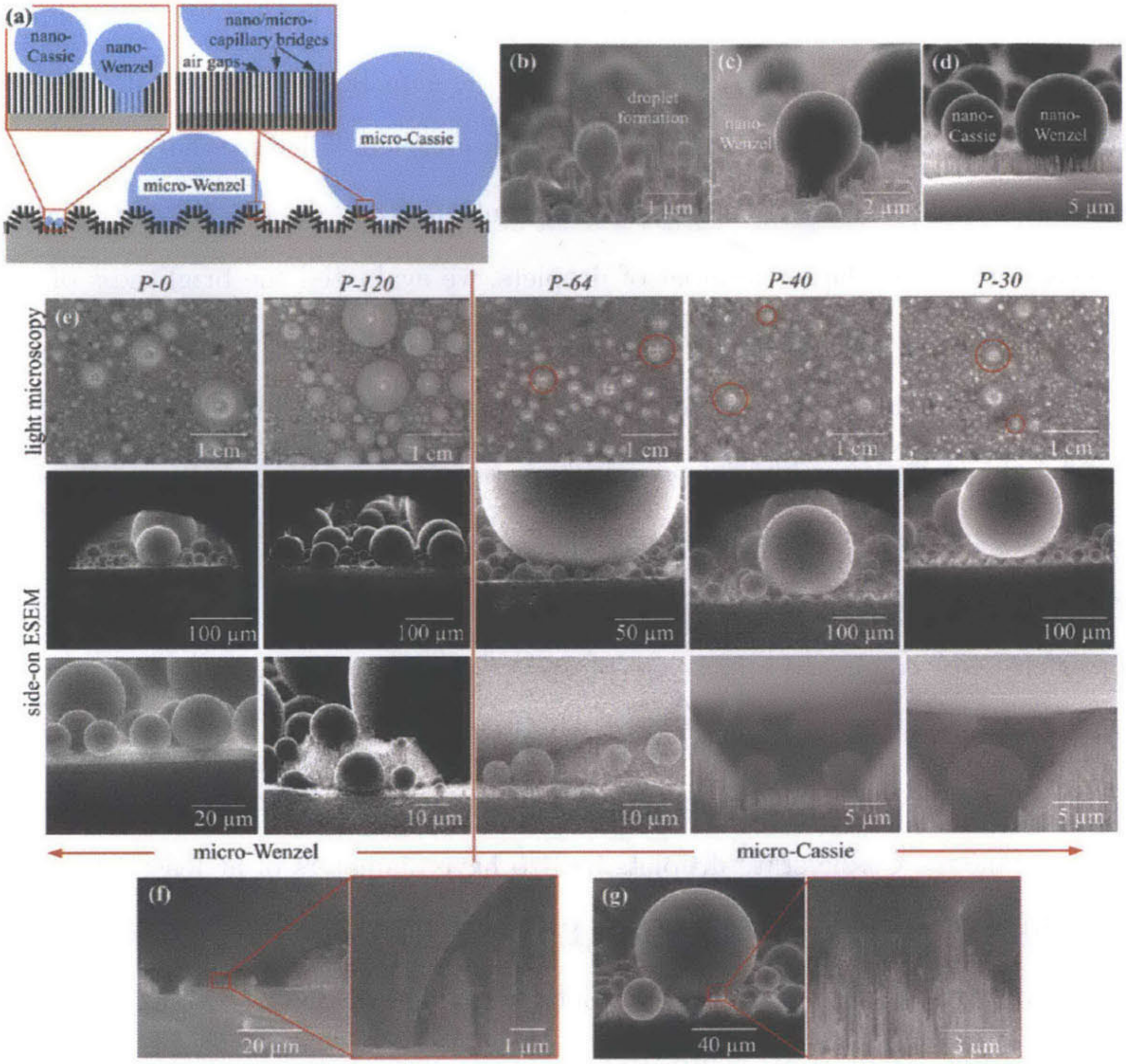

Figure 4-18. **Wetting states on different scales.** Possible wetting states of droplets condensed on a hierarchical superhydrophobic surface: (a) representative schematic, (b–d) side-on ESEM images of example droplets condensed on the nanotrees in nano-Wenzel and nano-Cassie states, (e) light microscopy and side-on ESEM images of water droplets in micro-Wenzel and micro-Cassie states; the red circles mark smallest observable drops in the micro-Cassie state, and (f and g) close-up examples demonstrating formation of capillary bridges between larger droplets and the nanoscale topography.

We observed that formation of droplets in the micro-Wenzel and the micro-Cassie states is intimately related to the geometry of the microscale topography. The close up ESEM images in Figure 4-18e clearly show that large droplets on the P- 64, P-40, and P-30 surfaces can bridge tops of the microscale features without penetrating the space between them. Moreover, we were able to image formation of multiple smaller droplets within the gaps below the large droplet. In contrast, on the P-120 surface all the larger droplets filled-in the volume in-between the microscale features. To confirm the direct side-on ESEM observations with a larger number of droplets, we evaluated the brightness of the droplets observed using top-down light microscopy. Droplets in the micro-Cassie state appear brighter because they have a smooth bottom water-gas interface and reflect light in a mirror-like specular fashion (see Figure 4-18e). In turn, droplets in the micro-Wenzel state appear darker because they have a rough bottom interface and reflect light in a diffuse fashion (see Figure 4-18e). Using this approach, we confirmed that the micro- Cassie state occurs only on the superhydrophobic surface with the center-to-center distance of the microscale features equal or smaller than 64 μm. Furthermore, we observed that in order to be in the micro- Cassie state droplets had to have diameters of at least 120−160, 100−140, and 80−120 μm on the P-64, P-40, and P-30 superhydrophobic surface, respectively. In other terms, the droplets had to have diameters two to three times greater than the center-to-center distance between the microscale topological features. We also observed that on the micro-Cassie enabling surfaces the maximum observed drop diameter is only ~500 μm as compared to the ~1000 μm observed on the P-120 and the P-0 surfaces. However, not all larger droplets formed during sequential coalescence events on the micro-Cassie enabling surfaces departed because of the nanoscale capillary bridges forming between the drop and the tops of the microscale features (see Figure 4-18, panels f and g). A random number of these capillary bridges form due to coalescence with satellite micro-droplets in nano-Wenzel state.[55,156] The capillary bridges significantly increase the local adhesion force and thus can act as anchors preventing merged droplet departure.

We re-evaluated the post-coalescence drop adhesion on the hierarchical superhydrophobic surface in light of the wetting states of condensed droplets. Specifically, we plotted the absolute size data in Figure 4-17 in scaled form of merged droplet diameter to microscale topography center-to-center distance ratio ($\boldsymbol{d_{drop}/P}$). The cumulative number of departed and anchored drops are plotted in Figure 4-19a and b. We observe that irrelevant of their absolute number, the cumulative number of departing drops saturates for all samples at d_{drop}/P ratio of two to three. Since this value of d_{drop}/P is also the minimum threshold for occurrence of the micro-Cassie state, we used to define a border between "small" and "large" merged drops in the histogram in Figure 4-19c. No large droplets depart the P-120 surface, because they remained anchored in the "sticky" micro-Wenzel state. In contrast, on all of the micro-Cassie enabling surfaces about 20—25% of the drop coalescence events resulted in formation of a large drop that departed the surface (see Figure 4-19d). This general observation implies that adhesion of Cassie-state droplets condensed on hierarchical superhydrophobic surface is governed by the number of microscale features in contact with the drop. For the small droplets, the percentage of departed drops was unaffected by the microscale topological features with the exception of P-64 surface. On this hierarchical superhydrophobic surface the fraction (Figure 4-19c) and the total number of small departing drops (Figure 4-19a) was two to three times higher than on any of the hierarchical superhydrophobic surface as well as the solely nanostructured P-0 surface (25—35% of drops depart this surface after coalescence). This trend is also reflected in the rather uniform drop size distribution curve for the P-64 surface in Figure 4-19d. Because of their efficient shedding, the percentage of small drops on the P-64 surface is less than on the other surfaces.

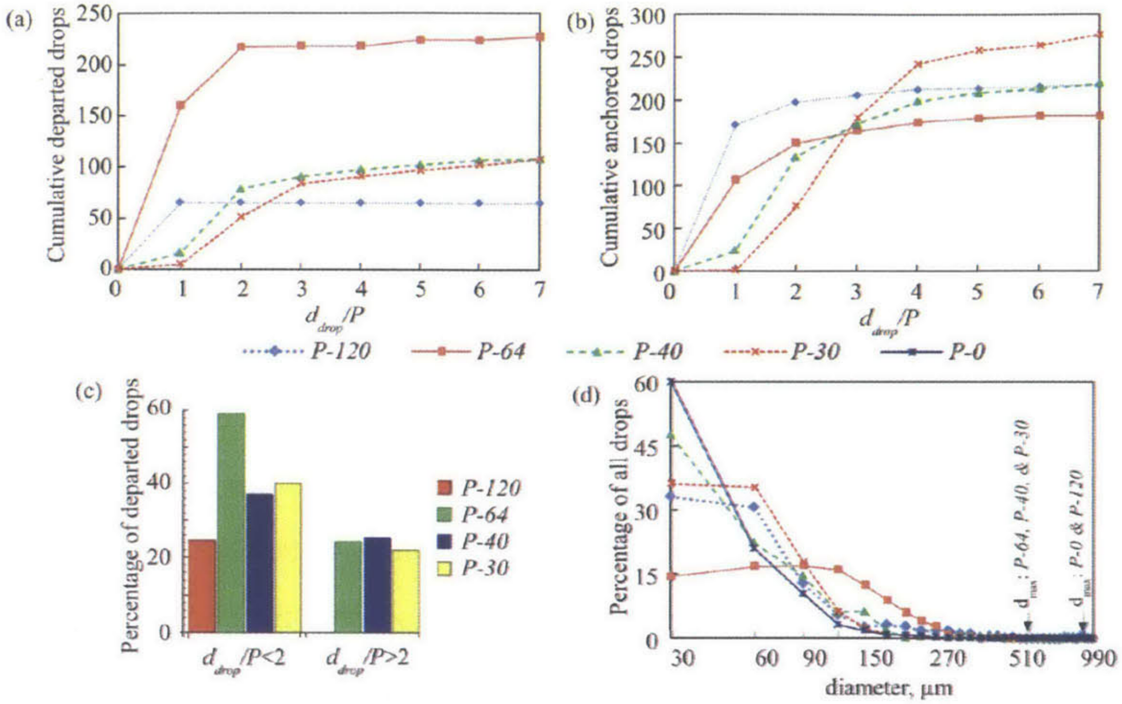

Figure 4-19. **Cumulative droplet departure diameter.** Cumulative number of drops which have (a) departed or (b) remained anchored to the surface in terms of the ratio of the drop diameter to the microscale feature center-to-center distance (d_{drop}/P), (c) Percentage of drops with diameters below or above the $d_{drop}/P = 2$ threshold which have departed the surface, and (d) Size distribution of drops with diameters above 30 µm for P-0, P-120, P-64, P-40, and P-30 surfaces. An individual point refers to the percentage of total drops on the surface that have diameters within 30 µm interval starting at the value of the point.

The microscale topological features on the P-64 surface are spaced closely enough to enable transition of large droplets into the micro-Cassie state, while at the same time providing sufficient space in-between the features for coalescence of two small droplets with diameters above d_{th} (see Figure 4-19b). As a result mobile coalescence can occur between two small drops condensed in-between the features. Consequentially, the mobile droplets can trigger numerous multi-drop coalescence events that lead to formation of easily departing drops in the micro-Cassie state. In contrast, the schematic in Figure 4-19a illustrates that on surfaces with P <

2dth (P-40 and P-30 superhydrophobic surface), only micro-droplets with diameter below dth can coalesce in- between the features, decreasing the number of mobile coalescence events between small drops. In addition the probability of mobile coalescence events decreases in this case because the edges of the microscale topological features are more prone to defects in the nanostructure. Lastly, despite large solely nanostructured area, we do not observe numerous small departing drops on the P-120 surface because large fraction of the area is occupied by large droplets in immobile micro-Wenzel state.

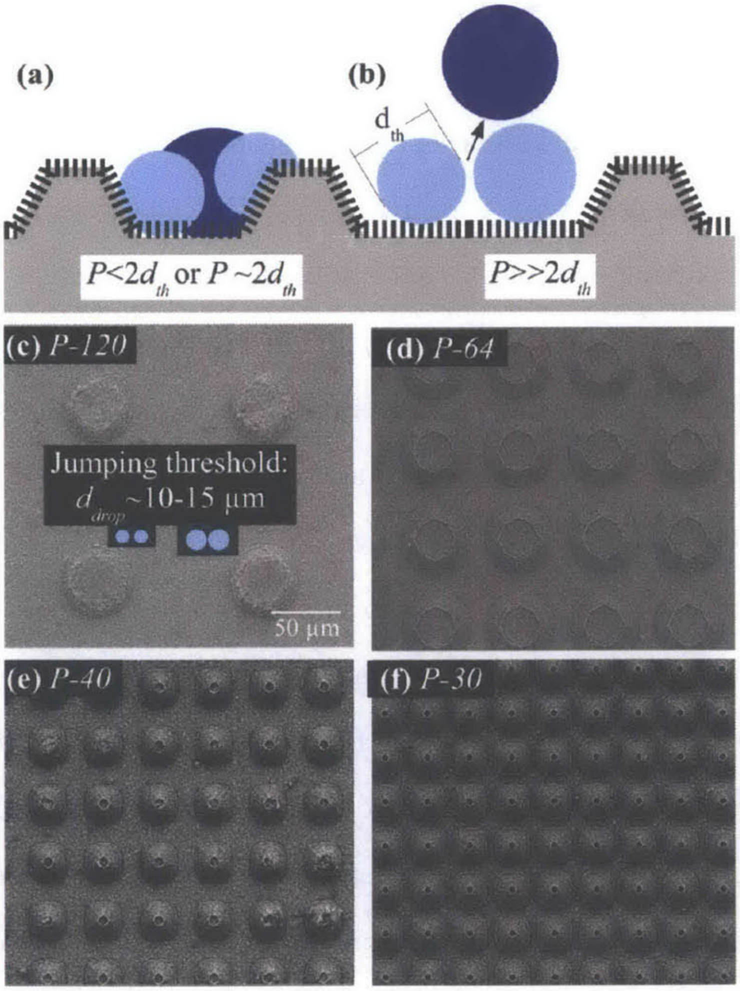

Figure 4-20. **Departure diameter threshold.** Schematic showing the relation between postcoalescence mobility of droplets with ddrop/P = 2 on hierarchical superhydrophobic surface with the center-to-center distance of the microscale topological features (P) (a) equal to or smaller and (b) greater than two times the

mobile coalescence threshold diameter (dth); (c–f) top-down SEM images of P-120, P-64, P-40, and P-30 surfaces and schematic showing two pairs of drops with diameters of 10 and 15 μm.

In this work we explored the relation between droplet coalescence dynamics, droplet wetting states, and the micro- scale topography of the underlying hierarchical superhydrophobic surface. We showed that for mobile coalescence to occur between two droplets on any of the superhydrophobic surface, the drops need to have diameters of at least 10 to 20 μm. However, we also showed that coalescence of two drops producing a drop with diameter above 30 μm is infrequent as compared to serial coalescence events involving three or more drops. The multi-drop coalescence events occurred when neighboring droplets combined or when drops were sequentially swept up in a domino-like process. These novel droplet shedding modes were triggered by mobile coalescence resulting in a tangentially departing droplet that subsequently collided with another neighboring or distant drop. Irrelevant of the mode, the serial coalescence events culminated in formation of a drop that either departed or remained anchored to the surface. Analysis of post-coalescence adhesion of drops with diameters in the 30–100, 100–200, and above 200 μm ranges demonstrated strong influence of the microscale feature geometry; however no clear trend was evident from the data presented in these absolute terms. To gain an insight into the post-coalescence adhesion data, we studied the effect of the microscale topology on the wetting states of the condensed droplets. We confirmed that micro-droplets can be in nano- Wenzel and nano-Cassie states, dependent on the location of nanodroplet nucleation on the nanostructure. The capillary bridges connecting droplets in the nano-Wenzel state to the substrate were likely responsible for occurrence of immobile coalescences between two small microdrops. Next, we found that drops condensed on hierarchical superhydrophobic surface with microscale feature center-to-center distance equal or less than 64 µm did transition into the micro-Cassie state. In order to transition into this microscale nonwetting state the drops had to have diameters two to three times greater than the center-to-center distance between the microscale topological features. Rescaling of the postcoalescence drop adhesion data in terms of merged diameter to microscale feature center-to-center distance ratio revealed clear trends. Specifically, if a hierarchical superhydrophobic surface architecture did not promote formation of drops in the micro-Cassie state, the postcoalescence drop adhesion was dramatically increased as compared to solely nanostructured surface. In turn, on micro-Cassie state enabling architectures about 20−25% of droplets with $d_{drop}/P > 2$ departed after coalescence with other drops. The formation of drops in a micro- Cassie state also correlated to a decrease in the maximum observed diameter from ~1000 µm to ~500 µm (P-0 and P- 120 vs P-64, P-40, and P-30 superhydrophobic surface). For droplets with $d_{drop}/P < 2$, about 25−35% of drops formed in a drop coalescence event departed the P-0, P-120, P-40, and P-30 superhydrophobic surface, while 60% departed the P-64 superhydrophobic surface. The architecture of the P-64 surface is optimal for shedding microdroplets because it enables higher mobility of droplets with $d_{drop}/P > 2$ through formation of Cassie state while at the same time provides sufficient spacing in-between the microscale features for mobile coalescence of two droplets with diameters above d_{th}.

5 Lubricant-Imbibed Textures

5.1 Steam condensation

Since Cassie droplets have minimal contact with the surface, they can be easily shed.[157] However, under condensation, many natural and synthetic superhydrophobic surfaces display poor drop mobility due to nucleation of droplets within texture features (Figure 5-1a, b) that ultimately results in sticky, Wenzel droplets (Figure 5-1c).[49,50,158–160] To overcome these limitations, hybrid hydrophobic-hydrophilic surfaces that promote Cassie condensation and micro-nano textures that promote coalescence-induced self-propelled dropwise condensation have been developed.[18,142,161] Though promising, these approaches require surface textures with intricate designs and morphologies that are vulnerable to damage and defects. Furthermore, although this technique is applicable to working fluids with large surface tension such as water, it is unlikely that a superhydrophobic state could be maintained when condensing low-surface tension fluids.[162]

In this chapter we present an alternate approach to promote dropwise condensation in which the condensing surface is microscopically textured and imbibed with a lubricating liquid immiscible with the condensed liquid (Figure 5-1d). Such surfaces have recently been shown to display low contact angle hysteresis, self-cleaning, self-healing by wicking upon damage, repellency to variety of liquids and anti-icing properties.[60–62] Furthermore, the shedding velocity of droplets from such surfaces has been shown to be inversely dependent upon viscosity.[63] In this chapter we show that by appropriately choosing the lubricant and designing the geometry and chemistry of the texture, enhanced condensation can be achieved (Figure 5-1e-f). We demonstrate that condensate droplets of water as small as 100 μm become mobile on such surfaces, continually sweeping them and creating fresh areas for further nucleation (Figure 5-1e-f). We capture the growth and shedding of the condensing droplets through direct imaging in an environmental scanning electron microscope (ESEM) as well as in a controlled-environment condensation apparatus. We also investigate the effect of surface texture and the interplay of the interfacial energies of the lubricant, textured surface, and droplets in order to facilitate design of such surfaces for enhanced condensation.

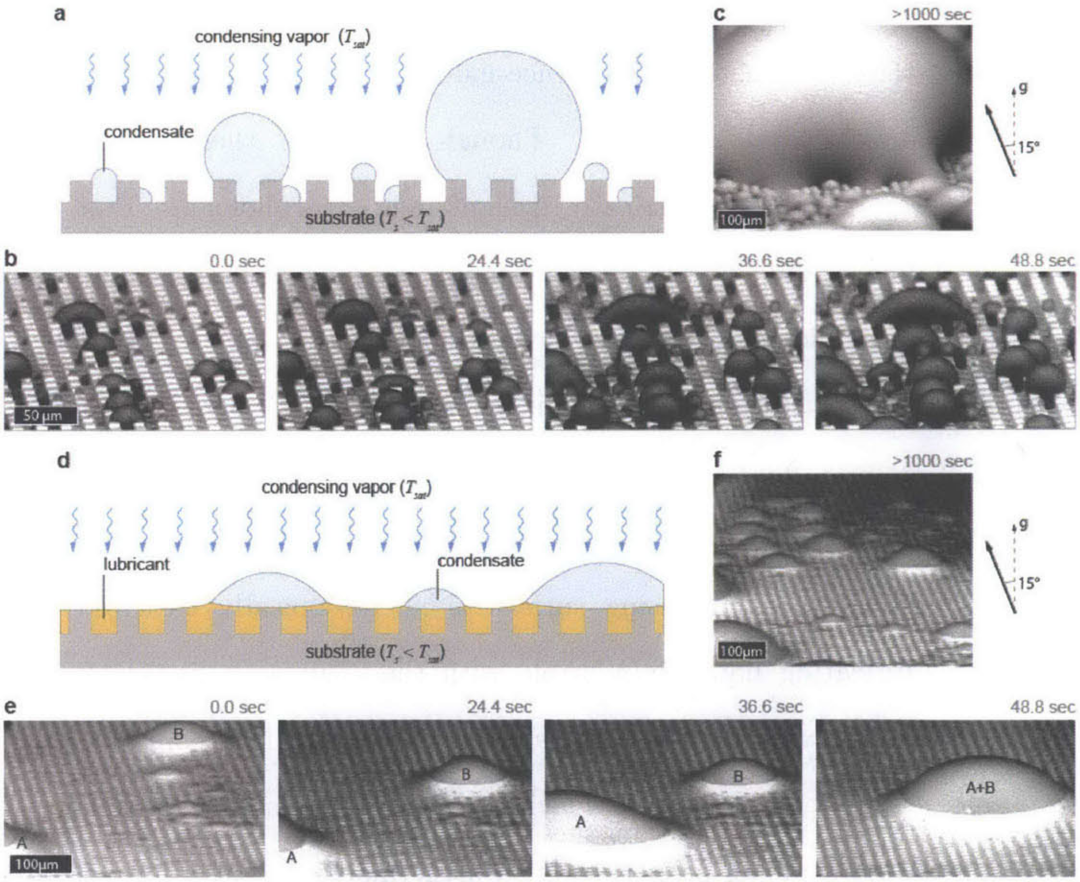

Figure 5-1. **Comparison of condensation of water vapor on superhydrophobic and lubricant-imbibed surfaces with identical texture**. (a) Schematic of condensation on a superhydrophobic surface showing the formation of droplets throughout the texture. (b) ESEM image sequence of condensation on a hierarchical superhydrophobic surface comprising nano-textured micropost arrays (see Figure 5-4e). Droplets

randomly nucleate on the top and within the texture features, grow and coalesce, and eventually (t >1000 sec) form (c) a large Wenzel droplet that is highly pinned. (d) Schematic of condensation on a lubricant-imbibed surface showing that droplets remain afloat on a lubricant film without impaling into the surface texture. (e) ESEM image sequence showing growth and motion of microscopic droplets on a nano-textured micropost array surface imbibed with ionic liquid. Drop B moves against gravity and coalesces with another randomly moving droplet A at 48.8 seconds, thereby clearing the surface for further nucleation. (f) ESEM image shows even after long time (>1000 s) small droplets remain mobile and clear the surface for further nucleation. The ESEM experiments were conducted under identical conditions (pressure = 1000 Pa, substrate temperature ~4.5°C, beam voltage = 25 kV and beam current = 1.7 nA; the surfaces were titled by 15° to the vertical).

We begin by describing the conditions necessary to imbibe a lubricating liquid into a textured surface and subsequently prevent its possible displacement out of the texture once condensate droplets start to form. Preventing lubricant displacement is important to avoid droplets from impaling the texture and becoming stuck.[62] For simplicity, we refer to the lubricant as oil and condensate droplets as water. It has been shown that an oil will imbibe a textured surface if $q_{os(v)} \le q_c$, where $q_{os(v)}$ is the contact angle of oil (subscript '*o*') on the smooth solid (subscript '*s*') in the presence of vapor (subscript '*v*'), and q_c is the critical contact angle for impregnation given by: $q_c = \cos^{-1}[(1 - f) / (r - f)]$.[62] Here, f is the fraction of the projected area of the textured surface that is occupied by solid and r is the ratio of total surface area of the textured surface to its projected area. For example, in the case of microposts, $f = a^2 / (a + b)^2$ and $r = 1 + 4ah / (a + b)^2$, where a is post width, b is edge-to-edge spacing between posts, and h is the post height. In the special case of $q_{os(v)} = 0$, the entire texture is covered with oil. When this condition is not met, portions of the texture are left uncovered above locations where the local contact angle of oil equals $q_{os(v)}$. Once water droplets begin to form on the textured surface, they can displace the oil from the texture unless $q_{os(w)} \le q_c$, where $q_{os(w)}$ is the contact angle of oil on the smooth solid in the presence of water (subscript 'w').[62,63] Again, if $q_{os(w)} = 0$, the entire texture underneath the water droplets would be covered with oil, whereas when this condition is not met, portions of the texture will remain uncovered and exposed to water. In addition to the above two conditions, a less obvious task in designing lubricant imbibed surfaces is to consider the possibility of cloaking (or encapsulation) of water droplets by the imbibed oil.[63] This can happen when the spreading coefficient of oil on water in the presence of vapor is positive, *i.e.*, $S_{ow(v)} > 0$, where $S_{ow(v)} = g_{wv} - g_{ov} - g_{ow}$, and g_{ij} is the interfacial tension between the phases i and j.[175,176] It is important to consider cloaking because it may prevent condensate growth, accelerate oil depletion from the texture, and contaminate the droplets. Conversely, the condensate may completely spread on oil if $S_{wo(v)} > 0$, where $S_{wo(v)} = g_{ov} - g_{wv} - g_{ow}$, leading to filmwise condensation. This scenario may occur during condensation of low-surface energy liquids such as refrigerants and organic liquids. Therefore, in order to avoid cloaking and promote dropwise condensation, $S_{ow(v)} < 0$ and $S_{wo(v)} < 0$.

5.1.1 Lubricant selection

Based on the above considerations, we chose two different lubricants for our study: a fluorinated oil (Krytox-1506, DuPont) and an ionic liquid (1-butyl-3-methylimidazolium bis(trifluoro-methyl-sulfonyl) imide, $[BMIm^+][Tf_2N^-]$) which we will refer to as BMIm for simplicity. Water was used as the condensing fluid. The condensing surfaces were well-defined cubical microposts of silicon (a = 10 µm, b = 10 µm, and h = 10 µm) fabricated by standard photolithography. A low energy silane (octadecyltrichlorosilane - OTS) was coated on the textured surfaces using solution-based deposition in order to render them hydrophobic (advancing water contact angle = 110° ± 4°) and preferentially wet by the lubricants (see Supporting Information for experimental details). Lubricants were imbibed into the textured surfaces by dipping them into a bath of lubricant and then withdrawing at controlled rates using a dip coater.[163] This procedure ensured high reproducibility and no excess impregnation of the lubricant. Two different types of experimental approaches were used to study the condensation phenomena: at the microscale, an ESEM was used at low supersaturation conditions to analyze the early stages of condensation, whereas at the macroscale, a controlled-environment condensation rig connected to a 20 kW boiler was used to examine droplet shedding and departure diameters. Contact angles of both lubricants on smooth OTS-coated silicon surfaces were measured in the presence of air as well as water. In addition, the interfacial tensions of lubricants in the presence of water were measured using the pendant drop method.[164] All of the above parameters, along with the relevant physical properties of the lubricants are listed in Table 5-1, from which several points are noteworthy. First, $S_{wo(v)} < 0$ for both lubricants, implying that water vapor would condense as droplets in both cases. Second, $S_{ow(v)} < 0$ for BMIm, but for Krytox, $S_{ow(v)} > 0$, indicating that Krytox would cloak the condensed water droplets, whereas cloaking would not be expected in the case of BMIm. Third, $q_{os(v)}$ is non-zero but less than q_c for both Krytox and BMIm indicating that the micropost tops will be left uncovered after impregnation. Fourth, since $q_{os(w)} < q_c$ for both Krytox and BMIm, water droplets are expected to remain suspended rather than impale into the texture. Finally, both lubricants have extremely low vapor pressure, especially BMIm, which mitigates the concern of lubricant loss through evaporation.

Table 5-1. Properties of Krytox and Ionic Liquid at room temperature.

Parameter	**Units**	**Krytox**	**BMIm**
g_{ov}[45]	mN / m	17	34
g_{ow} a)	mN / m	49	13
$S_{ow(v)}$ a)	mN / m	6	-5
$S_{wo(v)}$ a)	mN / m	-40	-63
$q_{os(v)}$	deg.	28 ± 4	64 ± 4
$q_{os(w)}$	deg.	28 ± 4	37 ± 4
q_c	deg.	65	65
Density[46]	kg / m^3	1860	1430
Dynamic viscosity[46]	Pa s	0.116	0.032
Vapor pressure	mmHg	$< 4 \text{ x } 10^{-7}$	$< 10^{-12}$

5.1.2 Spreading Coefficients of Krytox and Ionic Liquid

The equilibrium spreading coefficient, for Krytox and BMIm on water is given by $S_{ow(v)} = g_{ov} - g_{wv} - g_{ow}$ and the equilibrium spreading coefficient for water on the lubricant is given by $S_{wo(v)} = g_{ov} - g_{wv} - g_{ow}$. In these definitions, g_{ov}, g_{wv} and g_{wv} are the surface and interfacial tensions between phases at equilibrium, that is, after water and the lubricant become mutually saturated. These surface and interfacial tensions can be calculated from the profile of a pendant drop.[164] The details on spreading coefficient calculations are given below, and values of all the surfaces and interfacial tensions and the resulting spreading coefficients are provided in Table 5-2.

Table 5-2. Spreading coefficients of water-Krytox and water-[BMIm][Tf_2N] systems.

	g_{wv} (mN/m)	g_{ov} (mN/m)	g_{ow} (mN/m)	$S_{wo(v)}$ (mN/m)	$S_{ow(v)}$ (mN/m)
Krytox	72	17	49	-40	6
Ionic liquid	42	34	13	-66	-5

The ionic liquid used in the current study ([$BMIm^+$][Tf_2N^-]) is hydrophobic and considered to be almost completely immiscible with water.[165] However, it is slightly hygroscopic and has a very low solubility in water (~0.77% wt/wt).[166] The properties of BMIm upon saturation with water are available for surface tension (g_{ov}),[167] density[168] and viscosity.[168] In the absence of information on surface tension of water saturated with ionic liquid, we measured this value directly. Solutions comprising different concentrations of ionic liquid in water were prepared. Solutions were sonicated to completely dissolve the ionic liquid in water and a 5 μL drop taken from the resulting solution was used to calculate the interfacial tension (g_{wv}). The results of surface tension at different concentrations of ionic liquid in water are given in Figure 5-2. The saturated value of surface tension of water in presence of ionic liquid was found as 42 mN/m, calculated when ionic liquid/water weight% was ~1.0%. The spreading coefficients of water on BMIm (S_{wo}) and of BMIm on water (S_{ow}) are given in Table 5-2.

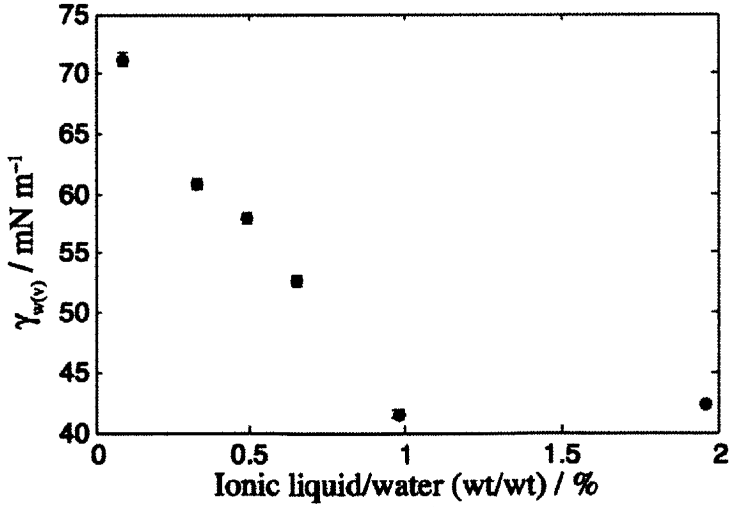

Figure 5-2. Surface tension of water with increasing concentration of ionic liquid. Decrease in surface tension of water due to partial miscibility of ionic liquid saturates at low values due to reaching critical micelle concentration.

We first analyze the effect of lubricant cloaking on the early stages of condensation using environmental scanning electron microscopy (ESEM) performed in a Zeiss EVO-55 and Zeiss EVO-LS10 equipped with a Peltier cooler. A custom copper fixture was fabricated to mount the samples and ensure adequate thermal contact with the Peltier device. All experiments were performed under identical conditions of pressure, electron beam parameters, beam scanning rate *etc.* The beam settings used were found to be best optimal settings for obtaining better imaging contrast of water droplets on the lubricants, especially Krytox. Videos from ESEM experiments were analyzed using ImageJ software.[49] Droplet growth analysis was performed using methods described elsewhere.[7] From the videos, the frames were extracted for analysis of droplet mobility that was performed using ImageJ. To obtain scaling for converting the pixel information into actual sizes, a reticule (10mm scale / 100 div) was photographed at the same focal distance as during the experiment. The change in droplet location (Δs) in time Δt was used to calculate droplet speed as $V = \Delta s / \Delta t$. This droplet speed is associated with a droplet of size $D_{avg} = (D_1 + D_2) / 2$ where D_1 and D_2 are diameter of droplet at time t and $t+\Delta t$ respectively. Since droplet coalescence is an extremely rapid process, performing such droplet mobility measurements over a longer period of time and having large sample space can provide a time-averaged value of mobility for a given droplet size. 1000 drops of different sizes were chosen randomly and analyzed for determining droplet mobility on lubricant-imbibed and un-imbibed nano-textured superhydrophobic surface (Figure 5-5c). The resolution of droplet displacement measurements was 10 μm. To obtain a representative value of mobility, droplet diameter was rounded to the nearest multiple of 100 μm, and a median for droplet speed of all the droplets with the same size was calculated.

The experiments were conducted at low subcoolings (substrate temperature,

T_s ~ 3.6°C, saturation temperature $T_{sat} = 3.8°\text{C}$ at $P = 800$ Pa) so that the condensation rate was not too high to be captured in ESEM (imaging rate 0.5 fps). These results are shown in Figure 5-3, which reveals that the droplet growth patterns obtained with the two lubricants are substantially different. On the Krytox imbibed surface (Figure 5-3a, $S_{ow(v)} > 0$), condensation is significantly inhibited as the droplets (black spots in the images) grow or coalesce little compared to those on the BMIm imbibed surface (Figure 5-3c, $S_{ow(v)} < 0$). Furthermore, droplets attain barrel shape (time $t = 111.9$ sec) on the BMIm imbibed surface as the dry hydrophobic post tops pin (Figure 5-3d) and confine droplets during the growth process. We calculated droplet coverage in each case by measuring the fraction of the total area of the images that was occupied by droplets. These results are given in Figure 5-3e, which clearly shows that the coverage of water droplets is both much faster and larger on the surface imbibed with BMIm compared to the one imbibed with Krytox. The suppression of droplet growth in the case of Krytox imbibed surface becomes more clear when we plot the number density of droplets with time and compare it with the BMIm imbibed surface. These measurements are shown in Figure 5-3f and reveal that the droplet number density first increases sharply due to nucleation and then decreases due to coalescence in the case of BMIm imbibed surface. Comparatively, the droplet number density on the Krytox imbibed surface increases weakly showing that droplet growth was significantly inhibited in this case. Furthermore, the condensed droplets on the Krytox imbibed surface could not be evaporated even under high superheat conditions (T_s - $T_{sat} = 20°\text{C}$). The above findings suggest that cloaking occurred during condensation on the Krytox imbibed surface (Figure 5-3b) and did not occur on the BMIm imbibed surface (Figure 5-3d), as predicted by their respective spreading coefficients (Table 5-1). It should be noted that cloaked droplets can grow through coalescence by draining the lubricant film between them,[46] which could be achieved through droplet confinement (*e.g.* within textures) while increasing their number density using higher supersaturation.

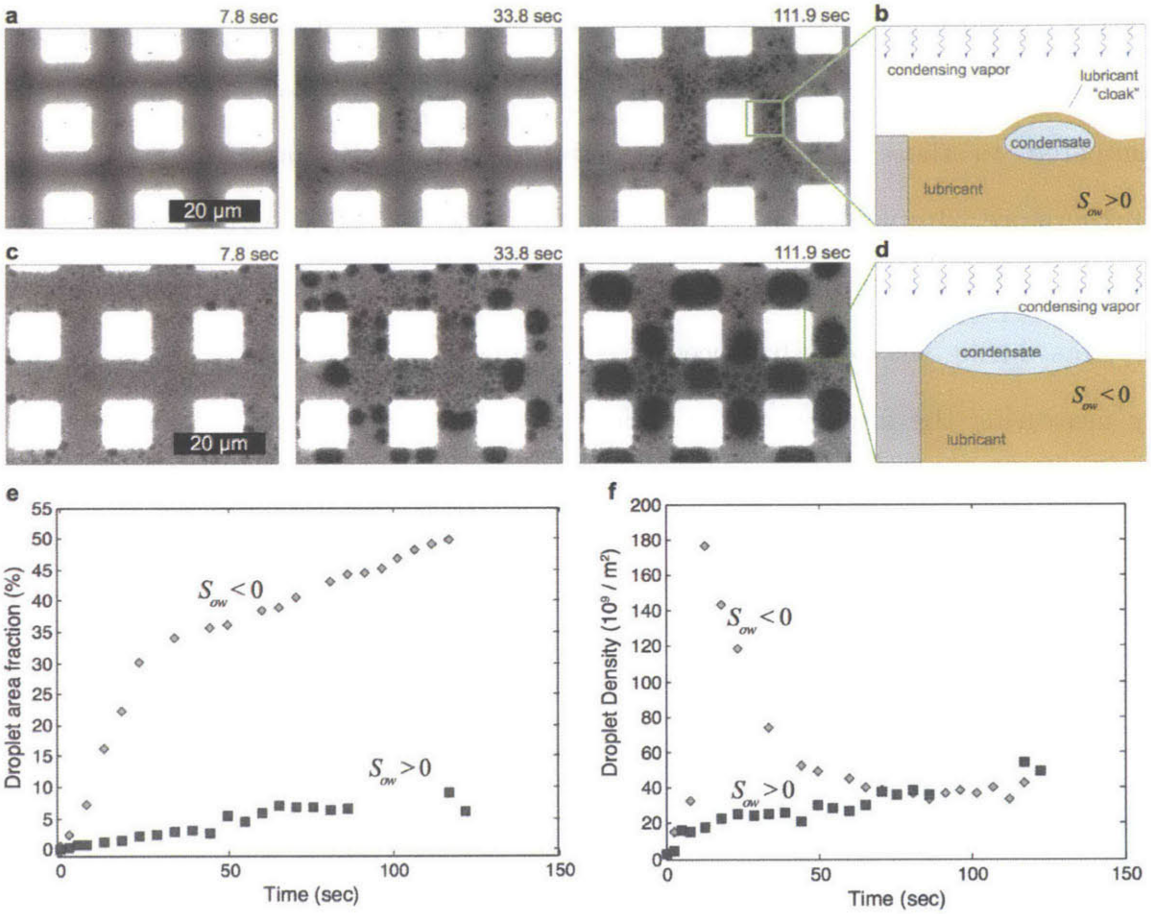

Figure 5-3. **Effects of lubricant spreading coefficient on condensate growth.** (a) ESEM image sequence of condensation on a micropost surface imbibed with Krytox that has positive spreading coefficient on water ($S_{ow} > 0$). Condensation is inhibited as Krytox cloaks the condensed droplets. (b) Illustration of cloaked condensate droplet depicting the thin film of condensate that spreads on the droplet. (c) ESEM image sequence of condensation on micropost surface imbibed with BMIm that has negative spreading coefficient with water ($S_{ow} < 0$). (d) Illustration of uncloaked condensate droplet depicting the three phase contact line of the water-vapor, water-lubricant, and lubricant-vapor interfaces on one end and pinning of the droplet at the dry post tops at the other end. (e) Plot comparing variation of surface area fraction covered by condensed water droplets versus time on surfaces imbibed with Krytox ($S_{ow} > 0$, solid squares) and BMIm ($S_{ow} < 0$, open diamonds). (f) Plot comparing number of water droplets per unit area versus time

on surfaces imbibed with Krytox (solid squares) and BMIm (open diamonds). The ESEM experiments were conducted under identical conditions (pressure = 800 Pa, substrate temperature ~ 3.6°C, beam voltage =25kV and beam current = 1.7 nA). In the analysis, t = 0 s is defined as the first frame in which water drops can be identified.

As shown in the frames showing microscopic growth, water droplets exist as micro-lenses on the surface of the ionic liquid during the growth process. This suggests that the change of surface tension of water occurs at times scales much smaller than condensation time scales. It should be noted that similar behavior has been noted with benzene and 1,1-diphenyl-ethane.[169] Camphor has also been observed to dissolve slightly in water, and this partial miscibility results in a decrease in the surface tension of water.[169]

Next, we analyze the effect of surface texture on the mobility of condensed droplets using ESEM. Figure 5-4a shows condensate drops (indicated by A-F) growing and coalescing on a micropost surface imbibed with BMIm. Although the drops grow, either by coalescence (droplets A and E, and B and C) or by direct condensation (droplets D and F), they remain largely immobile. This suggests that the drops were pinned to the texture probably at the post tops (Figure 5-4d), which is plausible since both $q_{os(v)}$ and $q_{os(w)}$ were non-zero in the case of BMIm. Also, the presence of a small drop of BMIm instead of a thin film on the post top (Figure 5-4c), along with the formation of barrel-shaped drops between the posts (Figure 5-2c), indicate that the post tops were uncovered by BMIm. To reduce pinning and enhance drop mobility we added a smaller level of roughness by etching nanograss on posts (Figure 5-4e) and imbibed it with BMIm. The additional capillary force imparted by the nanograss stabilizes BMIm even on post tops (Figure 5-4f), thereby reducing the uncovered solid where condensing drops could pin (Figure 5-4g). Consequently, when we condensed water vapor on this surface, we observed a dramatic increase in droplet mobility (Figure 5-1e): drops as small as 100 µm move rapidly across the surface.

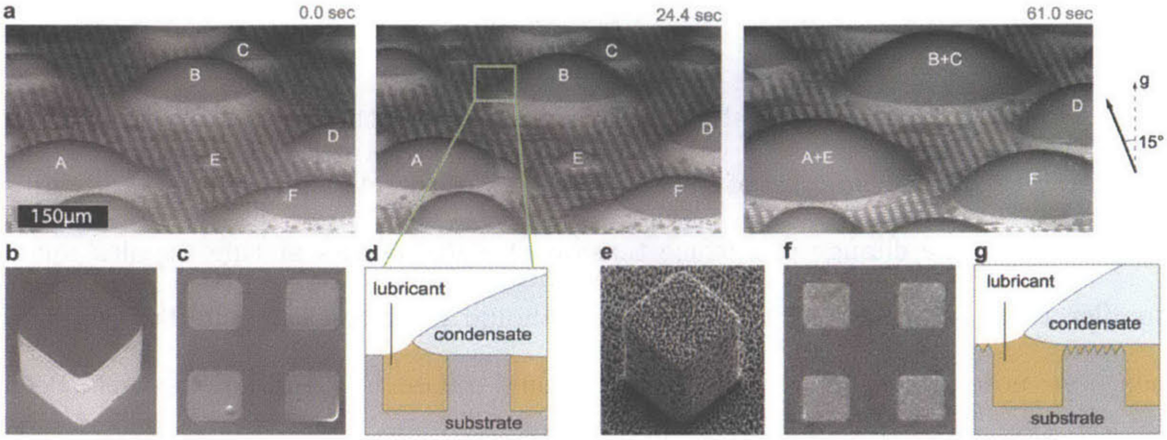

Figure 5-4. **Effects of pinned fraction on micropillars and nanograss.** (a) Image sequence showing growth of water droplets during condensation on micropost surface imbibed with BMIm. The images show that large droplets appear to grow and coalesce while still remaining at same location; there is no significant movement of drops. Also evident is the water-lubricant-vapor contact line that is pulled above the substrate. (b) SEM of a single smooth micropost. (c) Top-view SEM of smooth microposts imbibed with BMIm. A stable BMIm droplet can be seen on the surface indicating that the post tops are dry. (d) Schematic of a droplet on a textured surface that has been imbibed with a liquid for which $\vartheta_{os(w)} > 0$ depicting the exposed post tops beneath the water droplet and the pulled-up water-lubricant-vapor contact line. (e) SEM of a single micropost with etched nanograss structures. (f) SEM of imbibed surface with nano-textured microposts. (g) Schematic of a droplet on the nanograss micropost surfaces that has been imbibed with a lubricant. The nanograss allows for the lubricant to imbibe the post tops, resulting in reduced condensate-solid pinned fraction. The ESEM experiments were conducted under identical conditions (pressure = 1400 Pa, substrate temperature ~ 7.7°C, beam voltage =25kV and beam current = 1.7 nA).

Finally, we investigate the macroscopic behavior of condensed droplets on BMIm imbibed surface and compare it with a superhydrophobic surface having the same texture (microposts with nanograss) and chemistry (coated with OTS). These experiments were performed with saturated steam (60 kPa, 86°C) in the condensation rig of 2.1with a constant surface cooling flux (160 kW m^{-2}) and the condensing droplets were photographed using a digital video camera (Nikon D300s, 24 fps) equipped with a macro lens system (Nikon 105 mm with two 2X teleconverters) and a microscope lens (Navitar 6232). Sample surfaces were mounted to the face of a cylindrical copper cooling block instrumented with thermocouples to measure the cooling heat flux. The copper block was cooled by a water-cooled heat exchanger (NESLAB II, Thermo Scientific) and inserted into a vacuum chamber. After drawing vacuum of less than 100 Pa to remove non-condensable gas from the chamber, steam was introduced until the chamber reached a steady pressure of 60 kPa. Ultra-pure saturated steam was produced by an electric boiler (SR-20, Reimers Boiler Co.) supplied with 5 MΩ deionized water passed through a nanoporous membrane degassifier (Extra-Flow, Liqui-Cel) to obtain dissolved oxygen content of less than 1 ppm.

We find that under identical conditions, condensation occurs first on the imbibed surface and is delayed on the un-imbibed surface, indicating that the nucleation energy barrier is lower for imbibed surfaces, consistent with the trends reported on bulk liquids.[170] The results for droplet motion are shown in Figure 5-5. As seen in Figure 5-5a, droplets on the superhydrophobic surface were highly pinned, which was apparent by the non-spherical shape of the contact line of large droplets due to stretching by gravity. On the other hand, condensed droplets on the BMIm imbibed surface moved rapidly, which is shown in Figure 5-5b by drawing circles around some of the droplets to show their motion. While large droplets (˜ 1 mm) moved primarily in the direction of gravity, small ones (˜ 100 μm) moved in random directions creating a sweeping effect, as shown by circles and arrows in Figure 5-5b. To further characterize droplet mobility, we analyzed the motion of more than 1000 condensing droplets of various sizes on both the surfaces. We plot the speed of a representative droplet moving on the BMIm imbibed surface with time and compare it to that on the superhydrophobic surface. This is shown in Figure 5-5c, which shows that the droplet on the superhydrophobic surface remained mostly immobile except when it coalesced with a larger drop, resulting in a sudden increase in its speed (spikes in Figure 5-5c). On the other hand, the droplet on the BMIm imbibed surface was predominantly mobile with a speed that was several orders of magnitude higher than that on the superhydrophobic surface. Figure 5-5d assembles data of Figure 5-5c for a range of droplet sizes (from ~ 100 μm to gravity-induced departure) and plots their median speeds on the BMIm-imbibed and superhydrophobic surfaces. It can be seen that the median speed of droplets on the superhydrophobic surface remains negligible until the droplets grow sufficiently large to move by gravity (about 3.5 mm in diameter). In contrast, the median speed of droplets on the BMIm imbibed surface is much higher as early as when they are 100 μm in diameter. Moreover, the median speed remains consistently high and increases even further for higher droplet sizes until they begin to shed due to gravity. This data reveals a remarkable difference between the two surfaces: while droplets on the BMIm imbibed surface display gross continual motion, droplets on the superhydrophobic surface mostly "nudge" intermittently. The continual motion with high speeds on the BMIm imbibed surface is extremely beneficial as it induces a sweeping effect on the condensing surface and paves the way for nucleation of new drops. Since the condensation heat transfer is a strong function of droplet mobility,[171] we expect the BMIm imbibed surface to exhibit superior heat transfer performance.

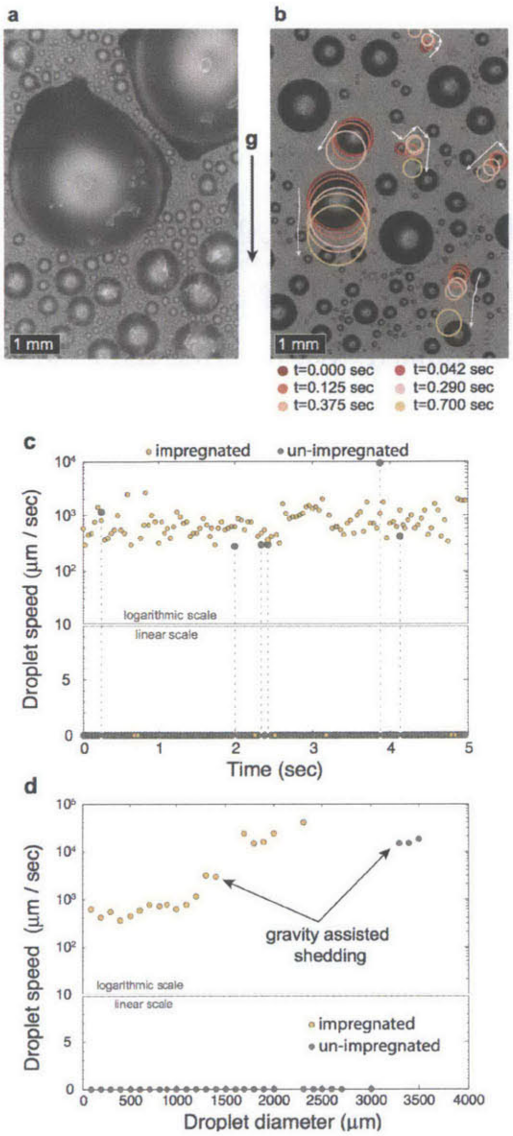

Figure 5-5. **Comparison of condensation on a hierarchical superhydrophobic and BMIm-imbibed surfaces with identical texture at macroscale.** (a) Representative image of condensation on superhydrophobic surface comprising nanograss microposts; large pinned droplets are seen before shedding from the surface. (b) Representative image of condensation on nanograss microposts imbibed with BMIm. Both small and large droplets are highly mobile; colored circles are provided as a guide to eye for depicting droplet motion. (c) speed of a representative droplet (initial diameter ~420 μm) as a function of time for un-imbibed (black circles) and imbibed surfaces (orange circles). (d) median speed of droplets as a function of drop diameter for un-imbibed (black circles) and imbibed surfaces (orange circles). The velocities of the immobile drops which moved by less than 1 pixel were below the measurement threshold of our apparatus, and therefore were assigned a value of zero The data are plotted on a mixed linear/logarithmic scale to capture both the zero value and substantial range of magnitudes in droplet speed.

In summary, we show that condensation of water droplets on lubricant-imbibed nanotextured surfaces occurs with enhanced droplet mobility compared to superhydrophobic surfaces. The enhancement results from the fact that the condensed droplets stay afloat on the lubricant with minimal pinning to the surface compared to superhydrophobic surfaces where droplets grow within textures and get strongly pinned. We describe the conditions required to ensure droplet floatation and demonstrate the effect of key parameters, such as texture geometry, surface energies of various phases, and lubricant cloaking on droplet growth and mobility. The extremely high mobility and the resultant sweeping effect of condensed drops observed on lubricant imbibed surfaces makes them promising for enhanced condensation heat transfer. We identify several phenomena, such as lubricant cloaking and pinning reduction using partially-wet nanotextures, that are expected to have broad implications for other applications of these surfaces such as anti-icing, self-cleaning, and anti-fouling.

5.2 Low-sigma condensation

Here, we investigate the condensation of a variety of liquids with low surface tensions (12 to 28 mN/m) on lubricant-imbibed surfaces and compare the behavior to smooth oleophobic and textured superomniphobic surfaces. Specifically, we used a custom built condensing chamber to study condensation of perfluorohexane, pentane, hexane, octane, isopropanol, ethanol, toluene, and, as a reference, water. The surfaces tested in the present study include both smooth and textured silicon wafers functionalized with fluorosilane coatings. The textured samples were vapor-deposited alumina-silica nanotextures[172] (Figure 5-6a), spray-coated re-entrant structures[173] (Figure 5-6b), and microposts (Figure 5-6c). Wettability and condensation of all the textured surfaces was studied before and after imbibition with Krytox perfluorinated oil (Krytox-1506 from DuPont, Figure 5-6d, e, f). This lubricant was selected primarily because its surface tension (γ_{lv} = 17 mN/m) is low enough to promote dropwise condensation of most condensed fluids while avoiding cloaking,[58,63] and also because of its low vapor pressure, broad chemical inertness, and immiscibility with most of the condensed fluids.

Advancing and receding contact angles and hysteresis of the condensing liquids on the smooth oleophobic, nanotextured, and Krytox-imbibed nanotextured surfaces were measured using the pendant drop method. On the nanotexture, although the advancing contact angle of water was greater than 160° with a contact angle hysteresis less than 5°, we found that all low-surface tension liquids spread over the texture. On the superomniphobic surface, ethanol wet in a Cassie-Baxter state with an advancing angle of 147 ± 3°,[173] and the *n*-alkanes wet in the Wenzel state with an advancing contact angle of ~50°. Since the surface is 50% PMMA, it was incompatible with toluene and isopropanol. Perfluorohexane spread completely on all surfaces due to its low surface tension, and since it is almost completely miscible with Krytox, also spread on all lubricant-imbibed surfaces. The contact angles of the non-spreading liquids on the smooth oleophobic surface and Krytox-imbibed nanotexture are shown in **Textured surfaces before and after lubricant impregnation.** (a) vapor-deposited alumina-silica nanotexture. (b) re-entrant superomniphobic texture. (c)

Silicon microposts etched via photolithography. (d) Krytox-imbibed nanotexture. (e) Krytox-imbibed superomniphobic texture. (f) Krytox-imbibed microposts.

Table 5-3.

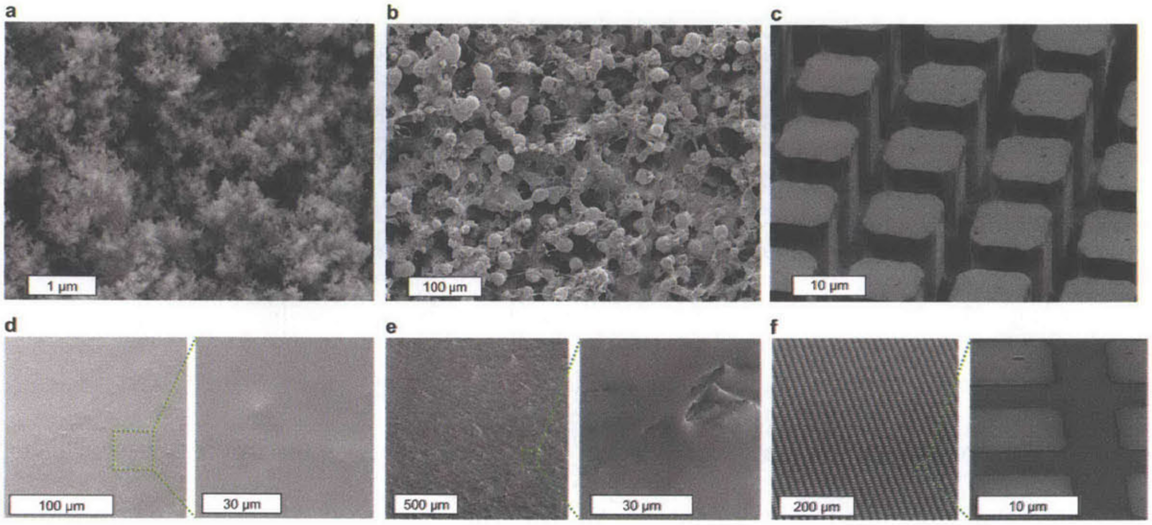

Figure 5-6. **Textured surfaces before and after lubricant impregnation.** (a) vapor-deposited alumina-silica nanotexture. (b) re-entrant superomniphobic texture. (c) Silicon microposts etched via photolithography. (d) Krytox-imbibed nanotexture. (e) Krytox-imbibed superomniphobic texture. (f) Krytox-imbibed microposts.

Table 5-3. Surface tension, σ_{lv}, advancing contact angle, ϑ_a, receding contact angle, ϑ_r, and contact angle hysteresis, $\Delta\vartheta$, of non-spreading condensing liquids measured on smooth oleophobic surface and Krytox-imbibed nanotexture.

		smooth oleophobic surface (γ_c = 10.1 mN/m)			**Krytox-imbibed nanotexture** (γ_{lv} = 17 mN/m)		
liquid	σ_{lv} (25°C) [mN/m]	θ_a [deg]	θ_r [deg]	$\Delta\theta$ [deg]	θ_a [deg]	θ_r [deg]	$\Delta\theta$ [deg]
water	72.7	119.5 ± 2.1	60.3 ± 1.7	59.3 ± 3.2	118.8 ± 1.0	116.8 ± 0.5	2.0 ± 0.8
toluene	27.9	75.3 ± 1.2	45.0 ± 1.7	30.3 ± 1.5	66.0 ± 1.0	35.3 ± 2.5	30.7 ± 3.1
ethanol	24.8	66.5 ± 0.6	37.3 ± 1.9	29.3 ± 2.2	57.8 ± 4.0	0.0	57.8 ± 4.0
isopropanol	20.9	58.3 ± 2.5	35.5 ± 2.4	22.8 ± 1.7	41.3 ± 2.6	0.0	41.3 ± 2.6
pentane	15.1	50.3 ± 0.5	9.3 ± 1.7	41.0 ± 2.2	35.3 ± 0.5	5.2 ± 2.1	20.1 ± 1.5
hexane	18.0	57.3 ± 2.5	30.7 ± 1.2	26.7 ± 1.5	44.0 ± 1.0	11.3 ± 3.5	32.7 ± 4.0
octane	21.1	66.7 ± 0.6	34.7 ± 0.6	24.0 ± 1.0	55.3 ± 0.6	43.0 ± 3.6	12.3 ± 3.8
perfluoro-hexane	12.0	0.0	0.0	0.0	0.0	0.0	0.0

5.2.1 Condensation behavior

Next, we investigated condensation behavior of all fluids on four surfaces: smooth oleophobic wafer, dry superomniphobic texture, and the Krytox-imbibed and unimbibed nanotexture. On the flat oleophobic surface, we observed continual formation and shedding of drops of all fluids with exception of perfluorohexane (Figure 5-8a). For the fluids with which the superomniphobic texture was compatible, namely water, ethanol, and the *n*-alkanes, the surface exhibited filmwise condensation. On the unimbibed nanotexture, although condensation of water led to self-propelled jumping droplet motion, all of the low-surface tension fluids flooded the surface (Figure 5-8b). Finally, on the Krytox-imbibed nanotexture, condensation of water, toluene, pentane, octane, and hexane led to continual formation and shedding of drops (Figure 5-8c) whereas condensation of perfluorohexane, ethanol, and isopropanol, led to filmwise condensation.

Visualization of the condensation behavior of different fluids was performed inside a condensation chamber (Figure 5-7). After mounting of the sample using double-sided copper tape on the aluminum back-plate, the bottom of the chamber was filled with 25 mL to 100 mL of the liquid. Perfluorohexane (99%, Sigma-Aldrich), pentane (99%, Sigma-Aldrich), *n*-hexane (95%, J. T. Baker), isopropanol (99.99%, Fisher), ethanol (99.5%, Sigma-Aldrich), *n*-octane (99%, anhydrous, Sigma-Aldrich), toluene, (99.8%, Sigma-Aldrich) and deionized water were used as working fluids. The pressure within the chamber was reduced using house vacuum down to about 50 kPa. After pumping down for about 30 s to 60 s, the vacuum valve was closed and temperature of the sample was reduced using a water-cooled Peltier element mounted to the outer side of the back-plate.

Temperatures were monitored using a K-type thermocouple placed in a recess drilled into the back-plate. To minimize the thermal contact resistance, silicon thermal grease (Dow-Corning) was applied between the Peltier element and the aluminum back-plate. The sample was illuminated using a ring light (Nikon) and imaged using a CMOS camera (ImagingSource) with a 10x objective lens. Images of the condensation process were captured for a period of 30 to 90 minutes with frequency of 5 Hz to 0.2 Hz, dependent on the rate of condensation of particular fluid. The images were manually analyzed using FIJI image analysis software. All reported diameter values are averages of six measurements with associated standard errors reported with a coverage factor of one. To ensure that residual water vapor in the chamber did not affect the condensation process, a control experiment was carried out by evacuating the chamber without a liquid and reducing the temperature of the back-plate to -5ºC. No condensation or frost formation was observed on the back-plate and mounted silicon wafer after 30 minutes of cooling, indicating a negligible amount of residual moisture in the chamber.

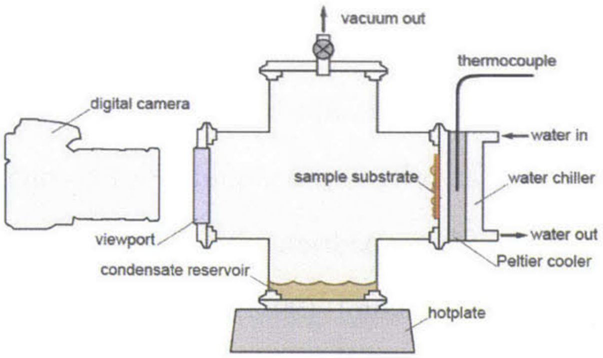

Figure 5-7. **Schematic of condensation chamber**. The bottom of the chamber was filled with a small amount of working fluid and evacuated. A Peltier cooler at the rear of the device provided cooling flux and temperatures were measured with a K-type thermocouple.

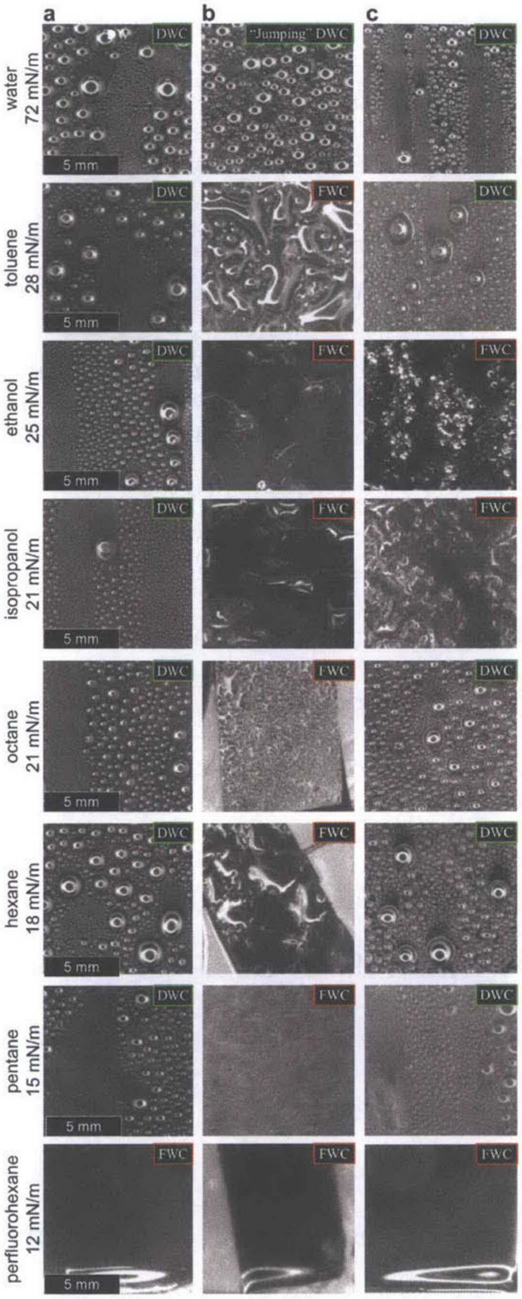

Figure 5-8. **Effect of condensate interfacial tension on condensation mode on different surfaces.** Condensation of various low-surface tension fluids on a (a) flat oleophobic surface, (b) unimbibed nanotexture, and (c) Krytox-imbibed nanotexture. DWC and FWC stand for dropwise and filmwise condensation, respectively.

The continual shedding of drops of all liquids (with exception of perfluorohexane) from the smooth oleophobic surface can be explained by its combination of moderately high contact angle and low contact angle hysteresis.[40]

However, since the advancing contact angles of all of low-surface tension fluids on the silanized solid was significantly below 90º (see Table 5-3), the addition of any surface roughness should amplify the wetting properties of the surface according to Wenzel's equation:[157,174]

$$\cos\theta_w = r\cos\theta_e \qquad \text{Equation 5-1}$$

where θ_w and θ_e are the Wenzel and Young equilibrium contact angles, respectively, and r is the Wenzel roughness: the ratio of the actual and projected areas. Hence, flooding of a textured silanized surface would be expected whenever condensing a low-surface tension fluid with an equilibrium contact angle less than 90°. However, such wettability arguments cannot be used to explain condensation behavior on the re-entrant superomniphobic surfaces. These surfaces have been shown to repel macroscale drops of ethanol and other low surface tension liquids due to their re-entrant geometrical features, where the wetting state is described by a modified Cassie-Baxter equation.[52,173] During condensation, since nuclei of condensing liquids have critical diameters of only a few nanometers,[25] they can easily nucleate within the roughness features of the re-entrant texture, similar to what was shown previously for water.[54,55,14,56,15,57] This behavior prevents formation of the Cassie-Baxter wetting state necessary for omniphobicity[51] and leads to the flooding observed on the spray-coated superomniphobic surface during condensation.

Impregnation of the textured surfaces with the perfluorinated oil dramatically alters macroscale wetting and condensation behavior of all the fluids and highlights the importance of the surface morphology. The wetting states for all of the condensing liquids on the Krytox-imbibed nanotexture, except for perfluorohexane since it is miscible with Krytox, are calculated from Equation 5-2 and depicted in Figure 5-9a, b, c. It has been shown that if the spreading coefficient ($S_{ls(c)}$) of the lubricant (subscript l) on the solid (subscript s) in the presence of condensate (subscript c) is greater than zero, i.e. $S_{ls(c)} > 0$, then the condensate drops will float on a thin film of lubricant with virtually no pinning (Figure 5-9c).[63] If $S_{ls(c)} < 0$, then in order to prevent the condensate from displacing the lubricant (Figure 5-9a), the surface lubricant and solid must possess surface energies in relation to the surface roughness such that

$$-\left(\frac{r-1}{r-\phi}\right) < \frac{S_{ls(v)}}{\gamma_{lc}} < 0 \qquad \text{Equation 5-2}$$

where r is the ratio of the actual surface area to the projected surface area and ϕ is the solid/condensate fraction.[63]

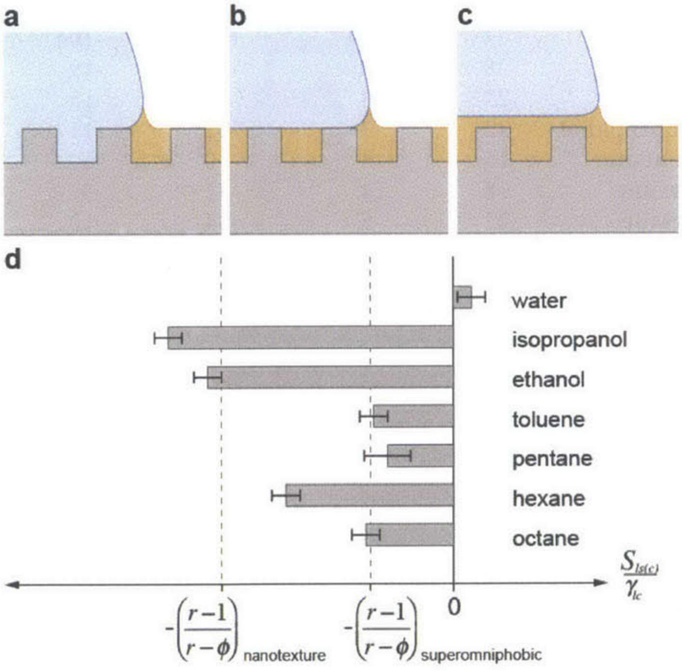

Figure 5-9. **Wetting states of condensing fluids on Krytox-imbibed surfaces.** The x-axis shows the spreading ratio of the lubricant on the solid in the presence of condensate. Dotted vertical lines correspond to roughness ratios on nanotexture and superomniphobic texture.

We observed that isopropanol and ethanol exhibited filmwise condensation. These liquids have a higher liquid/vapor interfacial tension than pentane and hexane, thus it was surprising to see that they display filmwise behavior while pentane and hexane displayed robust dropwise shedding behavior. This behavior can be explained by noting that the spreading coefficient of Krytox in the presence of isopropanol and ethanol is much lower than with pentane or hexane (Figure 5-9d), so the former two liquids act to destabilize the lubricant film and impale the solid texture. These experiments highlight the importance of the spreading coefficients of the lubricant on the solid surface not only in the presence of vapor but also in the presence of the condensate.

Table 5-4. Condensate/lubricant interfacial tensions and spreading coefficients.

	σ_{cv} [mN/m]	σ_{lc} [mN/m]	$S_{lc(v)}$ [mN/m]	$S_{cl(v)}$ [mN/m]
water	72	49	6	-104
toluene	28	8	-38	-19
ethanol	23	8	-32	-15
isopropanol	22	7	-32	-11
pentane	16	3	-30	-1
hexane	18	4	-32	-5
octane	22	5	-34	-10

The average base diameters of shedding drops were measured (see Table 5-5) to further investigate the effects of wetting state on condensation behavior. We observe a difference in shedding diameter of the different liquids on the same surface, which do not follow the same trend as the departure diameters on the smooth oleophobic surface. We attribute this behavior to the difference in wetting state of the lubricant film beneath the condensate drops. The small departing diameters of toluene (1.3 ± 0.2 mm) and pentane (1.2 ± 0.1 mm) compared to hexane (2.4 ± 0.1 mm) and octane (2.2 ± 0.2 mm) can be explained by their larger spreading ratio. Since the spreading coefficient of Krytox in the presence of toluene and pentane is larger than with hexane and octane, the former two liquids tend to stabilize the lubricant film underneath condensate drops, leading to reduced pinning and thus smaller departing diameters.

Table 5-5. Base diameters of condensing drops shedding from flat oleophobic surface and Krytox-imbibed nanotexture measured at 10-minute intervals.

	smooth oleophobic surface	Krytox-imbibed nanotexture		
liquid	d_{base} [mm]	d_{base}(0 min) [mm]	d_{base}(10 min) [mm]	d_{base}(20 min) [mm]
water	2.2±0.2	1.0±0.1	1.0±0.1	1.0±0.1
toluene	2.7±0.6	0.8±0.1	1.3±0.2	1.5±0.1
ethanol	2.0±0.1	filmwise	filmwise	filmwise
isopropanol	1.9±0.2	filmwise	filmwise	filmwise
pentane	1.5±0.1	0.8±0.1	1.2±0.1	1.5±0.2
hexane	2.5±0.1	2.3±0.2	2.4±0.1[a]	2.8±0.2[a]
octane	1.8±0.3	2.1±0.2	2.2±0.2	2.3±0.2

[a] measured at 7.5 min and 15 min

Average drop departure diameters from the imbibed nanotexture measurably increased over time, and are given in Table 5-5 at the initial moments of dropwise condensation, after 10 minutes, and after 20 minutes. On the smooth oleophobic surface, we did not observe any change in condensation behavior over time. On the imbibed nanotexture, on the other hand, we observed that drop circularity decreased while departure size increased during condensation. We attribute this increase in shedding diameter over time to a gradual depletion of the lubricant film when the texture becomes exposed and thereby pins the drops.[63] To determine the effects of excess lubricant during condensation, we performed an additional condensation experiment in which the excess lubricant layer was not removed with a nitrogen jet. The sequence of images in Figure 5-10a shows that condensation of pentane on this surface led to rapid emulsification of the lubricant. Most of the excess lubricant was removed by the shedding of this emulsion-like heterogeneous mixture of pentane and Krytox drops during the first ~140 sec of condensation. Subsequent pentane condensation behavior resembled that observed on the imbibed nanotexture without the excess lubricant layer (Figure 5-8c). Thus, the presence of the excess lubricant layer is not beneficial for condensation and is quickly removed during the process.

To further elucidate the interplay of texture on the stability of the lubricant film, we investigated the condensation of pentane on the imbibed superomniphobic and micropost textures (Figure 5-10b, c). We observed that the behavior of pentane condensation on these surfaces was strongly influenced by the underlying solid texture. As with condensation on the imbibed nanotexture, the imbibed superomniphobic texture exhibited sustained shedding of drops (Figure 5-10b). We also observed that the pinning of shedding droplets increased over time on the imbibed superomniphobic texture. The drops shown in Figure 5-10a and b illustrate that this effect was much more pronounced on the superomniphobic texture.

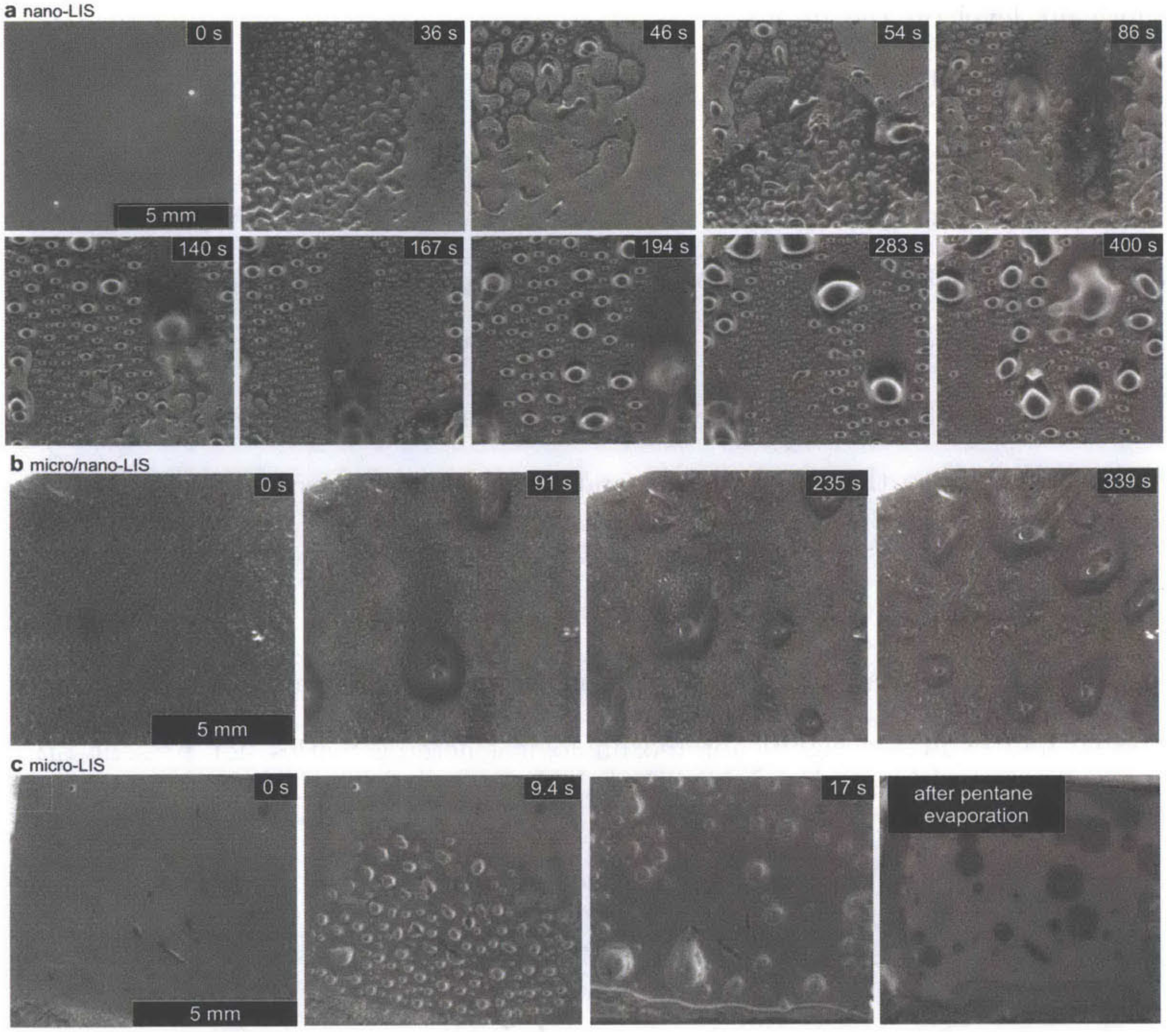

Figure 5-10. **Effect of texture of lubricant-imbibed surfaces on condensation.** (a) Condensation on Krytox-imbibed nanotexture with excess lubricant, clearing off by ~140sec. (b) Krytox-imbibed superomniphobic texture with highly-pinned drops. (c) Imbibed microposts are displaced by condensing pentane.

The increased pinning to the imbibed superomniphobic texture can be explained by the larger exposed area fraction of the roughness features. The SEM images in Figure 5-6d and e show topology of the imbibed nanotexture and superomniphobic texture after about 10 minutes of pentane condensation. The high area fraction of microscale topological features protruding above the lubricant level on the imbibed re-entrant texture explains the higher degree of drop pinning observed on this surface as compared to the relatively smooth imbibed nanotexture.[58,63]

On the imbibed microposts, the behavior was starkly different from the other two imbibed textures. Only a small number drops formed and either remained stationary or shed and aggregated at the bottom of the sample (Figure 5-10c). We also find during these experiments that contact between drops did not necessarily lead to their coalescence, and that in some cases secondary drops on top of primary drops were present.[58] After 30 sec, further cooling of the surface did not result in formation of any additional drops. We observed that after evaporation of pentane, triggered by raising the cooling plate temperature, the sample had exhibited significant morphological heterogeneities not present prior to condensation.

We attribute the unusual behavior on the imbibed microposts to the displacement of the lubricant by the condensate as predicted by Equation 5-2. Since the roughness of the micropillars is much lower than that of either the imbibed nanotexture or superomniphobic texture, the critical spreading ratio that leads to impalement is not as low for this surface. As indicated by Figure 5-9, all liquids except water have a spreading ratio that is sufficiently low to cause impalement of the microposts by the condensate. This hypothesis is further supported by observation of the morphology of the surface after pentane evaporation. Figure 5-9 shows that the heterogeneities after condensation correspond to regions in which oil was displaced from the surface. Additionally, the image sequences in Figure 5-10c shows that the Krytox, which accumulated at the bottom of the sample after dewetting, slowly wicks back in-between the micro-pillars leading to self-healing of the lubricant-imbibed surface.

5.2.2 Heat transfer coefficient

To determine the enhancement of dropwise over filmwise condensation modes, we measured the heat transfer coefficients for ethanol, pentane, and hexane on flat hydrophilic and flat oleophobic surfaces. The corresponding values for dropwise condensation were also estimated theoretically by substituting the experimentally measured droplet departure diameters and average contact angles into Kim and Kim's model. For filmwise condensation an equivalent heat transfer coefficient was estimated using a linear fit to the Nusselt model over ΔT range of 0 K to 10 K. The plot in Figure 5-11 shows close agreement between the measured and calculated values. This plot also demonstrates a four to eight-fold enhancement in heat transfer coefficient for dropwise vs. filmwise condensation for the three fluids. We also used the two models to predict the heat transfer coefficient enhancement for the remaining fluids on both smooth oleophobic surfaces and Krytox-imbibed nanotexture. The plot in Figure 5-11 shows that for all fluids the predicted heat transfer coefficient enhancement on smooth oleophobic surfaces was in the four to eight-fold range, but was smaller, in the two to six-fold range, for the Krytox-imbibed nanotexture. The difference in the enhancement value on these two types surfaces stems from the thermal resistance introduced by the lubricant layer.

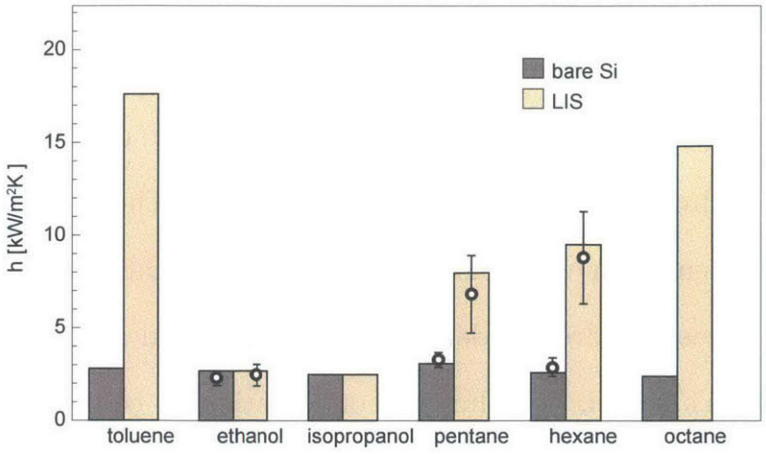

Figure 5-11. **Measured and predicted enhancement of heat transfer coefficients**. The predicted filmwise HTC was calculated from linear fit to Nusselt model and the predicted dropwise HTC on smooth oleophobic surface and Krytox-imbibed nanotexture was calculated using Equation 1-2 with experimentally determined departing diameters from Table 5-5. Experimental measurements are indicated with points.

Heat transfer coefficients were measured by introducing vapor to a chilled sample surface with diameter 50mm held in an evacuated chamber. The back side of the sample was chilled by forced cooled water. A vial of condensate liquid was immersed in a circulating water bath held at 35-40°C depending on the vapor pressure of the condensate. A vacuum vent was held near the point of heat transfer measurement to exhaust any non-condensable gases that may have accumulated in the chamber. Exhaust rates were less than 1 sccm and did not noticeably perturb condensation behavior. Sample temperatures were measured by 2252 kOhm thermistors (T337, Redfish Sensors) embedded 25 mm into a metal block behind the sample surface at precisely known locations. The thermistors were calibrated to ± 0.01°C using a platinum resistance probe (T100, Isotech) immersed in a circulating bath (FP-25, Julabo) filled with 50/50 water/ethylene glycol held to ± 0.01°C. The measurements of dT/dx, along with the thermal conductivity of the block, were used to determine the surface temperature. Saturated vapor temperature was determined from an Arrhenius correlation fitted to the range of 5-20°C, with residuals less than 0.01°C. Saturation pressure was measured by a high-accuracy pressure transducer (PX01 Omega) calibrated to ± 0.15% reading against a precision manometer (629B, MKS Instruments). Subcooling temperatures were thereby measured to accuracies better than 0.08°C. Measurements were taken after the apparatus had been allowed to reach steady state for 30 min.

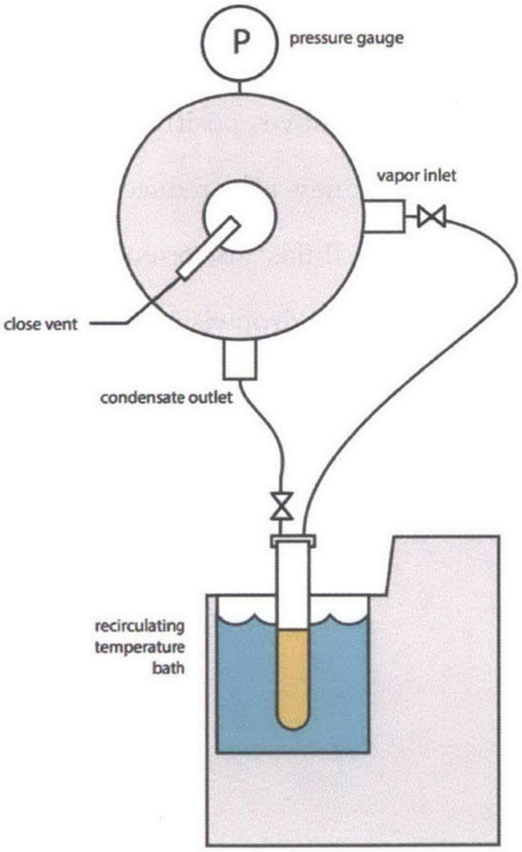

Figure 5-12. **Vapor condensation heat transfer measurements.** A sealed vial of vapor was immersed in a recirculating temperature bath and introduced into a vacuum chamber through a needle valve. The test surface in the vacuum chamber was cooled by forced chilled water and the resulting condensate drained back into the vapor vial.

In summary, we studied the condensation modes of fluids with surface tension in the range of 12 - 30 mN/m on oleophobic, superomniphobic, and lubricant-imbibed surfaces. We demonstrated that smooth oleophobic and stable lubricant-imbibed surfaces promote continual droplet formation and shedding of a majority of the studied fluids, whereas unimbibed superomniphobic textures become flooded due to nucleation within their re-entrant texture. By promoting dropwise condensation, we anticipate the increase in heat transfer coefficient to be at least two to four fold vs. filmwise condensation. Further increases in heat transfer coefficients on lubricant-imbibed surfaces could be realized by using higher thermal conductivity lubricant, minimizing the solid pinned fraction or using a lubricant-solid pair that have positive spreading coefficient in the presence of the condensate, which may also reduce lubricant drainage. Although the results for most of the studied fluids are promising, this study demonstrates the significant difficulty in promoting dropwise condensation of ultra-low-surface tension liquids, specifically fluorocarbon liquids. Future work should be directed toward the development of durable ultra-low-surface energy modifiers, and also to lubricants that are not non-wetting to fluorinated liquids.

6 Conclusions

6.1 Review of heat transfer coefficient

It is important when analyzing the performance of a particular component of a larger to take into consideration the system as a whole. In this case, it is helpful to start with an analysis of the overall heat transfer coefficient of a surface condenser. We will consider the case of shell-and-tube configuration since this type of condenser is used most commonly in power plants.[68]

The heat transfer through a condenser may be simplified into three dominant resistances. Although there are other sources of thermal resistance, such as non-condensable vapor and tube fouling, we will consider here the idealized case where the overall heat transfer coefficient is determined by three individual heat transfer resistances, shown below in Figure 5-2.

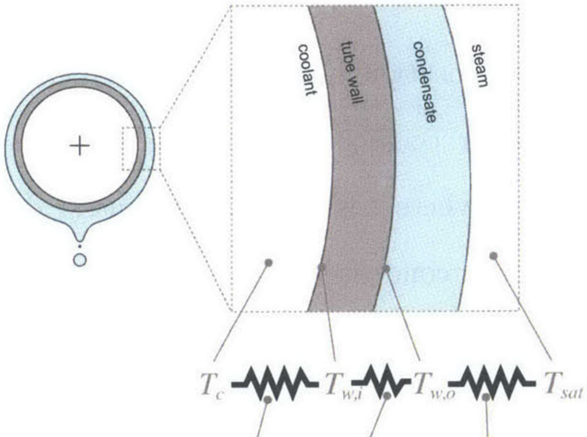

[kW/m²K]	h_i	h_w	h_o
filmwise	9.7	19.9	10.2
dropwise	9.7	19.9	38.5

Figure 6-1. **Thermal resistances in condenser tube.** The thermal resistances of a condenser tube are dominated by three principal resistors, or inverse heat transfer coefficients: convection from coolant water to the inside of the tube h_i, conduction through the tube h_w, and condensation on the outside of the tube h_o

which in filmwise mode is dominated by convection through the condensate film.

First, heat is transferred from saturated steam to the surface of the tube. In the case of filmwise condensation, which we will use as a point of comparison, all thermal processes may be lumped into a single heat transfer coefficient, given below by the Nusselt correlation:[175]

$$\mathrm{N\bar{u}}_D = 0.728\left[\frac{\rho_f(\rho_f-\rho_g)g_e h'_{fg} D^3}{\mu k(T_{sat}-T_w)}\right]^{1/4} \qquad \text{Equation 6-1}$$

Were h_{fg}' is the modified enthalpy of boiling. Evaluating at the conditions of a typical power plant condenser given in Table 2-1:

Table 6-1. Operating conditions of a typical power condenser.[68]

Parameter	**Value**	**Units**
P	3.98 kPa	condenser pressure
q''	30.68 kW/m^2	heat flux
T_s	28.89 °C	steam temperature
$T_{c,in}$	15.5°C	coolant inlet temperature
$T_{c,out}$	20.1°C	coolant outlet temperature
d_o	25.4 mm	tube outer diameter
d_i	24.0mm	tube inner diameter
k_w	16 W/mK	tube thermal conductivity

the resulting filmwise condensation heat transfer coefficient is 10.23 kW/m^{2}K. The equivalent heat transfer coefficient of the very thin tube wall h_w may be approximated as $h_w = k_w/t$ where t is the wall thickness: d_o-d_i / 2. Evaluated at the conditions of the model condenser, the equivalent heat transfer coefficient through the tube wall is 19.98 kW/m^{2}K. Finally, the convection heat transfer coefficient may be evaluated using the Gnielinski correlation:

$$\mathrm{N\bar{u}}_D = \frac{(f/8)(\mathrm{Re}_d-1000)\mathrm{Pr}^{2/3}}{1+12.7\sqrt{f/8}\left(\mathrm{Pr}^{2/3}-1\right)} \qquad \text{Equation 6-2}$$

where f is the friction factor, given by $f = (0.79\ \ln(\mathrm{Re}_D)-1.64)^{-2}$. Evaluating at the conditions of a model condenser, we arrive at a convection heat transfer coefficient of 9.74 kW/m^{2}K. Notably, all three heat transfer coefficients are of the same order of magnitude. Owing to the presence of the other two heat transfer coefficients – conduction through the tube wall and convection inside the tube – increasing the steam-side heat transfer coefficient will only have a limited effect on increasing the overall heat transfer coefficient as the other two resistances become dominant:

$$U = \left(\frac{1}{h_i} + \frac{1}{h_w} + \frac{1}{h_o} \right)^{-1} \qquad \text{Equation 6-3}$$

We now estimate the effect of increasing the heat transfer coefficient on the efficiency of the entire steam cycle. We first define the overall heat transfer coefficient as a function of the three individual heat transfer coefficients due to internal convection, conduction through the wall, and condensation of steam given by Equation 6-3. Next, we hold the thermal duty of the plant constant to relate the log-mean temperature difference (LMTD) across the condenser:

$$\begin{aligned} &\dot{Q} = \dot{m} h_{fg} = U \cdot A \cdot \mathrm{LMTD} \\ &U_{film} \cdot A \cdot \mathrm{LMTD}_{film} = U_{drop} \cdot A \cdot \mathrm{LMTD}_{drop} \\ &\Rightarrow \mathrm{LMTD}_{drop} = \mathrm{LMTD}_{film} \frac{U_{film}}{U_{drop}} \end{aligned} \qquad \text{Equation 6-4}$$

Using the definition of the LMTD, we can solve for the saturated temperature of the steam in the augmented condenser:

$$\mathrm{LMTD} = \frac{\left(T_{c,out} - T_{c,in}\right)}{\ln\left(\dfrac{T_s - T_{c,in}}{T_s - T_{c,out}} \right)} \Rightarrow T_{s,drop} = \frac{T_{c,in} - T_{c,out} \exp\left(\dfrac{T_{c,out} - T_{c,in}}{\mathrm{LMTD}_{drop}} \right)}{1 - \exp\left(\dfrac{T_{c,out} - T_{c,in}}{\mathrm{LMTD}_{drop}} \right)} \qquad \text{Equation 6-5}$$

With this new steam steam temperature we can now find the change in pressure by utilizing an augmented condenser by either consulting a steam table of using a pressure-temperature relationship for saturated steam, such as the Goff-Gratch relationship:

$$\Delta P = P_{sat}\left(T_{s,film}\right) - P_{sat}\left(T_{s,drop}\right) \qquad \text{Equation 6-6}$$

Finally, using empirical studies relating changes in turbine efficiency to changes in condenser pressure,[3,4] we arrive at the change in the overall steam cycle efficiency:

$$\Delta\eta = (1:1.5)\Delta P \qquad \text{Equation 6-7}$$

where efficiency is given in units of percent, and pressure is given in units of kPa. The range of 1-1.5% / kPa represents the uncertainty of the empirical studies. The results of this calculation are presented below in Figure 6-2, which shows that there are diminishing returns as a result of the three individual heat transfer coefficients of the condenser occurring in series. Also shown in this figure are the measured heat transfer coefficients of a number of the surfaces evaluated in this thesis: thin polymer films deposited via initiated chemical vapor deposition (iCVD), lubricant-imbibed nanotexture (LIS), rare-earth oxide (REO), and a superhydrophobic surface that exhibits jumping condensation (jumping).

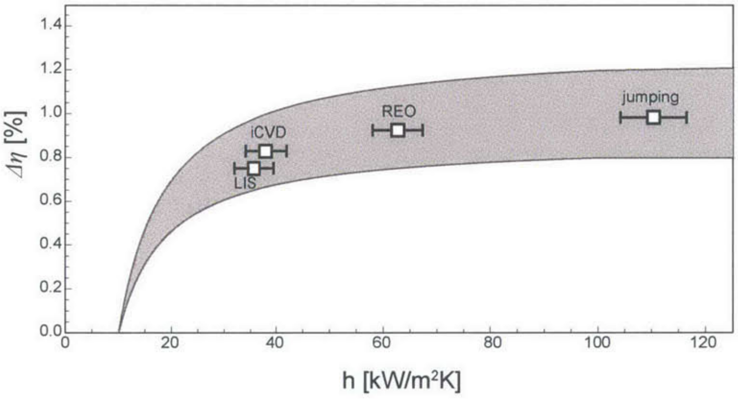

Figure 6-2. **Change in steam cycle efficiency as a function of condensation heat transfer coefficient**. Points are plotted to represent the measured values of condensation heat transfer coefficient for the surfaces evaluated in this thesis.

For the application of steam-based power plants, it is clear that even small increases in the condensation heat transfer coefficient can have a profound effect on increasing the overall steam cycle efficiency. However, owing to the diminishing returns of a higher heat transfer coefficient, is it also clear that most of the benefit of implementing dropwise condensation is captured by hydrophobic functionalizations. There may be other applications in which the extreme values of heat transfer coefficients of superhydrophobic surfaces may be desirable, but there are additional concerns with such surfaces including fragility of nanotextures and fabrication cost.

This thesis has shown that focusing on the development of robust hydrophobic functionalizations shows promise as a route that captures most of the benefits of dropwise condensation while benefiting from simpler implementation than textured superhydrophobic or lubricant-imbibed surfaces.

7 Bibliography

1. OECD. *OECD Factbook 2013.* (Organisation for Economic Co-operation and Development, 2013).
2. *World Energy Outlook 2010.* (International Energy Agency OECD Publications, 2010).
3. Lakovic, M. S., Stojiljkovic, M., Lakovic, S., Stefanovic, V. & Mitrovic, D. Impact of the cold end operating conditions on energy efficiency of the steam power plants. *Thermal Science* **14,** 53–66 (2010).
4. Vosough, A. *et al.* Improvement Power Plant Efficiency with Condenser Pressure. *International Journal of Multidisciplinary Sciences and Engineering* **2,** (2011).
5. Schmidt, E., Schurig, W. & Sellschopp, W. Versuche über die Kondensation von Wasserdampf in Film- und Tropfenform. *Technische Mechanik und Thermodynamik* **1,** 53–63 (1930).
6. Rose, J. W. Dropwise condensation theory and experiment: A review. *Proc. Inst. Mech. Eng.* **216,** 115 –128 (2002).
7. Bonner, R. W. Dropwise Condensation Life Testing of Self Assembled Monolayers. in *Proceedings of the International Heat Transfer Conference* (2010).
8. Erb, R. A. & Erb, R. A. Use of Silver Surfaces to Promote Dropwise Condensation. (1966).
9. Holden, K. M., Wanniarachchi, A. S., Marto, P. J., Boone, D. H. & Rose, J. W. The Use of Organic Coatings to Promote Dropwise Condensation of Steam. *Journal of Heat Transfer (Transactions of the ASME (American Society of*

Mechanical Engineers), Series C); (United States) **109:3,** (1987).

10. Yoshida, N. *et al.* Sliding Behavior of Water Droplets on Flat Polymer Surface. *J. Am. Chem. Soc.* **128,** 743–747 (2005).

11. Lara, J. R. & Holtzapple, M. T. Experimental investigation of dropwise condensation on hydrophobic heat exchangers part I: Dimpled-sheets. *Desalination* **278,** 165–172 (2011).

12. Marto, P. J., Looney, D. J., Rose, J. W. & Wanniarachchi, A. S. Evaluation of organic coatings for the promotion of dropwise condensation of steam. *International Journal of Heat and Mass Transfer* **29,** 1109–1117 (1986).

13. Mani, G. *et al.* Stability of Self-Assembled Monolayers on Titanium and Gold. *Langmuir* **24,** 6774–6784 (2008).

14. Dorrer, C. & Rühe, J. Condensation and wetting transitions on microstructured ultrahydrophobic surfaces. *Langmuir* **23,** 3820–3824 (2007).

15. Varanasi, K. K., Hsu, M., Bhate, N., Yang, W. & Deng, T. Spatial control in the heterogeneous nucleation of water. *Appl. Phys. Lett.* **95,** 094101 (2009).

16. He, M. *et al.* Hierarchical Porous Surface for Efficiently Controlling Microdroplets' Self-Removal. *Advanced Materials* (2013).

17. Chen, X. *et al.* Nanograssed Micropyramidal Architectures for Continuous Dropwise Condensation. *Advanced Functional Materials* **21,** 4617–4623 (2011).

18. Boreyko, J. & Chen, C. Self-Propelled Dropwise Condensate on Superhydrophobic Surfaces. *Phys. Rev. Lett.* **103,** 184501 (2009).

19. Boreyko, J. B., Zhao, Y. & Chen, C.-H. Planar jumping-drop thermal diodes. *Applied Physics Letters* **99,** 234105–234105–3 (2011).

20. Miljkovic, N. *et al.* Jumping-Droplet-Enhanced Condensation on Scalable Superhydrophobic Nanostructured Surfaces. *Nano Lett.* **13,** 179–187 (2012).

21. Kandlikar, S. G., Garimella, S., Li, D., Colin, S. & King, M. R. *Heat Transfer and Fluid flow in Minichannels and Microchannels.* (Elsevier, 2006).

22. Lu, Z. Film condensation of the component part of natural gas and heat transfer enhanced by surface longitudinal groove. (1996).

23. Rose, J. W. Surface Tension Effects and Enhancement of Condensation Heat Transfer. *Chemical Engineering Research and Design* **82,** 419–429 (2004).

24. Ghiaasiaan, S. M. *Two-Phase Flow, Boiling, and Condensation: In Conventional and Miniature Systems.* (Cambridge University Press, 2008).

25. Carey, V. P. *Liquid-Vapor Phase-Change Phenomena.* (Hemisphere Publishing, 2008).

26. Webb, R. L. & Kim, N.-H. *Principles of Enhanced Heat Transfer.* (Taylor & Francis, 2005).

27. Topper, L. & Baer, E. Dropwise condensation of vapors and heat transfer rates. *Journal of Colloid Science* **10,** 225–226 (1955).

28. Mizushina, T., Kamimura, H. & Kuriwaki, Y. Tetrafluoroethylene coatings on condenser tubes. *International Journal of Heat and Mass Transfer* **10,** 1015–1016 (1967).

29. Wilmhurst, R. Heat transfer during dropwise condensation of steam, ethane 1, 2 diol, aniline and nitrobenzene. (1979).

30. Y.-X. Wang, J. L. Plawsky, P. C. W. J. Optical Measurement of Microscale Transport Processes in Dropwise Condensation. *Microscale Thermophysical Engineering* **5,** 55–69 (2001).

31. Gokhale, S. J., Plawsky, J. L. & Wayner Jr., P. C. Effect of interfacial phenomena on dewetting in dropwise condensation. *Advances in Colloid and Interface Science* **104,** 175–190 (2003).

32. Mirkovich, V. V. & Missen, R. W. Non-filmwise condensation of binary

vapors of miscible liquids. *The Canadian Journal of Chemical Engineering* **39,** 86–87 (1961).

33. Mirkovich, V. V. & Missen, R. W. A study of the condensation of binary vapors of miscible liquids: Part 2: Heat transfer co-efficients for filmwise and non-filmwise condensation. *The Canadian Journal of Chemical Engineering* **41,** 73–78 (1963).

34. Utaka, Y. & Wang, S. Characteristic curves and the promotion effect of ethanol addition on steam condensation heat transfer. *International Journal of Heat and Mass Transfer* **47,** 4507–4516 (2004).

35. Murase, T., Wang, H. S. & Rose, J. W. Marangoni condensation of steam–ethanol mixtures on a horizontal tube. *International Journal of Heat and Mass Transfer* **50,** 3774–3779 (2007).

36. Maråk, K. A. Condensation Heat Transfer and Pressure Drop for Methane and Binary Methane Fluids in Small Channels. (2009).

37. Li, Y., Wang, G., Yan, J. & Wang, J. A Semi-Empirical Model for Condensation Heat Transfer Coefficient of Mixed Ethanol-Water Vapors. *J. Heat Transfer* **133,** 061501–061501 (2011).

38. Ali, H., Wang, H. S., Briggs, A. & Rose, J. W. Effects of Vapor Velocity and Pressure on Marangoni Condensation of Steam-Ethanol Mixtures on a Horizontal Tube. *Journal of Heat Transfer* **135,** 031502–031502 (2013).

39. Tanasawa, I. *Advances in Heat Transfer.* (Academic Press, 1991).

40. Davies, G. A., Mojtehedi, W. & Ponter, A. B. Measurement of contact angles under condensation conditions. The prediction of dropwise-filmwise transition. *International Journal of Heat and Mass Transfer* **14,** 709–713 (1971).

41. Miljkovic, N., Enright, R. & Wang, E. N. Effect of Droplet Morphology on

Growth Dynamics and Heat Transfer during Condensation on Superhydrophobic Nanostructured Surfaces. *ACS Nano* **6,** 1776–1785 (2012).

42. Rykaczewski, K. Microdroplet Growth Mechanism during Water Condensation on Superhydrophobic Surfaces. *Langmuir* **28,** 7720–7729 (2012).

43. Lee, S. *et al.* Heat transfer measurement during dropwise condensation using micro/nano-scale porous surface. *International Journal of Heat and Mass Transfer* **65,** 619–626 (2013).

44. Kim, S. & Kim, K. J. Dropwise condensation modeling suitable for superhydrophobic surfaces. *Journal of heat transfer* **133,** (2011).

45. Zhao, H. & Beysens, D. From droplet growth to film growth on a heterogeneous surface: condensation associated with a wettability gradient. *Langmuir* **11,** 627–634 (1995).

46. Rykaczewski, K. *et al.* How nanorough is rough enough to make a surface superhydrophobic during water condensation? *Soft Matter* **8,** 8786 (2012).

47. Rykaczewski, K. *et al.* Multimode Multidrop Serial Coalescence Effects during Condensation on Hierarchical Superhydrophobic Surfaces. *Langmuir* **29,** 881–891 (2013).

48. Lafuma, A. & Quéré, D. Superhydrophobic states. *Nat. Mater.* **2,** 457–460 (2003).

49. Nosonovsky, M. & Bhushan, B. Biomimetic Superhydrophobic Surfaces: Multiscale Approach. *Nano Lett.* **7,** 2633–2637 (2007).

50. Dorrer, C. & Rühe, J. Some thoughts on superhydrophobic wetting. *Soft Matter* **5,** 51 (2009).

51. Tuteja, A., Choi, W., Mabry, J. M., McKinley, G. H. & Cohen, R. E. Robust Omniphobic Surfaces. *Proc. Natl. Acad. Sci.* **105,** 18200–18205 (2008).

52. Tuteja, A. *et al.* Designing Superoleophobic Surfaces. *Science* **318,** 1618 – 1622 (2007).

53. Deng, X., Mammen, L., Butt, H.-J. & Vollmer, D. Candle Soot as a Template for a Transparent Robust Superamphiphobic Coating. *Science* **335,** 67–70 (2012).

54. Wier, K. & McCarthy, T. Condensation on ultrahydrophobic surfaces and its effect on droplet mobility: Ultrahydrophobic surfaces are not always water repellant. *Langmuir* **22,** 2433–2436 (2006).

55. Narhe, R. D. & Beysens, D. A. Water condensation on a superhydrophobic spike surface. *Europhys. Lett.* **75,** 98–104 (2006).

56. Jung, Y. C. & Bhushan, B. Wetting behaviour during evaporation and condensation of water microdroplets on superhydrophobic patterned surfaces. *Journal of Microscopy* **229,** 127–140 (2008).

57. Varanasi, K. K., Deng, T., Smith, J. D., Hsu, M. & Bhate, N. Frost formation and ice adhesion on superhydrophobic surfaces. *Appl. Phys. Lett.* **97,** 234102 (2010).

58. Anand, S., Paxson, A. T., Dhiman, R., Smith, J. D. & Varanasi, K. K. Enhanced Condensation on Lubricant-Impregnated Nanotextured Surfaces. *ACS Nano* **6,** 10122–10129 (2012).

59. Verheijen, H. J. J. & Prins, M. W. J. Reversible Electrowetting and Trapping of Charge: Model and Experiments. *Langmuir* **15,** 6616–6620 (1999).

60. Quéré, D. Non-sticking drops. *Rep. Prog. Phys.* **68,** 2495–2532 (2005).

61. Wong, T.-S. *et al.* Bioinspired self-repairing slippery surfaces with pressure-stable omniphobicity. *Nature* **477,** 443–447 (2011).

62. Lafuma, A. & Quéré, D. Slippery pre-suffused surfaces. *EPL* **96,** 56001

(2011).

63. Smith, J. D. *et al.* Droplet mobility on lubricant-impregnated surfaces. *Soft Matter* **9,** 1772 (2013).

64. Paxson, A. T. Nanoengineered surfaces for energy efficiency. (2012).

65. Azimi, G., Dhiman, R., Kwon, H.-M., Paxson, A. T. & Varanasi, K. K. Hydrophobicity of rare-earth oxide ceramics. *Nat Mater* **12,** 315–320 (2013).

66. Paxson, A. T., Yagüe, J. L., Gleason, K. K. & Varanasi, K. K. Stable Dropwise Condensation for Enhancing Heat Transfer via the Initiated Chemical Vapor Deposition (iCVD) of Grafted Polymer Films. *Advanced Materials* **26,** 418–423 (2014).

67. Paxson, A. T. & Varanasi, K. K. Self-similarity of contact line depinning from textured surfaces. *Nature Communications* **4,** 1492 (2013).

68. *Standards for steam surface condensers / Heat Exchange Institute.* (Cleveland, Ohio : The Institute, 2012).

69. Al-Shammari, S. B. Condensation of steam with and without the presence of non-condensable gases in a vertical tube. *Desalination* **169,** 151–160 (2004).

70. Kroger, D. G. & Rohsenow, W. M. Condensation heat transfer in the presence of a non-condensable gas. *International Journal of Heat and Mass Transfer* **11,** 15–26 (1968).

71. Ma, X.-H., Zhou, X.-D., Lan, Z., LI, Y.-M. & Zhang, Y. Condensation heat transfer enhancement in the presence of non-condensable gas using the interfacial effect of dropwise condensation. *International Journal of Heat and Mass Transfer* **51,** 1728–1737 (2008).

72. Tanner, D. W., Pope, D., Potter, C. J. & West, D. Heat transfer in dropwise condensation at low steam pressures in the absence and presence of

non-condensable gas. *International Journal of Heat and Mass Transfer* **11,** 181–182 (1968).

73. Depew, C. A. & Reisbig, R. L. Vapor Condensation on a Horizontal Tube Using Teflon to Promote Dropwise Condensation. *Ind. Eng. Chem. Proc. Des. Dev.* **3,** 365–369 (1964).

74. Smith, S., Francis, R. & Barnes, C. Treatment of condenser tubes. (1990).

75. Bani Kananeh, A., Rausch, M. H., Fröba, A. P. & Leipertz, A. Experimental study of dropwise condensation on plasma-ion implanted stainless steel tubes. *International Journal of Heat and Mass Transfer* **49,** 5018–5026 (2006).

76. Furman, T. & Hampson, H. Experimental Investigation into the Effects of Cross Flow with Condensation of Steam and Steam-Gas Mixtures on a Vertical Tube. *Proceedings of the Institution of Mechanical Engineers* **173,** 147–169 (1959).

77. Singh, S. Heat transfer during condensation of steam over a vertical grid of horizontal integral-fin copper tubes. *Applied Thermal Engineering* **21,** 717–730 (2001).

78. Koch, G., Zhang, D. C. & Leipertz, A. Condensation of steam on the surface of hard coated copper discs. *Heat and Mass Transfer* **32,** 149–156 (1997).

79. Koch, G. Untersuchungen zur Tropfenkondensation auf metallischen, hartstoffbeschichteten OberflaĻchen. Dr.-Ing. (1996).

80. Alf, M. E. *et al.* Chemical Vapor Deposition of Conformal, Functional, and Responsive Polymer Films. *Advanced Materials* **22,** 1993–2027 (2010).

81. Hare, E. F., Shafrin, E. G. & Zisman, W. A. Properties of Films of

Adsorbed Fluorinated Acids. *J. Phys. Chem.* **58,** 236–239 (1954).

82. Nishino, T., Meguro, M., Nakamae, K., Matsushita, M. & Ueda, Y. The Lowest Surface Free Energy Based on –CF3 Alignment. *Langmuir* **15,** 4321–4323 (1999).

83. Coclite, A. M., Shi, Y. & Gleason, K. K. Controlling the Degree of Crystallinity and Preferred Crystallographic Orientation in Poly-Perfluorodecylacrylate Thin Films by Initiated Chemical Vapor Deposition. *Adv. Funct. Mater.* **22,** 2167–2176 (2012).

84. Coclite, A. M., Shi, Y. & Gleason, K. K. Grafted Crystalline Poly-Perfluoroacrylate Structures for Superhydrophobic and Oleophobic Functional Coatings. *Adv. Mater.* **24,** 4534–4539 (2012).

85. Raghunathan, V. *et al.* Co-polymer clad design for high performance athermal photonic circuits. *Opt. Express* **20,** 20808–20813 (2012).

86. Yagüe, J. L. & Gleason, K. K. Enhanced crosslinked density by annealing on fluorinated polymers synthesized bia initiated chemical vapor deposition to prevent surface reconstruction. *Macromolecules* **46,** 6548–6554 (2013).

87. Gupta, M. & Gleason, K. K. Surface modification of high aspect ratio structures with fluoropolymer coatings using chemical vapor deposition. *Thin Solid Films* **517,** 3547–3550 (2009).

88. Beysens, D. & Knobler, C. Growth of breath figures. *Physical review letters* **57,** 1433–1436 (1986).

89. Arkles, B. *Hydrophobicity, Hydrophilicity, and Silane Surface Modification.* (Gelest, Inc., 2010).

90. Kung, H. H. *Transition Metal Oxides: Surface Chemistry and Catalysis.* (Elsevier, 1989).

91. Stirnemann, G., Rossky, P. J., Hynes, J. T. & Laage, D. Water reorientation, hydrogen-bond dynamics and 2D-IR spectroscopy next to an extended hydrophobic surface - Faraday Discussions (RSC Publishing). *Faraday Discuss.* **146,** 263–281 (2010).

92. Topp, N. E. *The chemistry of the rare-earth elements.* (Elsevier Amsterdam, 1965).

93. Good, R. J. Contact angle, wetting, and adhesion: a critical review. *Journal of adhesion science and technology* **6,** 1269–1302 (1992).

94. Prakash, M., Quéré, D. & Bush, J. W. M. Surface Tension Transport of Prey by Feeding Shorebirds: The Capillary Ratchet. *Science* **320,** 931–934 (2008).

95. Zheng, Y., Gao, X. & Jiang, L. Directional adhesion of superhydrophobic butterfly wings. *Soft Matter* **3,** 178–182 (2007).

96. Zheng, Y. *et al.* Directional water collection on wetted spider silk. *Nature* **463,** 640–643 (2010).

97. Dussan V., E. B. & Davis, S. H. On the motion of a fluid-fluid interface along a solid surface. *J. Fluid Mech.* **65,** 71–95 (1974).

98. Chen *et al.* Nanowires for Enhanced Boiling Heat Transfer. *Nano Letters* **9,** 548–553 (2009).

99. Patankar, N. A. Supernucleating surfaces for nucleate boiling and dropwise condensation heat transfer. *Soft Matter* **6,** 1613 (2010).

100. Koc, Y. *et al.* Nano-scale superhydrophobicity: suppression of protein adsorption and promotion of flow-induced detachment. *Lab Chip* **8,** 582–586 (2008).

101. Choi, W. *et al.* Bubbles navigating through networks of microchannels.

Lab Chip **11,** 3970–3978 (2011).

102. Joanny, J. F. & de Gennes, P. G. A model for contact angle hysteresis. *J. Chem. Phys.* **81,** 552–562 (1984).

103. Pompe, T. & Herminghaus, S. Three-Phase Contact Line Energetics from Nanoscale Liquid Surface Topographies. *Phys. Rev. Lett.* **85,** 1930–1933 (2000).

104. Vedantam, S. & Panchagnula, M. V. Phase Field Modeling of Hysteresis in Sessile Drops. *Phys. Rev. Lett.* **99,** 176102 (2007).

105. Decker, E. L., Frank, B., Suo, Y. & Garoff, S. Physics of contact angle measurement. *Colloids Surf., A* **156,** 177–189 (1999).

106. Pagonabarraga, I. Wetting dynamics: Adsorbed colloids relax slowly. *Nat. Mater.* **11,** 99–100 (2012).

107. Kaz, D. M., McGorty, R., Mani, M., Brenner, M. P. & Manoharan, V. N. Physical ageing of the contact line on colloidal particles at liquid interfaces. *Nat. Mater.* **11,** 138–142 (2011).

108. Giovambattista, N., Debenedetti, P. G. & Rossky, P. J. Enhanced Surface Hydrophobicity by Coupling of Surface Polarity and Topography. *Proc. Natl. Acad. Sci.* **106,** 15181–15185 (2009).

109. Koishi, T., Yasuoka, K., Fujikawa, S., Ebisuzaki, T. & Zeng, X. C. Coexistence and Transition Between Cassie and Wenzel State on Pillared Hydrophobic Surface. *Proc. Natl. Acad. Sci.* **106,** 8435–8440 (2009).

110. Bocquet, L. & Lauga, E. A smooth future? *Nat. Mater.* **10,** 334–337 (2011).

111. Shirtcliffe, N. J., McHale, G., Newton, M. I., Chabrol, G. & Perry, C. C. Dual-Scale Roughness Produces Unusually Water-Repellent Surfaces. *Adv. Mater.* **16,** 1929–1932 (2004).

112. Reyssat, M. & Quéré, D. Contact Angle Hysteresis Generated by Strong Dilute Defects†. *J. Phys. Chem. B* **113,** 3906–3909 (2009).

113. Öner, D. & McCarthy, T. J. Ultrahydrophobic Surfaces. Effects of Topography Length Scales on Wettability. *Langmuir* **16,** 7777–7782 (2000).

114. Herminghaus, S. Roughness-induced non-wetting. *Europhys. Lett.* **52,** 165–170 (2000).

115. Bico, J., Marzolin, C. & Quéré, D. Pearl drops. *Europhys. Lett.* **47,** 220–226 (1999).

116. Extrand, C. W. Model for Contact Angles and Hysteresis on Rough and Ultraphobic Surfaces. *Langmuir* **18,** 7991–7999 (2002).

117. Gao, L. & McCarthy, T. J. Contact Angle Hysteresis Explained. *Langmuir* **22,** 6234–6237 (2006).

118. Dorrer, C. & Rühe, J. Advancing and Receding Motion of Droplets on Ultrahydrophobic Post Surfaces. *Langmuir* **22,** 7652–7657 (2006).

119. Kusumaatmaja, H. & Yeomans, J. M. Modeling Contact Angle Hysteresis on Chemically Patterned and Superhydrophobic Surfaces. *Langmuir* **23,** 6019–6032 (2007).

120. Patankar, N. A. Hysteresis with Regard to Cassie and Wenzel States on Superhydrophobic Surfaces. *Langmuir* **26,** 7498–7503 (2010).

121. Krumpfer, J. W. & McCarthy, T. J. Contact angle hysteresis: a different view and a trivial recipe for low hysteresis hydrophobic surfaces. *Faraday Discuss.* **146,** 103 (2010).

122. Lv, C., Yang, C., Hao, P., He, F. & Zheng, Q. Sliding of Water Droplets on Microstructured Hydrophobic Surfaces. *Langmuir* **26,** 8704–8708 (2010).

123. Mognetti, B. M. & Yeomans, J. M. Modeling Receding Contact Lines on

Superhydrophobic Surfaces. *Langmuir* **26,** 18162–18168 (2010).

124. Gibbs, J. W. *The Scientific Papers, Vol I: Thermodynamics.* (Dover Publications, 1961).

125. Chibbaro, S. *et al.* Capillary Filling in Microchannels with Wall Corrugations: A Comparative Study of the Concus–Finn Criterion by Continuum, Kinetic, and Atomistic Approaches. *Langmuir* **25,** 12653–12660 (2009).

126. Mirsaidov, U. M., Zheng, H., Bhattacharya, D., Casana, Y. & Matsudaira, P. Direct observation of stick-slip movements of water nanodroplets induced by an electron beam. *Proc. Natl. Acad. Sci.* **109,** 7187–7190 (2012).

127. Choi, W., Tuteja, A., Mabry, J. M., Cohen, R. E. & McKinley, G. H. A modified Cassie-Baxter relationship to explain contact angle hysteresis and anisotropy on non-wetting textured surfaces. *J. Colloid Interface Sci.* **339,** 208–216 (2009).

128. Luo, C. *et al.* Direct Three-Dimensional Imaging of the Buried Interfaces between Water and Superhydrophobic Surfaces. *Angew. Chem. Int. Ed.* **49,** 9145–9148 (2010).

129. Krumpfer, J. W., Bian, P., Zheng, P., Gao, L. & McCarthy, T. J. Contact Angle Hysteresis on Superhydrophobic Surfaces: An Ionic Liquid Probe Fluid Offers Mechanistic Insight. *Langmuir* **27,** 2166–2169 (2011).

130. Dufour, R. *et al.* Zipping Effect on Omniphobic Surfaces for Controlled Deposition of Minute Amounts of Fluid or Colloids. *Small* 1–8 (2011).

131. Dufour, R., Harnois, M., Thomy, V., Boukherroub, R. & Senez, V. Contact angle hysteresis origins: Investigation on super-omniphobic surfaces. *Soft Matter* **7,** 9380–9387 (2011).

132. Papadopoulos, P. *et al.* Wetting on the Microscale: Shape of a Liquid

Drop on a Microstructured Surface at Different Length Scales. *Langmuir* **28,** 8392–8398 (2012).

133. Chatain, D., Lesueur, C. & Baland, J.-P. Wetting of Pb on Oxidized Micropatterned Si Wafers. *Langmuir* **22,** 4230–4236 (2006).

134. Priest, C., Albrecht, T. W. J., Sedev, R. & Ralston, J. Asymmetric Wetting Hysteresis on Hydrophobic Microstructured Surfaces. *Langmuir* **25,** 5655–5660 (2009).

135. Reyssat, M., Yeomans, J. M. & Quéré, D. Impalement of fakir drops. *Europhys. Lett.* **81,** 26006 (2008).

136. Rathgen, H. & Mugele, F. Microscopic shape and contact angle measurement at a superhydrophobic surface. *Faraday Discuss.* **146,** 49 (2010).

137. Huh, C. & Scriven, L. E. Shapes of axisymmetric fluid interfaces of unbounded extent. *J. Colloid Interface Sci.* **30,** 323–337 (1969).

138. Padday, J. F., Pitt, A. R. & Pashley, R. M. Menisci at a free liquid surface: surface tension from the maximum pull on a rod. *J. Chem. Soc., Faraday Trans. 1:* **71,** 1919 (1975).

139. Mognetti, B. M. & Yeomans, J. M. Capillary filling in microchannels patterned by posts. *Phys. Rev. E* **80,** 056309 (2009).

140. Vagharchakian, L., Restagno, F. & Léger, L. Capillary Bridge Formation and Breakage: A Test to Characterize Antiadhesive Surfaces†. *J. Phys. Chem. B* **113,** 3769–3775 (2008).

141. Restagno, F., Poulard, C., Cohen, C., Vagharchakian, L. & Léger, L. Contact Angle and Contact Angle Hysteresis Measurements Using the Capillary Bridge Technique. *Langmuir* **25,** 11188–11196 (2009).

142. Dorrer, C. & Rühe, J. Wetting of Silicon Nanograss: From

Superhydrophilic to Superhydrophobic Surfaces. *Adv. Mater.* **20,** 159–163 (2008).

143. Neinhuis, C. & Barthlott, W. Characterization and distribution of water-repellent, self-cleaning plant surfaces. *Ann. Bot.* **79,** 667 (1997).

144. Cheng, Z., Gao, J. & Jiang, L. Tip Geometry Controls Adhesive States of Superhydrophobic Surfaces. *Langmuir* **26,** 8233–8238 (2010).

145. Prakash, M. & Bush, J. W. M. Interfacial propulsion by directional adhesion. *Int. J. Non Linear Mech.* **46,** 607–615 (2011).

146. Duprat, C., Protière, S., Beebe, A. Y. & Stone, H. A. Wetting of flexible fibre arrays. *Nature* **482,** 510–513 (2012).

147. Dietz, C., Rykaczewski, K., Fedorov, A. G. & Joshi, Y. Visualization of droplet departure on a superhydrophobic surface and implications to heat transfer enhancement during dropwise condensation. *Appl. Phys. Lett.* **97,** 033104 (2010).

148. He, M. *et al.* Hierarchically structured porous aluminum surfaces for high-efficient removal of condensed water. *Soft Matter* (2012).

149. Feng, J., Qin, Z. & Yao, S. Factors Affecting the Spontaneous Motion of Condensate Drops on Superhydrophobic Copper Surfaces. *Langmuir* **28,** 6067–6075 (2012).

150. Enright, R., Miljkovic, N., Al-Obeidi, A., Thompson, C. V. & Wang, E. N. Condensation on Superhydrophobic Surfaces: The Role of Local Energy Barriers and Structure Length Scale. *Langmuir* **28,** 14424–14432 (2012).

151. Liu, T., Sun, W., Sun, X. & Ai, H. Thermodynamic Analysis of the Effect of the Hierarchical Architecture of a Superhydrophobic Surface on a Condensed Drop State. *Langmuir* **26,** 14835–14841 (2010).

152. Liu, T. Q., Sun, W., Sun, X. Y. & Ai, H. R. Mechanism study of condensed drops jumping on super-hydrophobic surfaces. *Colloids and Surfaces A: Physicochemical and Engineering Aspects* **414,** 366–374 (2012).

153. Choi, C.-H. & Kim, C.-J. Fabrication of a dense array of tall nanostructures over a large sample area with sidewall profile and tip sharpness control. *Nanotechnology* **17,** 5326 (2006).

154. Wang, F.-C., Yang, F. & Zhao, Y.-P. Size effect on the coalescence-induced self-propelled droplet. *Applied Physics Letters* **98,** 053112 –053112–3 (2011).

155. Verho, T. *et al.* Reversible switching between superhydrophobic states on a hierarchically structured surface. *PNAS* **109,** 10210–10213 (2012).

156. Narhe, R. & Beysens, D. Growth dynamics of water drops on a square-pattern rough hydrophobic surface. *Langmuir* **23,** 6486–6489 (2007).

157. Quéré, D. Wetting and Roughness. *Annu. Rev. Mater. Res.* **38,** 71–99 (2008).

158. Cheng, Y. & Rodak, D. Is the lotus leaf superhydrophobic? *Appl. Phys. Lett.* **86,** 144101 (2005).

159. Dorrer, C. & Rühe, J. Condensation and Wetting Transitions on Microstructured Ultrahydrophobic Surfaces. *Langmuir* **23,** 3820–3824 (2007).

160. Jung, Y. C. & Bhushan, B. Wetting Behavior of Water and Oil Droplets in Three-Phase Interfaces for Hydrophobicity/philicity and Oleophobicity/philicity†. *Langmuir* **25,** 14165–14173 (2009).

161. Miljkovic, N. *et al.* Jumping-Droplet-Enhanced Condensation on Scalable Superhydrophobic Nanostructured Surfaces. *Nano Lett.* **13,** 179–187 (2013).

162. Rykaczewski, K. *et al.* Dropwise Condensation of Low Surface Tension

Fluids on Omniphobic Surfaces. *Sci. Rep.* **4,** (2014).

163. Seiwert, J., Clanet, C. & Quéré, D. Coating of a Textured Solid. *Journal of Fluid Mechanics* **669,** 55–63 (2011).

164. Stauffer, C. E. The measurement of surface tension by the pendant drop technique. *The journal of physical chemistry* **69,** 1933–1938 (1965).

165. Pfruender, H., Jones, R. & Weuster-Botz, D. Water immiscible ionic liquids as solvents for whole cell biocatalysis. *Journal of Biotechnology* **124,** 182–190 (2006).

166. Shvedene, N. V., Borovskaya, S. V., Sviridov, V. V., Ismailova, E. R. & Pletnev, I. V. Measuring the solubilities of ionic liquids in water using ion-selective electrodes. *Anal Bioanal Chem* **381,** 427–430 (2005).

167. Freire, M. G. *et al.* Surface tensions of imidazolium based ionic liquids: Anion, cation, temperature and water effect. *Journal of Colloid and Interface Science* **314,** 621–630 (2007).

168. Jacquemin, J., Husson, P., Padua, A. A. H. & Majer, V. Density and viscosity of several pure and water-saturated ionic liquids - Green Chemistry (RSC Publishing). *Green Chemistry* (2011).

169. Harkins, W. D. & Feldman, A. Films. The spreading of liquids and the spreading coefficient. *J. Am. Chem. Soc.* **44,** 2665–2685 (1922).

170. Eslami, F. & Elliott, J. A. W. Thermodynamic Investigation of the Barrier for Heterogeneous Nucleation on a Fluid Surface in Comparison with a Rigid Surface. *J. Phys. Chem. B* **115,** 10646–10653 (2011).

171. Rose, J. W. & Glicksman, L. R. Dropwise condensation–The distribution of drop sizes. *International Journal of Heat and Mass Transfer* **16,** 411–425 (1973).

172. Chinn, J. *et al.* Durable Super-Hydrophobic Nano-Composite Films. *NSTI-Nanotech 2010* **1,** (2010).

173. Srinivasan, S., Chhatre, S. S., Mabry, J. M., Cohen, R. E. & McKinley, G. H. Solution spraying of poly(methyl methacrylate) blends to fabricate microtextured, superoleophobic surfaces. *Polymer* **52,** 3209–3218 (2011).

174. Wenzel, R. Resistance of solid surfaces to wetting by water. *Industrial and Engineering Chemistry* **28,** (1936).

175. Nusselt, W. Die Oberflachenkondesation des Wasserdamffes the surface condensation of water. *Zetrschr. Ver. Deutch. Ing.* **60,** 541–546 (1916).